8-19-2013 12:00 AM

Accelerated Imaging Techniques for Chemical Shift Magnetic Resonance Imaging

Curtis N. Wiens
The University of Western Ontario

Supervisor
Charles McKenzie
The University of Western Ontario

Graduate Program in Physics
A thesis submitted in partial fulfillment of the requirements for the degree in Doctor of Philosophy

Recommended Citation

Wiens, Curtis N., "Accelerated Imaging Techniques for Chemical Shift Magnetic Resonance Imaging" (2013). *Electronic Thesis and Dissertation Repository*. 1465.
https://ir.lib.uwo.ca/etd/1465

Accelerated Imaging Techniques for Chemical Shift Magnetic Resonance Imaging
(Thesis format: Integrated Article)

by

Curtis N. Wiens

Graduate Program in Physics

A thesis submitted in partial fulfillment
of the requirements for the degree of
Doctor of Philosophy

The School of Graduate and Postdoctoral Studies
The University of Western Ontario
London, Ontario, Canada

Abstract

Chemical shift imaging is a magnetic resonance imaging technique that separates the signal from two or more chemical species. The cost of chemical shift encoding is increased acquisition time as multiple acquisitions are required at different echo times. Image acceleration techniques, typically parallel imaging, are often used to improve coverage and resolution. This thesis describes a new technique for estimating the signal to noise ratio for parallel imaging reconstructions and proposes new image reconstructions for accelerated chemical shift imaging using compressed sensing and/or parallel imaging for two applications: water-fat separation and metabolic imaging of hyperpolarized [1-^{13}C] pyruvate.

Spatially varying noise in parallel imaging reconstructions makes measurements of the signal to noise ratio, a commonly used metric for image for image quality, difficult. Existing approaches have limitations: they are not applicable to all reconstructions, require significant computation time, or rely on repeated image acquisitions. A signal to noise ratio estimation technique is proposed that does not exhibit these limitations.

Water-fat imaging of highly undersampled datasets from the liver, calf, knee, and abdominal cavity are demonstrated using a customized IDEAL-SPGR pulse sequence and an integrated compressed sensing, parallel imaging, water-fat reconstruction. This method offers image quality comparable to fully sampled reference images for a range of acceleration factors. At high acceleration factors, this method offers improved image quality when compared to the current standard of parallel imaging.

Accelerated metabolic imaging of hyperpolarized [1-^{13}C] pyruvate and its metabolic by-products lactate, alanine, and bicarbonate is demonstrated using an integrated compressed sensing, metabolite separation reconstruction. Phantoms are used to validate this technique while retrospectively and prospectively accelerated 3D *in vivo* datasets are used to demonstrate feasibility. An alternative approach to accelerated metabolic imaging is demonstrated using high performance magnetic field gradient set.

This thesis addresses the inherently slow acquisition times of chemical shift imaging by examining the role compressed sensing and parallel imaging can play in chemical shift imaging. An approach to SNR assessment for parallel imaging reconstruction is proposed and approaches to accelerated chemical shift imaging are described for applications in water-fat imaging and metabolic imaging of hyperpolarized [1-^{13}C] pyruvate.

Keywords

Water-fat imaging, chemical shift imaging, hyperpolarized carbon-13, parallel imaging, compressed sensing, signal to noise ratio

Co-Authorship Statement

The work in chapter 2 entitled "Computationally Rapid Method of Estimating Signal-To-Noise Ratio for Phased Array Image Reconstructions" is published in the journal Magnetic Resonance in Medicine and is co-authored by Curtis Wiens, Shawn Kisch, Jacob Willig-Onwuachi, and Charles McKenzie. Curtis Wiens was responsible for the implementation of the proposed technique, experimental validations, acquisition and analysis of phantom data, and the writing of the manuscript. Shawn Kisch wrote the Pseudo-replica SNR code used, a method of SNR measurements that the proposed method was compared to. Jacob Willig-Onwuachi and Charles McKenzie provided advice regarding experimental validations and assisted in the preparations of the manuscript. *In vivo* datasets were acquired by Cyndi Harper Little.

The work in chapter 3 entitled "R_2^*-corrected Water-Fat Imaging using Compressed Sensing and Parallel Imaging" is published in the journal Magnetic Resonance in Medicine and is co-authored by Curtis Wiens, Colin McCurdy, Jacob Willig-Onwuachi and Charles McKenzie. Curtis Wiens was responsible for the implementation of the proposed image reconstruction, the implementation of the MRI pulse sequence used to validate the proposed image reconstruction, and the writing of the manuscript. Colin McCurdy assisted in the development of the pulse sequence. Jacob Willig-Onwuachi and Charles McKenzie provided advice regarding experimental validations of the image reconstruction and pulse sequence. In addition, they assisted in the preparations of the manuscript. *In vivo* data were acquired by Trevor Szekeres.

The work in chapter 4 entitled "Accelerated ^{13}C Chemical Shift Imaging of Hyperpolarized Pyruvate" is in preparation for submittion to the journal Magnetic Resonance in Medicine and is co-authored by Curtis Wiens, Lanette Friesen-Waldner, Trevor Wade, Kevin Sinclair, and Charles McKenzie. Curtis Wiens was responsible for the implementation of the proposed image reconstruction, the implementation of the MRI pulse sequence, data acquisition, and the writing of the manuscript. Lanette Friesen-Waldner was responsible for the polarization and injection of the hyperpolarized constrast agents and the preparations of animals. Trevor Wade provided training regarding the acquisition of hyperpolarized ^{13}C data and advice on pulse sequence design. Kevin Sinclair assisted with the data acquisition. Charles McKenzie provided advice regarding experimental validation and assisted with preparations of the manuscript.

Acknowledgments

The completion of a PhD is not done without support of many people. Here are a few people that I'd like to acknowledge at this milestone of my life.

I'd like to begin by thanking my supervisor Dr. Charles McKenzie. Charlie, I appreciated the effort you made to be available, approachable, and understanding. I remember the numerous times I came into his office saying "I set the wrong the CVs" or "I set the wrong center frequency". There is often something to be learned from your mistakes but no point dwelling on it. It wasn't always clear what direction this project would go but I learned a lot along the way.

Secondly, I'd like to thank Jacob Willig-Onwuachi. Jake, you were like a 2nd supervisor to me. Your attention to detail makes you great to work with. Throughout this PhD, I always got you involved in my work. It was clear very early on, that your involvement always resulted in better manuscripts and a better understanding of my work.

The task of familiarizing oneself with GE's pulse sequence programming language EPIC is daunting. Trevor Wade, Ann Shimakawa, and Alexei Ouriadov played instrumental roles in the completion process. Trevor, thank you for teaching me the fundamentals of pulse sequence programming and always making time to answer my questions. Your first email regarding EPIC programming entitled "You want to program in EPIC? Run while you still can" has been viewed many times throughout the course of this PhD. Ann, thank you for your assistance with the IDEAL-IQ pulse sequence. Whenever I got stuck implementing one of my crazy ideas, Charlie's advice was always the same: "Just ask Ann". Alexei, thank you for your assistance regarding the broadbanding of pulse sequences.

Throughout my time here, the personnel in the McKenzie Lab have changed a lot. I'd like to thank each member of the lab, past and present. Each of you contributed into making the McKenzie Lab an enjoyable place to work. I thank you all for your friendships, collaborations, encouragement, and memories over the last five years.

Lastly, I'd to thank my family for their love and support. It's safe to say I wouldn't be here celebrating this accomplishment if not for you.

Table of Contents

List of Tables

List of Figures

Glossary

3D	Three dimensional
2D	Two dimensional
AF	Acceleration Factor
BW	Acquisition bandwidth
CS	Compressed Sensing
DESPOT	Driven equilibrium single pulse observation of T_1/T_2
ΔTE	Echo spacing
ETL	Echo train length
FOV	Field of view
γ	Gyromagnetic ratio
GRAPPA	Generalized autocalibrating partially parallel acquisitions
Hz	Hertz
IDEAL	Iterative Decomposition of water and fat with Echo Asymmetric and Least-squares estimation
MRI	Magnetic resonance imaging
ORF	Outer Reduction Factor
PMRI	Parallel magnetic resonance imaging
R2*	Effective transverse relaxation time
ROI	Region of interest
SENSE	Sensitivity encoding

SMASH	Simultaneous acquisition of spatial harmonics
SNR	Signal to noise ratio
SPGR	Spoiled gradient recalled echo
T	Tesla
T_1	Longitudinal relaxation time
TE	Echo time
TR	Repetition time
VOI	Volume of interest

Chapter 1

1 Introduction

Magnetic resonance imaging (MRI) is a non-invasive imaging modality based on the interaction of nuclear spins, typically from the ^{1}H of water and fat, with an external magnetic field. MRI is routinely used in clinical practice and offers several advantages over other imaging modalities including no ionizing radiation and excellent soft tissue contrast. The signal (and phase of signal) of magnetic resonance (MR) images is sensitive to many different physiologic and user defined parameters. This sensitivity can be exploited allowing different types of contrast to be generated.

One form of MRI is chemical shift imaging. In this technique, the different resonance frequencies of chemical species (known as a chemical shift) are exploited to separate the signal from each chemical species. This separation is achieved by encoding the MR images in additional dimension, a spectral dimension called the chemical shift dimension. This chemical shift dimension is sampled by acquiring images at different echo times. The sampling of this additional dimension is time-consuming and can limit the resolution and spatial coverage achievable.

The predominant use of chemical shift imaging is water-fat imaging. In this technique, the signal from water is separated from the signal from fat resulting two images: a water-only image and a fat-only image. Clinically, water-fat imaging is used in imaging of organs such as the liver, heart, and spine for applications such quantitative grading and staging of non-alcoholic fatty liver disease (1), quantification of fat in bone marrow (2,3), measurement of total visceral adipose tissue (4), detection of brown fat (5,6), and detection of myocardial fat infiltration (7).

Chemical shift imaging has also been proposed as a method to detect metabolites for hyperpolarized ^{13}C imaging of [1-^{13}C] pyruvate. Here, the signal from pyruvate and its metabolic by-products lactate, alanine, and bicarbonate are separated. Detection of pyruvate's metabolites through hyperpolarized ^{13}C imaging offers the unique opportunity to probe abnormalities in metabolism. These metabolic abnormalities often precede the structural abnormalities seen in a traditional MRI. Metabolic imaging through hyperpolarized ^{13}C imaging has many potential applications, including the detection and staging of diseases like cancer and the metabolic syndrome.

This thesis examines the applications of two acceleration techniques, compressed sensing and parallel imaging, to chemical shift imaging. First, a new method for measuring the signal-to-noise ratio (SNR) for parallel imaging reconstructions is described. Then, new methods to reconstruct water-fat images and pyruvate and its metabolic by-products are proposed. These methods separate chemical species using fewer measurements than conventional approaches thereby accelerating image acquisition times.

In this chapter, I introduce MR spatial encoding, existing image acceleration techniques, water-fat imaging, and hyperpolarized ^{13}C imaging.

1.1 Spatial Encoding

Three types of magnetic fields are used in MRI to produce an image: the main magnetic field, radiofrequency pulses, and gradients. The main magnetic field polarizes the magnetic moments of ^{1}H leading to a net magnetization aligned along the direction of the magnetic field, the radiofrequency-pulse tilts this net magnetization into the transverse plane allowing a nearby coil to detect a signal, and the gradients allow us to resolve spatially where the measured signal is coming from. In this section, the process of spatial localization by means of gradients is described.

In the presence of a main magnetic field and absence of gradients, all ^{1}H will precess about the main magnetic field (B_0) at the Larmor frequency (ω_0):

$$\omega_0 = \gamma B_0 \tag{1.1}$$

where γ is the gyromagnetic ratio. After demodulation of ω_0, the detected signal by a nearby coil will be proportional to the integral of the spin density $\rho(x,y)$ over the excited volume:

$$S \propto \int \rho(x,y)\, dxdy. \tag{1.2}$$

Under these conditions, the spatial location of the signal cannot be determined.

1.1.1 Frequency Encoding

The spatial location of the spin densities can be resolved in one dimension (x dimension) through a process called frequency encoding. In this process an additional linearly varying magnetic field called a gradient is superimposed onto main magnetic field. In the presence of this gradient (G_x), the precessional frequency will now vary as a function of position (x):

$$\omega(x) = \gamma(B_0 + G_x(t)x). \tag{1.3}$$

At any time t, the distribution of frequencies caused by the gradient will result in additional accrual of phase ($\Delta\phi_f$)

$$\Delta\phi_f(x,t) = -x\gamma \int_0^t G_x(t')\, dt' \tag{1.4}$$

After demodulation of ω_0, the detected signal is now the integral of the product of the spin density and this gradient induced phase term:

$$S \propto \int \rho(x,y)\, e^{-i\Delta\phi_f(x,t)} dxdy \tag{1.5}$$

Alternatively, Eqn. 1.5 can be described in terms of spatial frequency

$$S(k_x) \propto \int \rho(x,y)\, e^{-i2\pi(k_x x)} dxdy \tag{1.6}$$

where k_x the spatial frequency in the x-direction:

$$k_x = \frac{\gamma}{2\pi} \int_0^t G(t')dt' \tag{1.7}$$

By means of a one-dimensional inverse Fourier transform, the spin density can be resolved in the x dimension:

$$\rho(x) \propto \int S(k_x) e^{i2\pi k_x x}\, dk_x. \qquad 1.8$$

Equation 1.8 states that if measurements of the signal are made at different spatial frequency k_x, then spin density can be resolved in the x direction. This can be done by multiple measurements throughout the duration of the frequency encoding gradient.

1.1.2 Phase Encoding

The spatial location of the spin density can be obtained in the y dimension using phase encoding. In this process a gradient is briefly applied in the y direction in-between excitation and the acquisition of signal. Again, the presence of this gradient (G_y) causes the precessional frequency to vary as a function of position (y):

$$\omega(y) = \gamma(B_0 + G_y(t)y). \qquad 1.9$$

Applying a phase encoding gradient for a duration Δt prior to an acquisition results in the spin density accumulating spatially varying phase ($\Delta\phi_p$):

$$\Delta\phi_p(y) = -y\gamma \int_0^{\Delta t} G_y(t')\, dt' \qquad 1.10$$

This phase accrual is identical to that seen in Eqn 1.4. After demodulation of ω_0, the detected signal is now the integral of the product of the spin density and frequency and phase gradient induced phase terms:

$$S \propto \int \rho(x,y)\, e^{-i(\Delta\phi_f(x,t)+\Delta\phi_p(y,t))} dxdy \qquad 1.11$$

or

$$S(k_x, k_y) \propto \int \rho(x,y)\, e^{-i2\pi(k_x x + k_y y)} dxdy \qquad 1.12$$

where k_y the spatial frequency in the y-direction:

$$k_y = \frac{\gamma}{2\pi}\int_0^t G_y(t')dt'. \qquad 1.13$$

By means of a two-dimensional inverse Fourier transform, the spin density can be resolved in the x dimension:

$$\rho(x, y) \propto \int S(k_x, k_y)e^{i2\pi(k_x x + k_y y)}dk_x dk_y. \qquad 1.14$$

Equation 1.14 states that if measurements of the signal are made at different spatial frequency k_x and k_y, then spin density can be resolved in the x and y direction. In order to acquire different k_y spatial frequency, repeated frequency encoded acquisitions using different G_y gradients (Eqn. 1.13) are required. This repetitive process limits the speed MR images can be acquired.

1.1.3 k-space

Figure 1.1 summarizes the encoding process. In the absence of gradients (Figure 1.1), only the center point of k-space is sampled. This results in signal that cannot be spatially resolved. By applying a frequency gradient and acquiring data throughout the duration of the gradient (Figure 1.1b), the center line of k-space is now sampled resulting in signal that can be resolved in one dimension. Resolving an image in two dimensions requires the use of phase encoding gradients. The application of a phase encoding gradient in the y direction prior to applying frequency encoding results in a off-centered line of k-space being sampled. Repeated acquisitions in the presence of different phase encoding gradients will sample k_y space. Once the k_y dimension has been adequately sampled, the image can be resolved in both dimensions (Figure 1.1c).

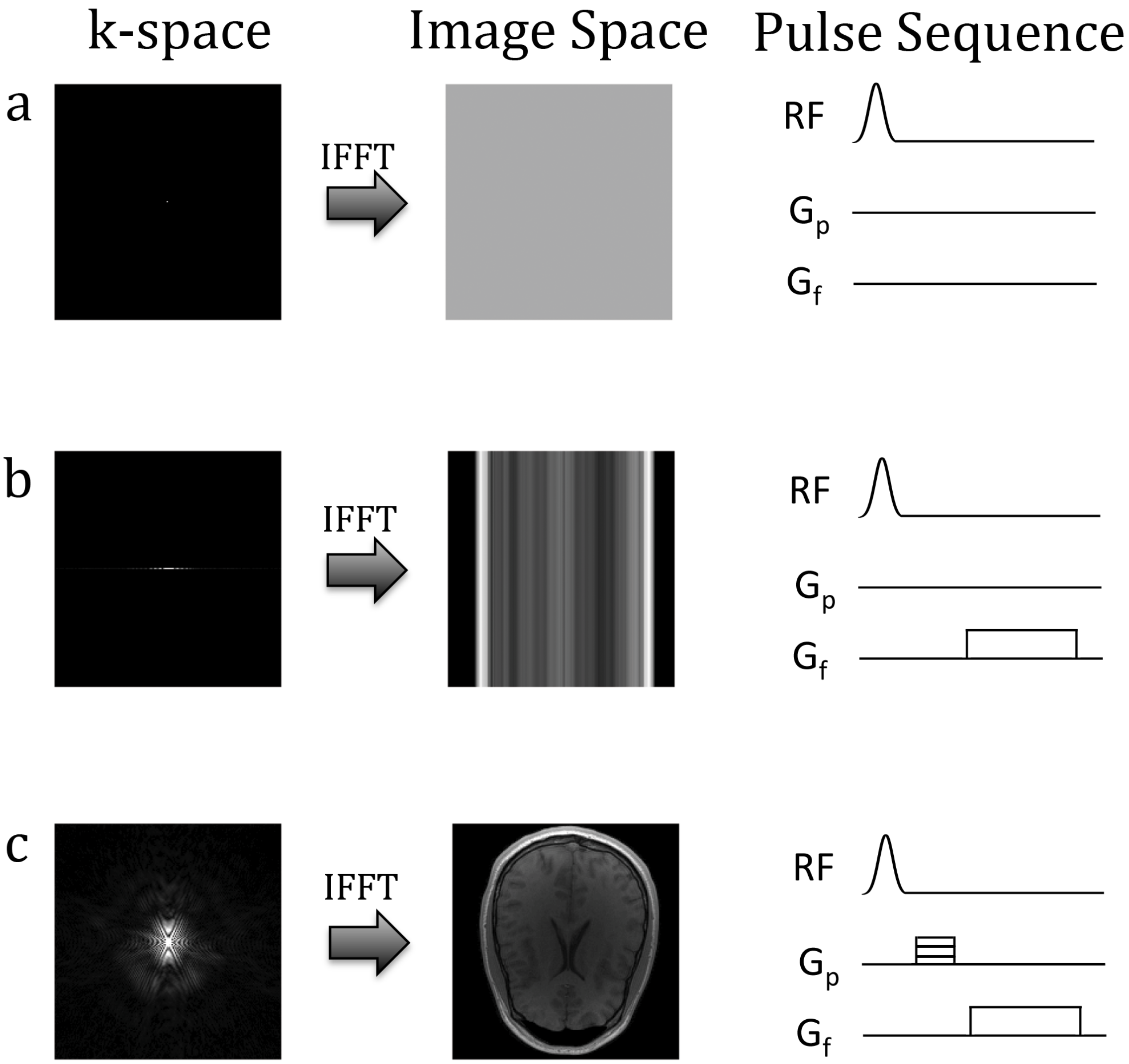

Figure 1.1 The encoding process. a) In the absence of gradients, only the central point of k-space can be sampled. As a result signal cannot be spatially resolved. b) Application of a frequency encoding gradient allows the central line of k-space to be sampled and the image to be resolved in the frequency encode direction. c) To resolve the entire image, the entire k-space must be sampled. Repeated acquisitions are required using different phase encode gradients to sample different lines of k-space.

1.2 Parallel Imaging

Magnetic Resonance (MR) images are acquired by sampling a Fourier space known as k-space where the spacing between adjacent samples in k-space (Δk) defines the field of view (FOV) of the image

$$FOV = \frac{1}{\Delta k} \qquad 1.15$$

and the largest k-space position measured ($k_{x,max}$, $k_{y,max}$) defines its resolution

$$\delta = \frac{1}{2k_{max}} \qquad 1.16$$

Figure 1.2 illustrates these principles. For a given field of view and resolution, the number of phase encodes required is fixed. In parallel imaging, a portion of the k-space phase encodes is not sampled which should result in an aliased image (Figure 1.2b). However, by using multiple surface coils and their known coil sensitivities, the missing phase encodes can be reconstructed (8-10).

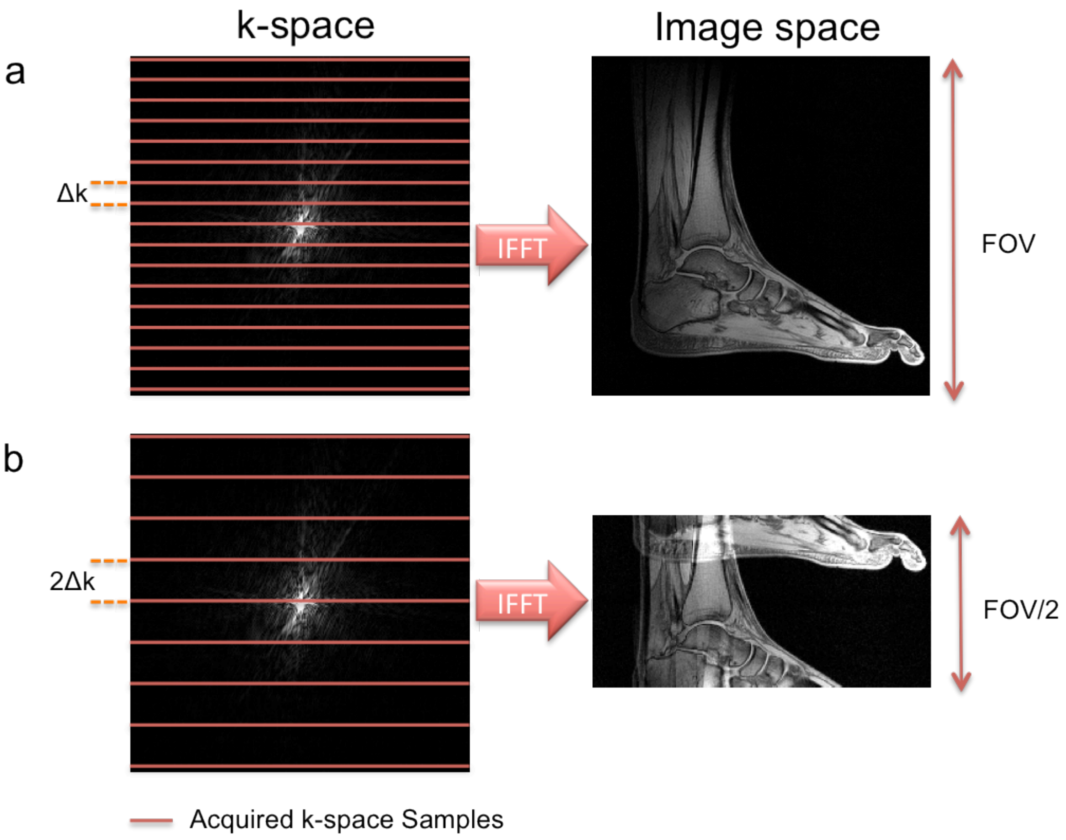

Figure 1.2 Relationship between k-space and image space. a) The field-of-view of an image is proportional to the inverse of the spacing between adjacent samples (Δk) while the resolution is proportional to the max k-space position. b) In the case where only half of the phase encodes are acquired, the final image will be a field-of-view reduced by a factor of two resulting in aliasing.

Parallel imaging techniques fall into one of two categories: k-space (8,9) and image-space techniques (10). In k-space techniques, the missing k-space lines are reconstructed and an inverse Fourier transform results in the reconstructed image. In image-space techniques, the undersampled k-space is Fourier transformed to give an aliased image. The aliased image is then un-aliased by means of the coil sensitivity to reconstruct the image. The common feature of all parallel imaging reconstructions is that the spatial information contained in the sensitivity profile of each coil is being used to partially replace phase encoding, thereby reducing scan time. In the sections to follow surface coil arrays and coil sensitivity, sensitivity encoding principles, the conjugate gradient SENSE parallel imaging reconstruction, and methods to measure SNR in parallel imaging will be described.

1.2.1 Coil Arrays and Coil Sensitivities

Arrays of surface coils can offer significant advantages in MR acquisitions including higher SNR and accelerated image acquisition through the use of parallel imaging. Each surface coil has a non-uniform receive profile, known as its coil sensitivity, which modulates the signal intensity across the field of view. Therefore, the signal intensity S($\mathbf{r}$) measured at any position r will be the product of the coil sensitivity C($\mathbf{r}$) and the underlying spin density ρ($\mathbf{r}$):

$$S(\boldsymbol{r}) \propto C(\boldsymbol{r})\rho(\boldsymbol{r}) \qquad 1.17$$

Figure 1.3 shows the coil sensitivities and resulting coil and coil-combined images for an 8 channel torso array.

Multiple methods exist to calculate the coil sensitivity of a surface coil. Although it is possible to directly calculate coil sensitivities directly from the Biot-Savart Law (11), practical considerations typically restrict coil sensitivities to being estimated directly from acquired data. Coil sensitivities are estimated using either a volume coil (10) or root sum squared approach (10,12).

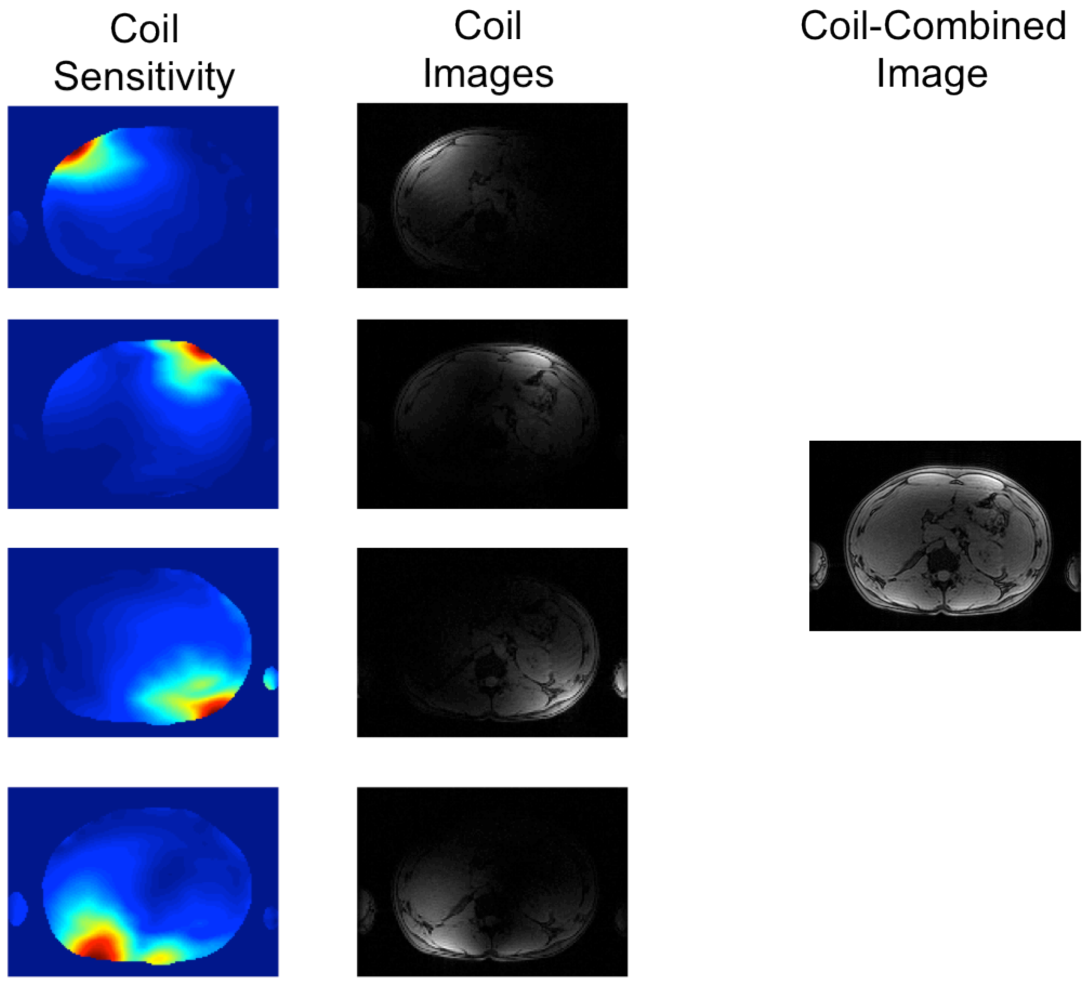

Figure 1.3 Four coil sensitivities, individual coil images, and the coil-combined image for an 8 channel torso array. Signal variation across the field of view caused by the coil sensitivity results in elevated signal intensity in locations near each surface coil and low signal intensities in locations far from each surface coil.

In the volume coil approach, an additional scan is taken using a volume coil (which is assumed to have a uniform sensitivity profile). The coil sensitivity can then be estimated as the ratio of the signal intensity of the surface coil and the volume coil. This technique is sensitive to motion. Any motion between these two separate acquisitions will result in errors in the coil sensitivity estimate.

In the root sum square approach, the root-sum square (RSS) of the each of the surface coils is calculated resulting in an image that is roughly uniform. The coil sensitivity is then estimated as the ratio of the signal intensity of the surface coil and the RSS image. For a small number of coils (ie. <8 coils), the assumption that the RSS image has uniform signal intensity (ie. no coil sensitivity weighting) is a good approximation. However, for large arrays this assumption breaks down in regions near the coils, resulting in errors in the coil sensitivity estimations.

1.2.2 Sensitivity Encoding Principles

In the case that surface coils are used, Eqn. 1.14 needs to be modified to account for the coil sensitivity. The signal measured at k-space position **k** by the lth receive coil can be described as

$$S_l(\boldsymbol{k}) = \int \rho(\boldsymbol{r}) C_l(\boldsymbol{r})\, e^{-\boldsymbol{i2\pi}(\boldsymbol{k}\cdot\boldsymbol{r})} d\boldsymbol{r} \qquad 1.18$$

where $\rho(\mathbf{r})$ is the spin density and $C_l(\mathbf{r})$ is the coil sensitivity. Combining the coil sensitivity and Fourier encoding creates encoding functions that differ for each coil:

$$E_l(\boldsymbol{k}, \boldsymbol{r}) \equiv C_l(\boldsymbol{r}) e^{-i2\pi(\boldsymbol{k}\cdot\boldsymbol{r})} \qquad 1.19$$

Alternatively, Eqn. 1.18 can be discretized and described in matrix form:

$$S_q = \sum_p E_{qp} \rho_p \qquad 1.20$$

$$\boldsymbol{S} = E\boldsymbol{\rho} \qquad 1.21$$

where **S** is a vector of k-space values with element $S_q = S_l(k)$ such that every combination of k-space index, k, and coil index, l, map onto index q, $\boldsymbol{\rho}$ is a vector of spin density with elements ρ_p at position index p, and E is the encoding matrix, consisting of the coil sensitivity and Fourier encoding, a matrix with elements

$$E_{qp} \equiv C_l(r_p) e^{-2\pi k r_p} \qquad 1.22$$

1.2.3 Conjugate Gradient SENSE Reconstruction

In general, the encoding matrix in Eqn 1.21 is large and difficult to invert. In such cases, an iterative approach such as conjugate gradient SENSE (CG-SENSE(13)) offers an efficient method of solving Eqn. 1.21. By using CG-SENSE, the inversion of the encoding matrix can be avoided. CG-SENSE also yields an exact solution, provided sufficient iterations are done (13). In practice a sufficient accurate approximation can be achieved after relatively few iterations, significantly reducing reconstruction times (13).

1.2.4 SNR Measurements

The cost of acceleration using parallel imaging is reduced SNR resulting from two effects: reduced signal averaging results in a loss of SNR by a factor of the square root of the acceleration factor and an additional penalty called the g-factor (10) which describes the additional noise amplification caused by the parallel imaging reconstruction. This g-factor is dependent on the sampling strategy and the design of the coil array (number of coils and geometry of the coils in the array). In addition, this g-factor penalty varies spatially making the conventional method for SNR measurement, which relies on a ROI from a signal free region to estimate the noise, invalid. Existing methods for measuring SNR in a parallel imaging reconstruction include direct SNR calculations (7,10), multiple pseudo-replica (14), and estimation from multiple acquisitions (15-17).

Analytical methods for “direct SNR calculation” have been proposed (7,10). Here, direct inversion of the encoding matrix allows SNR scaled images to be reconstructed. However, inversion of the encoding matrix is not computationally feasible for an arbitrary sampling pattern or parallel imaging reconstruction. Typically this method has been restricted to uniform or 1d undersampling patterns, situations where this inversion can be simplified.

Multiple methods (15-17) have been proposed for SNR estimates using the repeated acquisition of the same images. The National Electrical Manufacturers Association (NEMA) standard proposed one such method (15) where the difference between two replica images is taken to produce a difference image. Image noise can then be estimated from ROIs within the difference images using the following formula

$$Noise = \left[\frac{\sum_{i=1}^{n}\sum_{j=1}^{m-1}(V(i,j+1)-V(i,j))^2}{4\sum_{i=1}^{n}(m-1)}\right] \qquad 1.23$$

where n and m are the number of rows and columns within the ROI and V(i,j) is the signal intensity of the difference image at pixel location [i,j]. These techniques assume that each replica is identical except for the noise, making these techniques sensitive to variations between acquisitions (such as motion and radiofrequency instability). In particular, sensitivity to motion (even motion on the order of a voxel) makes repeated acquisition techniques impractical for *in vivo* imaging.

The Monte-Carlo based “pseudo-multiple replica” (14) approach offers a statistical approach to measure SNR. Figure 1.4 describes this approach. Properly scaled and correlated synthetic Gaussian noise is added to the acquired k-space data and the resulting image is reconstructed. The process is repeated many times (typically 128) resulting in a stack of replica images. For each pixel, the standard deviation is measured through the stack of replica images to generate a noise-only image. Dividing the original image by the noise-only image then forms an SNR map. This method is applicable to all linear parallel imaging reconstructions with arbitrary sampling patterns. The need to reconstruct each of the replica images requires lengthy reconstruction times.

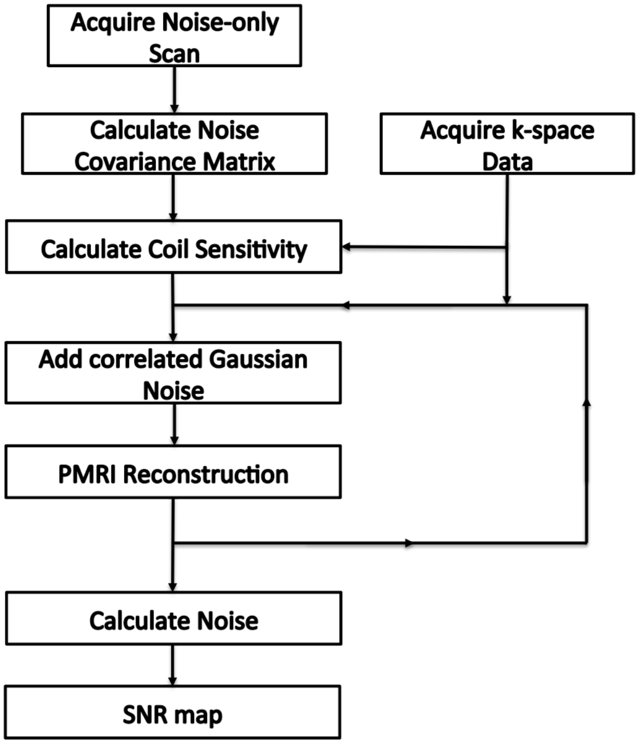

Figure 1.4 Flowchart of the multiple-pseudo replica method.

1.3 Compressed Sensing

Compressed Sensing (CS) has been proposed as an alternative approached to image acceleration. Instead of relying on spatially-varying coil sensitivities, transform sparsity of the MR image is exploited allowing the image to be recovered from significantly undersampled datasets. The concept of transform sparsity has been successfully used for data compression of pictures. Commonly-used image formats such as JPEG transform images into sparse representations where only the important coefficients are stored (18). CS attempts to recover these important coefficients from undersampled datasets (19). In the paragraphs to follow, the conditions required for a successful CS reconstruction are explained and the opportunity to combine compressed sensing with parallel imaging is discussed.

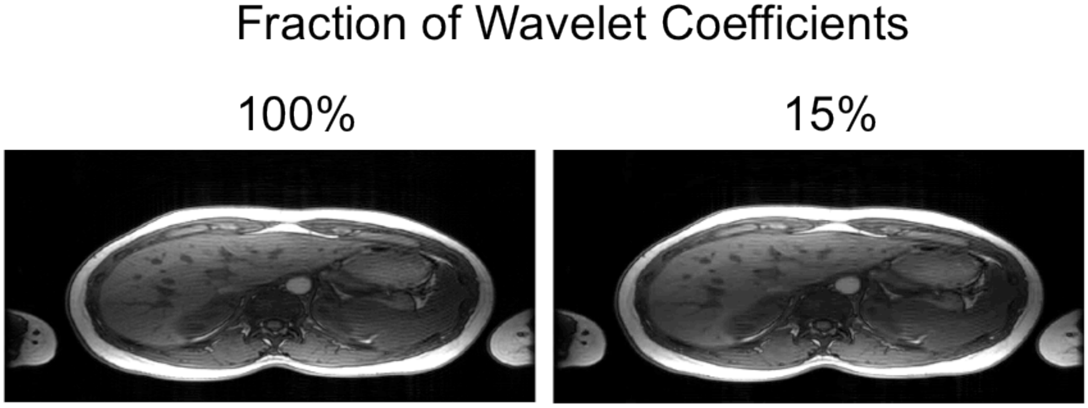

Figure 1.5 Sparsity of a liver dataset in the wavelet domain. Images reconstructed using the largest 15% of the wavelet coefficients and 100% of the coefficients show excellent agreement.

The first requirement for a CS reconstruction is that the MR image must be sparse in a known transform domain. Sparsity refers to the ability of an image to be described by relatively few non-zero coefficients. Typically transform sparsity rather than image sparsity is enforced, meaning that the image can be described by a few non-zero coefficients in a transform domain. Two commonly used transform domains for MR images are wavelet and finite difference. In Figure 1.5, the sparsity of a liver dataset in the wavelet domain is shown. Using the largest 15% of the coefficient in the wavelet domain, the image can be recovered with excellent fidelity.

The second requirement is that the aliasing artifact is incoherent. As previously mentioned, the MR images are acquired by sampling k-space. By random sampling k-space phase-encodes, an incoherent artifact can be introduced. However, most of the energy of an MR image is contained in the center of the k-space (Figure 1.1). Variable density random sampling patterns where more k-space samples are acquired in the center of k-space are commonly used (19). Figure 1.6 shows the effect of variable density random sampling patterns vs random sampling patterns.

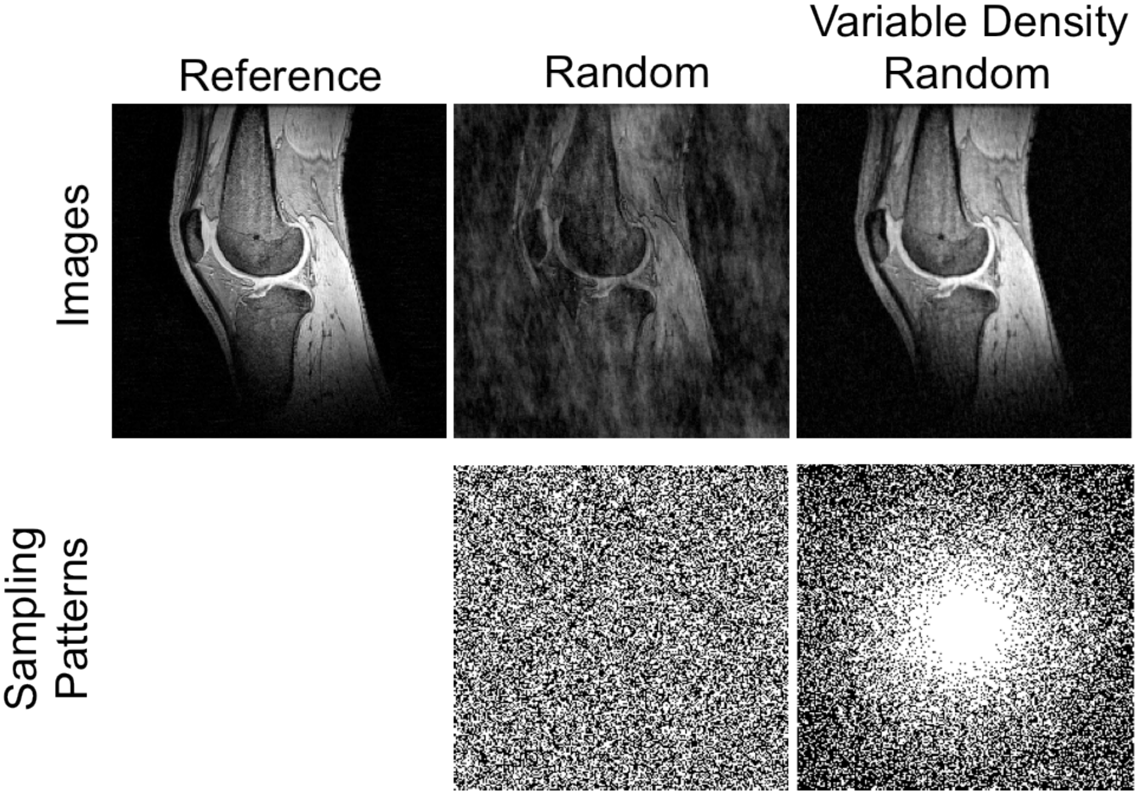

Figure 1.6 Knee Images reconstructed using random and variable density random at an acceleration factor of 2. Use of a variable density random sampling pattern significantly reduces the artifact introduced by undersampling.

The final requirement is a non-linear reconstruction that enforces both sparsity of the reconstructed image and consistency of the reconstructed image with the acquired data. This criterion can be meet by solving the following convex optimization problem:

$$\underset{m}{argmin} = ||F_U m - y||_2^2 + \lambda||\Psi m||_1 \tag{1.24}$$

where F_U is the undersampled Fourier operator, m is the image, y is the undersampled k-space data, Ψ is the sparsity transform, and λ is the sparsity weighting. Here the first component of Eqn. 1.24 enforces consistency of the reconstructed image with the acquired data and the second promotes sparsity of the image in its sparsifying transform domain. The regularization parameter, λ, scales the relative importance between data consistency and sparsity.

Compressed sensing has been shown to be a complimentary approach to parallel imaging for image acceleration (20,21). In such methods, Fourier encoding is again replaced with the hybrid encoding described by Eqn. 1.19 in a non-linear reconstruction that promotes sparsity. The combination of both parallel imaging and compressed sensing has been shown to reduce the g-factor penalty paid by parallel imaging reconstructions. Using both, acceleration factors can be achieved that are higher than either compressed sensing or parallel imaging on their own.

1.4 Water-Fat Imaging

Water and fat are the two prominent sources of signal in *in vivo* applications of MRI. Water and fat exhibit a difference in resonance frequencies called a chemical shift. Electrons surrounding any molecule shield the hydrogen nuclei from an external magnetic field causing small but measurable perturbations in the magnetic field experienced by the ^{1}H nuclei. These perturbations to the magnetic field are different for fat and water molecules and result in resonance frequencies that differ by 3.4ppm (22,23). At 3T, this results in a 434Hz difference between the resonance frequency of water and fat (Figure 1.7). This difference can be exploited, allowing separation of signal due to water from signal due to fat.

Chemical shift imaging typically refers to spatially resolved spectroscopy where free induction decays are readout and the spatial location is phase encoded in 2 or 3 dimension. Dixon-based chemical shift methods assume that the chemical shift between water and fat is known *a priori.* This assumption significantly reduces the spectral information required to separate water and fat. In this section, the Dixon-based chemical imaging methods, henceforth referred to as chemical shift imaging, used to separate water and fat signals will be introduced and their limitations discussed.

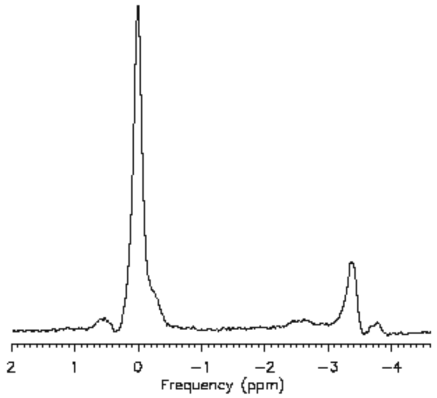

Figure 1.7 Spectrum taken from the liver of a patient with non-alcoholic fatty liver disease. The spectrum shows the 3.4ppm chemical shift between water (left) and fat (right).

1.4.1 Two-Point Dixon

At any particular pixel p and echo time t, the total signal $S_p(t)$ can be considered as the sum of the signal from fat protons, $\rho_{f,p}$, with the signal from water protons, $\rho_{w,p}$:

$$S_p(t) = \rho_{w,p} + \rho_{f,p} e^{i2\pi \Delta f t} \tag{1.25}$$

where Δf is the chemical shift between water and fat. At t=0, the transverse components of fat and water are in phase with one another (24). As time progresses, the fat and water signal will dephase due their chemical shift. If two images are acquired at echo times when the water and fat signal are in-phase (S_{IP}) and 180° out-of-phase (S_{OP}), then simple addition and subtraction of the in-phase and out-of-phase images results in a water-only and fat-only images (25):

$$S_W = \frac{1}{2}(S_{IP} + S_{OP}) \tag{1.26}$$

$$S_F = \frac{1}{2}(S_{IP} - S_{OP}) \tag{1.27}$$

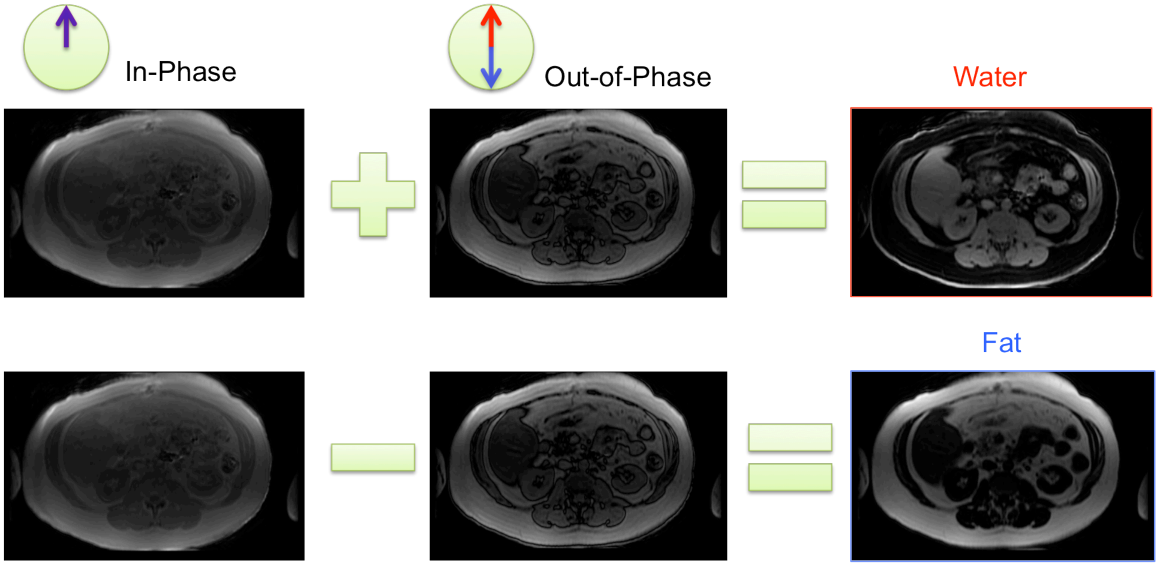

Figure 1.8 Illustration of the Two Point Dixon Method. Water-only and fat-only images are produced by the sum or difference of in-phase and out-of-phase images.

Figure 1.8 demonstrates this technique using in-phase and out-of-phase images taken from the abdomen. This approach assumes that the magnetic field is homogeneous, an assumption that in practice is never true.

1.4.2 Three-Point Dixon

In the presence of non-uniform magnetic field, additional phase will accumulate due to the magnetic field inhomogeneity:

$$S_p(t) = (\rho_{w,p} + \rho_{f,p} e^{i2\pi\Delta f t}) e^{i2\pi\psi_p t} \tag{1.28}$$

Here ψ_p is the field map, a measure of B_0 inhomogeneity in units of Hz. Under such conditions, the two-point approach will not provide accurate water-only and fat-only images. A modified approach to correct for the field inhomogeneity was proposed (26). In this approach, a third image is acquired when the relative phase between fat and water is $-\pi$. The two out-of-phase images can then be used to measure the phase offset at each pixel due to magnetic field inhomogeneity (Figure 1.9).

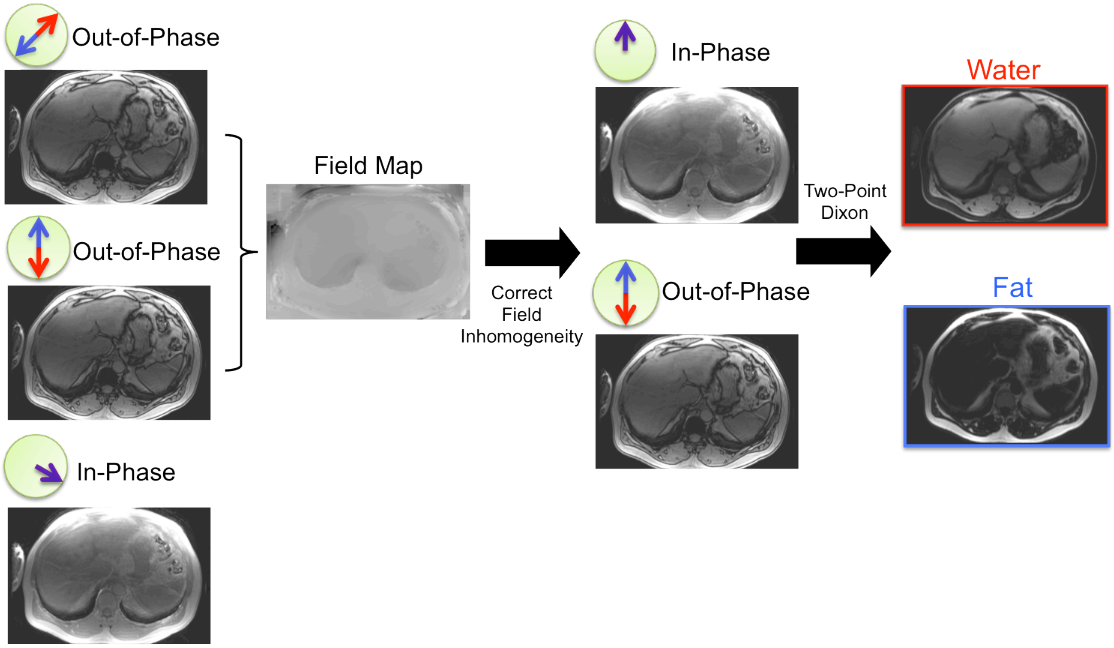

Figure 1.9 Illustration of the three-point Dixon technique. At each voxel, the difference in phase between the two out-of-phase images is only due to B_0 inhomogeneity. By using two out-of-phase images an estimate the field map, a measure of the B_0 inhomogeneity, can be made. This field map is used to correct the phases of the in-phase and out-of-phase images. The two-point Dixon technique is now used on the corrected images.

1.4.3 IDEAL

A method called Iterative Decomposition of water and fat with Echo Asymmetric and Least-squares estimation (IDEAL) has been proposed as a generalized version of the three-point Dixon technique (27). In this technique, 3 or more images are acquired with arbitrary phase shifts. The increased flexibility in the choice of phase shifts allows for SNR optimal phase-shifts to be used thereby providing improved SNR (28,29). Unlike prior work, which solved signal model analytically by restricting echo times, the IDEAL approach separates water and fat on a pixel basis using an iterative least-square approach. The IDEAL method is described in Figure 1.10.

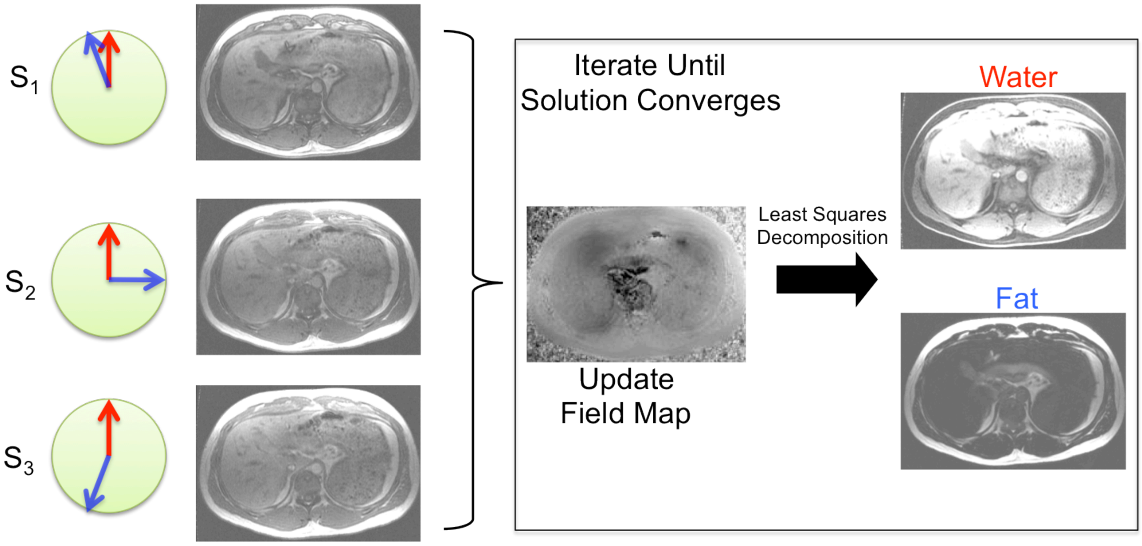

Figure 1.10 IDEAL water-fat separation technique. Images are acquired with at least three different echo times (with different phases between fat and water). A process of updating the field map followed by a least squares decomposition to produce water-only and fat-only images is repeated until the convergence has been achieved.

1.4.4 Quantitative Water-Fat Imaging

The clinical need for techniques to quantify fat has driven the development of quantitative chemical shift based water-fat techniques. The proton density fat-fraction (PDFF) defined as the ratio of the density of mobile protons from fat to the total density of mobile protons from both fat and water has emerged as the most commonly used and most biologically relevant imaging biomarker for tissue fat concentration (30). Unfortunately, many factors affect the signal intensities of fat and water. These confounding factors result in biased estimates of the PDFF and must be accounted for in order to achieve accurate estimates. These factors include T_1 bias (31,32), accurate spectral modeling (22,23,32), and R_2^* correction (32-34).

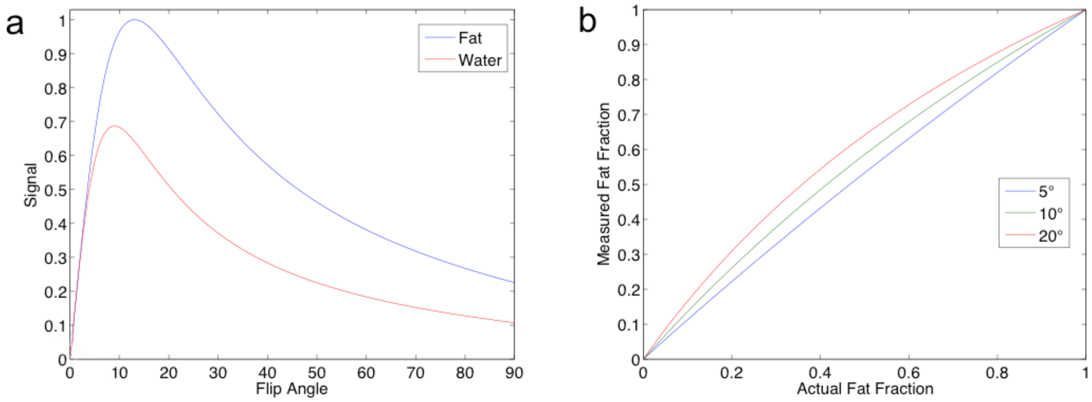

Figure 1.11a) Simulated fat and water signal behaviour of a SPGR sequence as a function of flip angle assuming $T_{1,fat}$=382ms, $T_{1,water}$=809ms, and TR=10ms. b) Simulated fat fraction at flip angles of 5°,10°, and 20°. As flip angles increases, the deviation between measured fat fraction and actual fat fraction increases.

T_1 bias in the PDFF arises from the difference in T_1 of fat and water. In Figure 1.11a shows the behaviour of fat and water signals as a function of flip angles assuming $T_{1,fat}$=382ms and $T_{1,water}$=809ms for a spoiled gradient echo sequence (SPGR). At higher flip angles the water and fat signals becomes more T_1 weighted (Figure 1.11a), resulting in an increased bias in the fat fraction measurement (Figure 1.11b). Therefore, a small flip angle is used to minimize T_1 effects, resulting in reduced bias in the PDFF at the cost of reduced SNR. Alternative approaches have been proposed that use multiple acquisitions at different flip angles to measure the T_1 of fat and water (31,35). However, this approach has been shown to be less efficient than using a small flip angle(36).

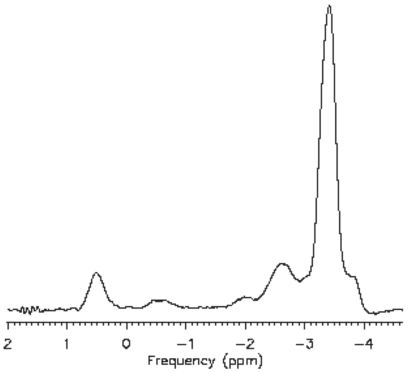

Figure 1.12 Spectrum of a peanut oil phantom. This spectrum shows that fat spectra consist of multiple spectral peaks.

The previously defined signal model Eqn. 1.28 assumes the water and fat spectra are singlets. While this is a good assumption for water, Figure 1.12 shows that the spectrum of fat is complex, consisting of multiple spectral peaks. These additional spectral peaks lead to bias in our fat and water estimates. A more accurate spectral model should contain the additional spectral peaks of fat:

$$S_p(t) = (\rho_{w,p} + \rho_{f,p} \sum_j \alpha_j e^{i2\pi \Delta f_j t}) e^{i2\pi \psi_p t} \qquad 1.29$$

where α_j and f_j are the relative amplitudes and chemical shifts, respectively, of the *j*th spectral peak of fat. The amplitude of each spectral peak of fat could be estimated using IDEAL provided that enough echo images were acquired. Typically, the relative amplitude and frequency of each spectral component of fat is assumed to be known *a priori*.

Unlike the previous discussed confounding factors, T_2^* effects cannot be accounted for using appropriate imaging parameters or prior knowledge. An additional free parameter must be added to the signal model to account for the R_2^* decay (23,33):

$$S_p(t) = (\rho_{w,p} + \rho_{f,p} \sum_j \alpha_j e^{i2\pi \Delta f_j t}) e^{i2\pi (\psi_p + \frac{R_{2,p}^*}{2\pi}) t} \qquad 1.30$$

This additional free parameter requires the acquisition of more than three echo images for accurate and reliable model fitting. Typically six-echo acquisitions have been used to provide a good balance between acquisition time and accurate R_2^* estimation.

1.5 Hyperpolarized C13 Imaging

Hyperpolarized carbon-13 (^{13}C) imaging is an emerging field that enables measurement of *in vivo* metabolism. Using a process called dynamic nuclear polarization (DNP), a ^{13}C labeled substrate with a non-thermal equilibrium distribution of spins in a hyperpolarized state can be produced (37). This hyperpolarized state offers signal enhancement on the order of 10,000 fold over thermal imaging and enhances imaging of ^{13}C substrates (37). The polarized substrates are injected and their metabolic by-products detected. The following sections will discuss: the physics of non-thermal imaging and its impact on imaging strategies and the biochemistry of the most commonly used substrate [1-^{13}C] pyruvate.

1.5.1 Physics of Non-thermal imaging

Many nuclei (eg. ^1H, ^3He, ^{13}C, ^{129}Xe) have a non-zero spin that can be detected by NMR and MRI through the interaction of a nuclear spin with an external magnetic field. For nuclei with a spin quantum number of ½ (e.g. ^1H, ^{13}C), the interactions of spins with an external magnetic field results in two possible spin states, namely, parallel alignment and anti-parallel alignment. The slight preference for any given nuclei to populate the parallel state results in a population difference or polarization P given by:

$$P = \frac{N^+ - N^-}{N^+ + N^-} \approx \frac{h\gamma B_0}{4\pi kT} \tag{1.31}$$

where N^+ and N^- are the number of spins in the parallel and anti-parallel state, γ is the gyromagnetic ratio of the nuclei, h is Planck's constant , k is Boltzmann constant, and T is the temperature. This polarization gives rise to detectable signal.

At thermal equilibrium the polarization is low. For example, at 3T the polarization is only $1x10^{-5}$ for ^1H and $2.5x10^{-6}$ for ^{13}C. In other words, only one out of every one hundred thousand nuclei contribute to the detected ^1H signal. In ^1H MRI the number of *in vivo* nuclei is large due to the high concentration of hydrogen (~88M) (38) and the high natural abundance of the isotope ^{1}H. This makes detection of ^{1}H signal relatively easy despite this low polarization. In ^{13}C MRI the number of spins is much smaller due the lower biological abundance of carbon (approximately 18% by mass) and the low natural abundance of the isotope ^{13}C (1%). As such, detection of ^{13}C signal difficult.

An approach to enhance signal is to temporarily increase the polarization relative to thermal equilibrium resulting in a non-thermal, hyperpolarized state. Polarization increases of more than four orders of magnitude can be obtained through a process called dynamic nuclear polarization (37). In this approach, a ^{13}C labeled substrate is polarized and subsequently injected into the subject.

The increased polarization due to this hyperpolarized state immediately begins to decay back to thermal equilibrium. The rate of this decay is substrate-dependent and is described by the substrate's T_1. This rapid decay limits the time window in which hyperpolarized signal can be detected and makes efficient rapid imaging strategies necessary.

1.5.2 Metabolism of [1-^{13}C] Pyruvate

[1-^{13}C] pyruvate (pyruvate labeled with ^{13}C in the C1 position) is the most commonly used hyperpolarized substrate for multiple reasons. Its central role in metabolism allows for the detection of metabolites from several different metabolic pathways. In addition, its desirable hyperpolarization properties, such as high polarization levels and a relatively long T_1 of ~30s *in vivo* and ~45s *ex-vivo,* improve the quality and life-time of polarization (39,40).

Figure 1.13 shows a ^{13}C spectrum acquired in a mouse liver. In this spectrum, common metabolites of [1-^{13}C] pyruvate including [1-^{13}C] lactate and [1-^{13}C] alanine are observed at 12.7ppm and 5.94ppm. ^{13}C-bicarbonate was not observed. Its expected location is approximation -10.0ppm (41,42). [1-^{13}C] pyruvate's metabolic fate is either one of production of energy (lactate, bicarbonate) or synthesis of amino acids (alanine). The metabolic pathways being probe with hyperpolarized [1-^{13}C] pyruvate are summarized in Figure 1.14.

The ^{13}C spectrum (Figure 1.13) shows that pyruvate and its metabolites exhibit a chemical shift difference that is very similar to the fat-water difference (Figure 1.7). It has been shown that using variants of the IDEAL water-fat separation method (27) can be used to separate ^{13}C metabolites, producing pyruvate-only images, lactate-only images, and alanine-only images (43,44).

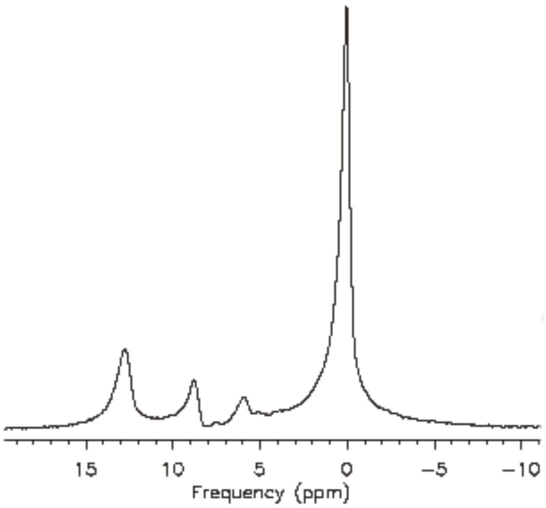

Figure 1.13 Spectrum of a mouse liver after injection of [1-^{13}C] pyruvate. The peaks at 12.7ppm, 8.6ppm, 5.9ppm, 0ppm correspond to lactate, pyruvate-hydrate, alanine, and pyruvate. No bicarbonate (~ -10.6ppm) is observed in this spectrum.

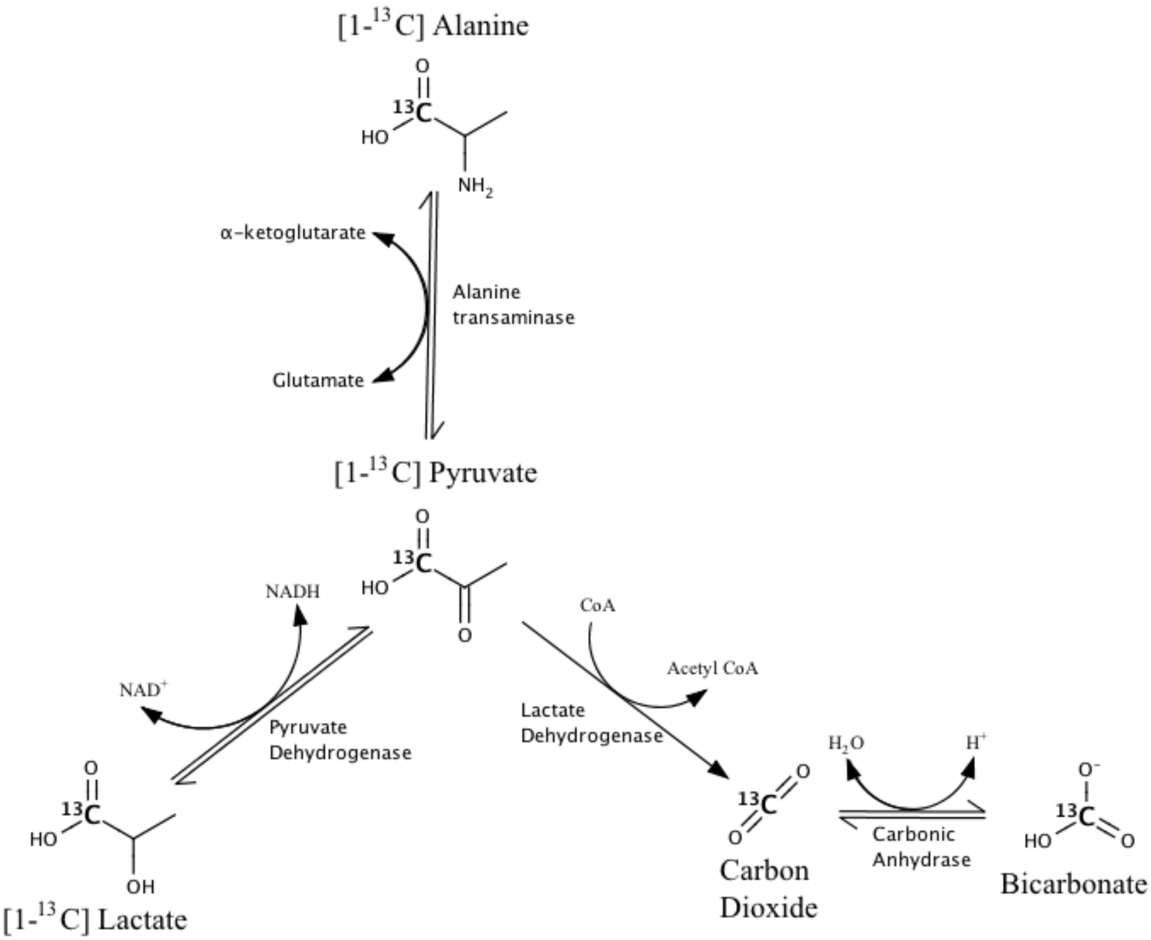

Figure 1.14 Metabolic pathways of [1-^{13}C] Pyruvate. Under anaerobic conditions elevated lactate levels are caused by the conversion of [1-^{13}C] pyruvate into [1-^{13}C] lactate by the enzyme lactate dehydrogenase. Under aerobic conditions, pyruvate and Coenzyme A (CoA) are converted into Acetyl CoA and $^{13}CO_2$ by pyruvate dehydrogenase. The $^{13}CO_2$ can then form ^{13}C-bicarbonate through carbonic anhydrase. [1-^{13}C] pyruvate can be converted into the amino acid [1-^{13}C] alanine through alanine transaminase.

1.6 Thesis Outline

In Chapter 2, a new approach to SNR measurements for parallel imaging reconstructions is proposed. This new method builds off of two existing techniques: pseudo multiple replica and the NEMA standard for SNR measurements. Unlike previous methods, this method has the following properties: applicable to all parallel imaging reconstructions, computationally rapid, and requires only one image acquisition.

In Chapter 3, an integrated compressed sensing, parallel imaging, R_2^* corrected water-fat separation technique for water-fat imaging of highly accelerated acquisitions is described. The technique is demonstrated using a customized IDEAL-SPGR pulse sequence to acquire retrospectively and prospectively undersampled datasets of the liver, calf, knee, and abdominal cavity. At high acceleration factors, this technique is shown to offer improved image quality over parallel imaging.

In Chapter 4, an integrated compressed sensing, metabolite separation technique for separation of pyruvate and its metabolites, lactate, alanine, and bicarbonate is described. The technique was validated using phantom and *in vivo* experiments using a broadbanded variant of the IDEAL-SPGR sequence.

Chapter 5 provides a summary of the material presented in this thesis. In addition, future work and potentially applications are discussed.

1.7 References

1. Hussain HK, Chenevert TL, Londy FJ, Gulani V, Swanson SD, McKenna BJ, Appelman HD, Adusumilli S, Greenson JK, Conjeevaram HS. Hepatic fat fraction: MR imaging for quantitative measurement and display--early experience. Radiology 2005;237(3):1048-1055.

2. Schick F, Einsele H, Lutz O, Claussen CD. Lipid selective MR imaging and localized 1H spectroscopy of bone marrow during therapy of leukemia. Anticancer Res 1996;16(3B):1545-1551.

3. Schick F, Weiss B, Einsele H. Magnetic resonance imaging reveals a markedly inhomogeneous distribution of marrow cellularity in a patient with myelodysplasia. Ann Hematol 1995;71(3):143-146.

4. Kuk JL, Katzmarzyk PT, Nichaman MZ, Church TS, Blair SN, Ross R. Visceral fat is an independent predictor of all-cause mortality in men. Obesity (Silver Spring) 2006;14(2):336-341.

5. Hu HH, Perkins TG, Chia JM, Gilsanz V. Characterization of human brown adipose tissue by chemical-shift water-fat MRI. AJR Am J Roentgenol 2013;200(1):177-183.

6. Hu HH, Yin L, Aggabao PC, Perkins TG, Chia JM, Gilsanz V. Comparison of brown and white adipose tissues in infants and children with chemical-shift-encoded water-fat MRI. J Magn Reson Imaging 2013.

7. Kellman P, McVeigh ER. Image reconstruction in SNR units: a general method for SNR measurement. Magn Reson Med 2005;54(6):1439-1447.

8. Griswold MA, Jakob PM, Heidemann RM, Nittka M, Jellus V, Wang J, Kiefer B, Haase A. Generalized autocalibrating partially parallel acquisitions (GRAPPA). Magn Reson Med 2002;47(6):1202-1210.

9. Sodickson DK, Manning WJ. Simultaneous acquisition of spatial harmonics (SMASH): fast imaging with radiofrequency coil arrays. Magn Reson Med 1997;38(4):591-603.

10. Pruessmann KP, Weiger M, Scheidegger MB, Boesiger P. SENSE: sensitivity encoding for fast MRI. Magn Reson Med 1999;42(5):952-962.

11. Jin J, Liu F, Weber E, Li Y, Crozier S. An electromagnetic reverse method of coil sensitivity mapping for parallel MRI - theoretical framework. J Magn Reson 2010;207(1):59-68.

12. McKenzie CA, Yeh EN, Ohliger MA, Price MD, Sodickson DK. Self-calibrating parallel imaging with automatic coil sensitivity extraction. Magn Reson Med 2002;47(3):529-538.

13. Pruessmann KP, Weiger M, Bornert P, Boesiger P. Advances in sensitivity encoding with arbitrary k-space trajectories. Magn Reson Med 2001;46(4):638-651.

14. Robson PM, Grant AK, Madhuranthakam AJ, Lattanzi R, Sodickson DK, McKenzie CA. Comprehensive quantification of signal-to-noise ratio and g-factor for image-based and k-space-based parallel imaging reconstructions. Magn Reson Med 2008;60(4):895-907.

15. NEMA. Determination of signal-to-noise ratio (SNR) in diagnostic magnetic resonance imaging. Rosslyn, VA; 2001.

16. Reeder SB, Wintersperger BJ, Dietrich O, Lanz T, Greiser A, Reiser MF, Glazer GM, Schoenberg SO. Practical approaches to the evaluation of signal-to-noise ratio performance with parallel imaging: application with cardiac imaging and a 32-channel cardiac coil. Magn Reson Med 2005;54(3):748-754.

17. Dietrich O, Raya JG, Reeder SB, Reiser MF, Schoenberg SO. Measurement of signal-to-noise ratios in MR images: influence of multichannel coils, parallel imaging, and reconstruction filters. J Magn Reson Imaging 2007;26(2):375-385.

18. Taubman D, Marcellin M. Image compression fundamentals, standards and practice. Kluwer Internation Series in Engineering and Computer Science: Kluwer Academic Publishers; 2002.

19. Lustig M, Donoho D, Pauly JM. Sparse MRI: The application of compressed sensing for rapid MR imaging. Magn Reson Med 2007;58(6):1182-1195.

20. Lustig M, Alley M, Vasanawala S, Donoho D, Pauly JM. L1 SPIR-iT: Autocalibrating Parallel Imaging Compressed Sensing. Proceedings of the 17th Annual Meeting of ISMRM, Honolulu, USA 2009:379.

21. Liang D, Liu B, Wang J, Ying L. Accelerating SENSE using compressed sensing. Magn Reson Med 2009;62(6):1574-1584.

22. Hamilton G, Yokoo T, Bydder M, Cruite I, Schroeder ME, Sirlin CB, Middleton MS. In vivo characterization of the liver fat (1)H MR spectrum. NMR Biomed 2011;24(7):784-790.

23. Yu H, Shimakawa A, McKenzie CA, Brodsky E, Brittain JH, Reeder SB. Multiecho water-fat separation and simultaneous R2* estimation with multifrequency fat spectrum modeling. Magn Reson Med 2008;60(5):1122-1134.

24. Bydder M, Yokoo T, Yu H, Carl M, Reeder SB, Sirlin CB. Constraining the initial phase in water-fat separation. Magn Reson Imaging 2011;29(2):216-221.

25. Dixon WT. Simple proton spectroscopic imaging. Radiology 1984;153(1):189-194.

26. Glover GH, Schneider E. Three-point Dixon technique for true water/fat decomposition with B0 inhomogeneity correction. Magn Reson Med 1991;18(2):371-383.

27. Reeder SB, Wen Z, Yu H, Pineda AR, Gold GE, Markl M, Pelc NJ. Multicoil Dixon chemical species separation with an iterative least-squares estimation method. Magn Reson Med 2004;51(1):35-45.

28. Pineda AR, Reeder SB, Wen Z, Pelc NJ. Cramer-Rao bounds for three-point decomposition of water and fat. Magn Reson Med 2005;54(3):625-635.

29. Chebrolu VV, Yu H, Pineda AR, McKenzie CA, Brittain JH, Reeder SB. Noise analysis for 3-point chemical shift-based water-fat separation with spectral modeling of fat. J Magn Reson Imaging 2010;32(2):493-500.

30. Reeder SB, Hu HH, Sirlin CB. Proton density fat-fraction: a standardized MR-based biomarker of tissue fat concentration. J Magn Reson Imaging 2012;36(5):1011-1014.

31. Liu CY, McKenzie CA, Yu H, Brittain JH, Reeder SB. Fat quantification with IDEAL gradient echo imaging: correction of bias from T(1) and noise. Magn Reson Med 2007;58(2):354-364.

32. Bydder M, Yokoo T, Hamilton G, Middleton MS, Chavez AD, Schwimmer JB, Lavine JE, Sirlin CB. Relaxation effects in the quantification of fat using gradient echo imaging. Magn Reson Imaging 2008;26(3):347-359.

33. Yu H, McKenzie CA, Shimakawa A, Vu AT, Brau AC, Beatty PJ, Pineda AR, Brittain JH, Reeder SB. Multiecho reconstruction for simultaneous water-fat decomposition and T2* estimation. J Magn Reson Imaging 2007;26(4):1153-1161.

34. Chebrolu VV, Hines CD, Yu H, Pineda AR, Shimakawa A, McKenzie CA, Samsonov A, Brittain JH, Reeder SB. Independent estimation of T*2 for water and fat for improved accuracy of fat quantification. Magn Reson Med 2010;63(4):849-857.

35. Karampinos DC, Yu H, Shimakawa A, Link TM, Majumdar S. T(1)-corrected fat quantification using chemical shift-based water/fat separation: application to skeletal muscle. Magn Reson Med 2011;66(5):1312-1326.

36. Wiens CN, Addeman BT, Kisch SJ, Hines CD, Yu H, Brittain JH, Reeder SB, McKenzie CA. Quantification of Noise Efficiency with T1 corrected IDEAL

Spoiled Gradient Imaging. Proceedings of the 17th Annual Meeting of ISMRM, Honolulu, USA 2009:656.

37. Ardenkjaer-Larsen JH, Fridlund B, Gram A, Hansson G, Hansson L, Lerche MH, Servin R, Thaning M, Golman K. Increase in signal-to-noise ratio of > 10,000 times in liquid-state NMR. Proc Natl Acad Sci U S A 2003;100(18):10158-10163.

38. Haacke EM, Brown RW, Thompson MR, Venkatesan R. Magnetic Resonance Imaging: Physical Principles and Sequence Design. New York: Wiley-Liss; 1999.

39. Ardenkjaer-Larsen JH, Macholl S, Johannesson H. Dynamic nuclear polarization with trityls at 1.2 K. Applied Magnetic Resonance 2008;34(3-4):509-522.

40. Golman K, in 't Zandt R, Thaning M. Real-time metabolic imaging. Proc Natl Acad Sci U S A 2006;103(30):11270-11275.

41. Lee P, Leong W, Tan T, Lim M, Han W, Radda GK. In vivo hyperpolarized carbon-13 magnetic resonance spectroscopy reveals increased pyruvate carboxylase flux in an insulin-resistant mouse model. Hepatology 2013;57(2):515-524.

42. Schroeder MA, Cochlin LE, Heather LC, Clarke K, Radda GK, Tyler DJ. In vivo assessment of pyruvate dehydrogenase flux in the heart using hyperpolarized carbon-13 magnetic resonance. Proc Natl Acad Sci U S A 2008;105(33):12051-12056.

43. Wiesinger F, Weidl E, Menzel MI, Janich MA, Khegai O, Glaser SJ, Haase A, Schwaiger M, Schulte RF. IDEAL spiral CSI for dynamic metabolic MR imaging of hyperpolarized [1-13C]pyruvate. Magn Reson Med 2012;68(1):8-16.

44. Reeder SB, Brittain JH, Grist TM, Yen YF. Least-squares chemical shift separation for (13)C metabolic imaging. J Magn Reson Imaging 2007;26(4):1145-1152.

Chapter 2

2 Computationally Rapid Method of Estimating Signal-To-Noise Ratio for Phased Array Image Reconstructions[1]

2.1 Introduction

Parallel magnetic resonance image reconstruction exhibits spatially dependent noise amplification that can make accurate signal-to-noise (SNR) calculations difficult. The spatial dependence of noise properties in the reconstructed image prevents the use of the conventional region of interest (ROI) calculations of SNR (where the noise is measured using an ROI in a region containing no signal).

Parallel imaging reconstructions like SMASH (1), SENSE (2) and GRAPPA (3), which use signals simultaneously acquired from multiple receive coils, rely on the spatial information contained in each coil's unique sensitivity to partially replace conventional phase encoding. The penalty for replacing a portion of the phase encoding is a loss in SNR from two effects: a decrease in SNR by a factor of the square root of the acceleration factor due to reduced signal averaging and an additional penalty caused by spatially dependent noise amplification (the "g-factor")(2).

A number of alternative methods of measuring SNR for phased array image reconstructions have been proposed, including direct SNR calculation (4), Monte Carlo based "pseudo multiple replica" SNR estimation (5) and estimation of SNR from multiple acquisitions (6). However, each of these methods has limitations, as we will outline below.

Direct SNR calculation (4) can be computationally rapid (ie. calculation does not take substantially longer than the image reconstruction) but is not applicable to sampling

---

[1] A version of Chapter 2 has been published: Wiens CN, Kisch SJ, Willig-Onwuachi JD, McKenzie CA. Computationally Rapid Method of Estimating SNR for phased array image reconstructions. Magnetic Resonance In Medicine 2011;66:1192-1197.

patterns and/or reconstruction techniques in which an analytic g-factor map is not computationally feasible. A common case in which direct SNR calculation is not computationally feasible due to the size of the matrix that needs to be inverted is 2D-accelerated generalized SENSE reconstructions with variable density sampling (7).

The pseudo multiple replica method is more broadly applicable than the direct SNR calculation method but can require lengthy reconstruction times. It can be used with any linear image reconstruction, including SENSE and "complex-GRAPPA" with any arbitrary k-space trajectories pattern. The limitations of the pseudo multiple replica method, however, lie in its lengthy computation time, as it requires multiple reconstructions (typically ~128) of the raw dataset with random pseudo-noise added to ensure a precise estimate of SNR.

SNR estimates from multiple image acquisitions (6,8,9) are computationally rapid, but they require substantial additional image acquisition time and are highly susceptible to errors resulting from variations between acquisitions (e.g. motion, radiofrequency instability, etc.). In one multiple acquisition method proposed in the NEMA standard, an image is acquired twice and the difference between the two images is used to determine the noise (6). Motion, even on a sub-pixel level, will introduce error in the SNR estimate, making this method difficult for *in vivo* imaging.

To avoid the limitations of the aforementioned methods of determining SNR in parallel MR reconstructions, we propose a new SNR estimation approach that is a hybrid of the NEMA two-acquisition method and the pseudo multiple replica method. In the proposed method an estimate of the image noise is determined using noise variations in space (similar to the NEMA technique) between a reconstruction of the acquired data and a separate reconstruction of that same data with pseudo-noise added (similar to the pseudo multiple replica technique). This method can be used to produce accurate SNR maps for linear image reconstructions with arbitrary k-space sampling patterns. This method is computationally rapid because it only requires two reconstructions and avoids the complications of multiple image acquisitions by using the same data for both of the image reconstructions. In this chapter, we will refer to the proposed technique as the generalized pseudo replica method, or simply the generalized method.

2.2 Theory

The noise in magnetic resonance signals is characterized by the standard deviation of noise variations in time and/or space. Multiple-acquisition methods of determining SNR such as the actual replica method (8,9) rely on noise variations in time and the assumption that the repeated acquisitions of data differ only in noise content. The pseudo replica method (5) works on the same assumption, but introduces the idea that synthetic noise that has been correctly scaled and correlated between elements can be repeatedly added to a single dataset to produce the same noise statistics on a pixel-by-pixel basis by analyzing a stack of reconstructed pseudo images. Note that because the added noise is correlated and scaled appropriately and has passed through the same signal reconstruction algorithm, each pseudo-image has the same spatial noise amplification as the original image without synthetic noise.

A noise map can be calculated by taking the standard deviation through a stack of replicas (actual or synthetic) for each pixel

$$Noise(i,j,k) = \sqrt{\frac{\sum_{m=1}^{n_{replicas}} (V(i,j,k,m) - V_{ave}(i,j,k))^2}{n_{replicas} - 1}} , \qquad 2.1$$

where V is the real (or equivalently imaginary) component of pseudo-image m at spatial position (i,j,k), V_{ave} is the average value through the stack of replicas of the real (or imaginary) component,

$$V_{ave}(i,j,k) = \frac{\sum_{m=1}^{n_{replicas}} V(i,j,k,m)}{n_{replicas}} , \qquad 2.2$$

and n_{replicas} is the number of replicas. This stack of replicas can be produced using pseudo-images, actual replicas, or a combination of both. This method requires at least two replicas with the cost of fewer replicas being a decrease in precision.

Traditionally, however, SNR has been measured by examining spatial noise variations (i.e. with fixed ROIs). If we include nearby pixels with a sliding window average method to obtain additional noise statistics, Eqn. 2.1 can be further generalized. Here image noise is calculated using a 4D moving standard deviation calculation:

$$Noise(s,q,r)=\sqrt{\frac{\sum_{i=s-n_i}^{s+n_i}\sum_{j=q-n_j}^{q=n_j}\sum_{k=r-n_k}^{r+n_k}\sum_{m=1}^{n_{replicas}}(V(i,j,k,m)-\bar{V}(s,q,r))^2}{n_{replicas}(2n_i+1)(2n_j+1)(2n_k+1)-1}}, \qquad 2.3$$

where we now use nearby pixels of a sliding 3D volume of interest (VOI) with dimensions $(2n_i+1)$ x $(2n_j+1)$ x $(2n_k+1)$ to obtain additional noise statistics. In other words, for each pixel, noise statistics are determined by examining the set of pixels in the local VOI for all replicas. Thus $\bar{V}$ for each pixel has been computed as the average of that same set of pixels—not just over the replica dimension.

$$\bar{V}(s,q,r)=\frac{\sum_{\alpha=s-n_i}^{s+n_i}\sum_{\beta=q-n_j}^{q+n_j}\sum_{\gamma=r-n_k}^{r+n_k}\sum_{m=1}^{n_{replicas}}V(\alpha,\beta,\gamma,m)}{n_{replicas}(2n_i+1)(2n_j+1)(2n_k+1)}. \qquad 2.4$$

Problems arise with Eqn. 2.3 when the signal varies across the VOI and results in biased noise calculations. To remove this problem, the noise is calculated on noise-only images rather than the pseudo-images as done in the method describe in the NEMA standard (6). Noise-only images are produced by subtracting the pseudo-images from the original image with no synthetic noise added and will subsequently be denoted N. Equation 2.3 can be now be written in terms of noise-only images

$$Noise(s,q,r)=\sqrt{\frac{\sum_{i=s-n_i}^{s+n_i}\sum_{j=q-n_j}^{q=n_j}\sum_{k=r-n_k}^{r+n_k}\sum_{m=1}^{n_{replicas}}(N(i,j,k,m)-\overline{N}(s,q,r))^2}{n_{replicas}(2n_i+1)(2n_j+1)(2n_k+1)-1}} \qquad 2.5$$

where

$$\overline{N}(s,q,r)=\frac{\sum_{\alpha=s-n_i}^{s+n_i}\sum_{\beta=q-n_j}^{q+n_j}\sum_{\gamma=r-n_k}^{r+n_k}\sum_{m=1}^{n_{replicas}}N(\alpha,\beta,\gamma,m)}{n_{replicas}(2n_i+1)(2n_j+1)(2n_k+1)}. \qquad 2.6$$

The use of nearby pixels allows the use of fewer replicas without the loss in precision. The sliding volume of interest calculation allows for the noise to vary across the image, but the use of nearby pixels for noise calculation causes some spatial smoothing of the noise map. Large g-factor spikes will be measured multiple times by nearby pixels, effectively blurring the spikes over the volume used to calculate the noise. It is desirable to have a box size that is large enough to provide reasonable statistics for noise calculation but small enough so that there is minimal variation in the g-factor over its volume. The number of replicas and the sliding volume of interest box size can be adjusted in combination to achieve the desired/acceptable level of noise accuracy, spatial smoothing, and computation time.

In the limiting case of only one replica ($n_{replicas} = 1$) noise is measured spatially and Eqn. 2.5 simplifies to a moving VOI standard deviation calculation:

$$Noise(s,q,r)=\sqrt{\frac{\sum_{i=s-n_i}^{s+n_i}\sum_{j=q-n_j}^{q+n_j}\sum_{k=r-n_k}^{r+n_k}\left(N(i,j,k)-\overline{N}\right)^2}{(2n_i+1)(2n_j+1)(2n_k+1)-1}}. \qquad 2.7$$

The generalized pseudo replica method of calculating an SNR map involves calculating a noise map using Eqn. 2.5 then dividing the magnitude of the original image by this noise map on a pixel-by-pixel basis.

2.3 Methods

2.3.1 Phantom Experiments

The generalized pseudo replica method of SNR estimation was first validated for 1D acceleration on a spherical phantom by comparison with the pseudo-replica and analytic direct SNR methods. A fully gradient encoded 3D spoiled gradient recalled echo (SGPR) dataset was acquired of a spherical phantom using an eight channel head coil at 3T (MR 750, GE Healthcare, Waukesha, WI, USA). The *k*-space data were decimated to obtain sampling patterns with net acceleration factors of 1.8 (outer reduction factor (ORF) of 2 and 32x32 fully sampled center lines) and 2.9 (outer acceleration factor of 4 and 32x32 fully sampled center lines). Imaging parameters were as follows: TE=1.7 ms, TR=5.0 ms, matrix size=256x256x64, field of view (FOV) 220 mm, slice thickness=3.5 mm, flip angle=15°, and bandwidth (BW)= +/- 143 kHz.

2.3.2 *in vivo* Experiments

The generalized pseudo replica method was also compared to the standard pseudo multiple replica method for a two dimensional, variable density undersampling pattern *in vivo*. After obtaining ethics approval from the University of Western Ontario's Research Ethics Board and informed consent from a healthy volunteer, one low resolution, fully encoded data set and two high resolution, undersampled 3D SGPR datasets of the liver were acquired using a 32 channel torso coil at 3T (MR 750, GE Healthcare, Waukesha, WI, USA). The fully sampled dataset was taken at a lower resolution than the undersampled datasets because image acquisition in the abdomen must be performed in a single breath-hold (~20s) to avoid breathing-induced motion artefacts.

Imaging parameters for the low resolution, fully sampled dataset were: TE=1.4 ms, TR=6.6 ms, matrix size=144x96x32, FOV 400x300 mm, slice thickness=8.5 mm, flip angle=10°, and BW= ±143 kHz. Imaging parameters for the first high resolution, undersampled dataset were: TE=2.2 ms, TR=10.7 ms, matrix size=224x120x48, FOV 400x300 mm, slice thickness=5.5 mm, flip angle=10°, Acceleration Factor=3.2 (outer reduction factor of 2x2 and 32x32 fully sampled center lines), and BW= ±143 kHz. Imaging parameters for the second high resolution, undersampled dataset were the same as the first except Acceleration Factor=5.5 (outer acceleration factor of 3x3 and 24x24 fully sampled center lines).

2.3.3 Noise Covariance Measurement

For both phantom and *in vivo* acquisitions, a noise-only scan was acquired by setting the amplitude of the radiofrequency pulse to zero. For noise scans, 65536 data points were collected using the same bandwidths and amplifier gains as the corresponding images and were used to calculate the noise covariance matrix (10) for correct scaling and correlation of the pseudo-noise (5,11)

2.3.4 Image reconstruction and noise analysis

For the 1D-accelerated phantom data, direct matrix-inverse generalized SENSE was used for image reconstruction. SNR maps were calculated using direct SNR (11), pseudo multiple replica (5) with 128 replicas, and generalized pseudo replica methods (as described above in the Theory section) with a single replica. Normalized difference maps were also calculated to compare results from the latter two techniques to the first. For phantom data, the following formula was used

$$NormalizedDifference(i,j) = \frac{A(i,j) - B(i,j)}{B(i,j)} \qquad 2.8$$

where A(i,j) is the SNR map from either the pseudo multiple replica technique or the generalized method and B(i,j) is the SNR map from the direct SNR technique.

These difference maps were also characterized numerically. The mean difference from the direct SNR method was calculated for both the pseudo multiple replica and generalized pseudo replica methods (simply the mean of the difference maps described above). Confidence intervals were also tabulated for both methods. The range indicated by the 99% confidence interval is meant to represent the range in which the central 99% of the pixel values for a given difference map fall. The mean difference and confidence intervals were calculated for each acceleration factor presented.

For the 2D-acclerated *in vivo* data, conjugate gradient generalized SENSE was used for image reconstruction. SNR maps were calculated using the pseudo multiple replica method with 128 replicas and using the generalized method with a single replica. The direct SNR method was not calculated in this case, since direct SNR calculation is not computationally feasible for non-uniform, 2D-accelerated acquisitions. Normalized difference maps, calculated from Eqn. 2.8, were used to compare results from these two techniques.

All image reconstructions, calculations, and analyses were performed using MATLAB (R2009-64bit, The MathWorks, Natick, MA, USA) on Mac Pro workstations (Apple Computer, Cupertino, CA, USA).

2.4 Results

Figure 2.1 shows SNR maps calculated using the direct SNR, pseudo multiple replica, and generalized pseudo replica methods for a slice of a spherical phantom reconstructed using a direct inverse generalized SENSE reconstruction. For each method, SNR maps are shown for a fully sampled dataset, an undersampled dataset with a net acceleration factor of 1.8, and an undersampled dataset with a net acceleration factor of 2.9.

Good agreement between all methods for low acceleration factors of 1 and 1.8 can be seen in Figure 2.1 and Table 2.1. At the relatively high acceleration factor of 2.9, the generalized pseudo replica method with a single replica deviated from the multiple pseudo replica and direct SNR calculations at the edge of the region with increased g-factor, as seen by the structure in the difference map on the lower right. This is expected, as the g-factor at these positions varies significantly even over the small volume used to calculate the noise, leading to a slightly biased SNR calculation. Despite this, the generalized method still gives an accurate measure of mean SNR (Table 2.1), with 99% confidence interval comparable to that of the multiple pseudo replica method. Also, the SNR maps for the generalized method depict the same major structures as the direct SNR and multiple pseudo replica methods.

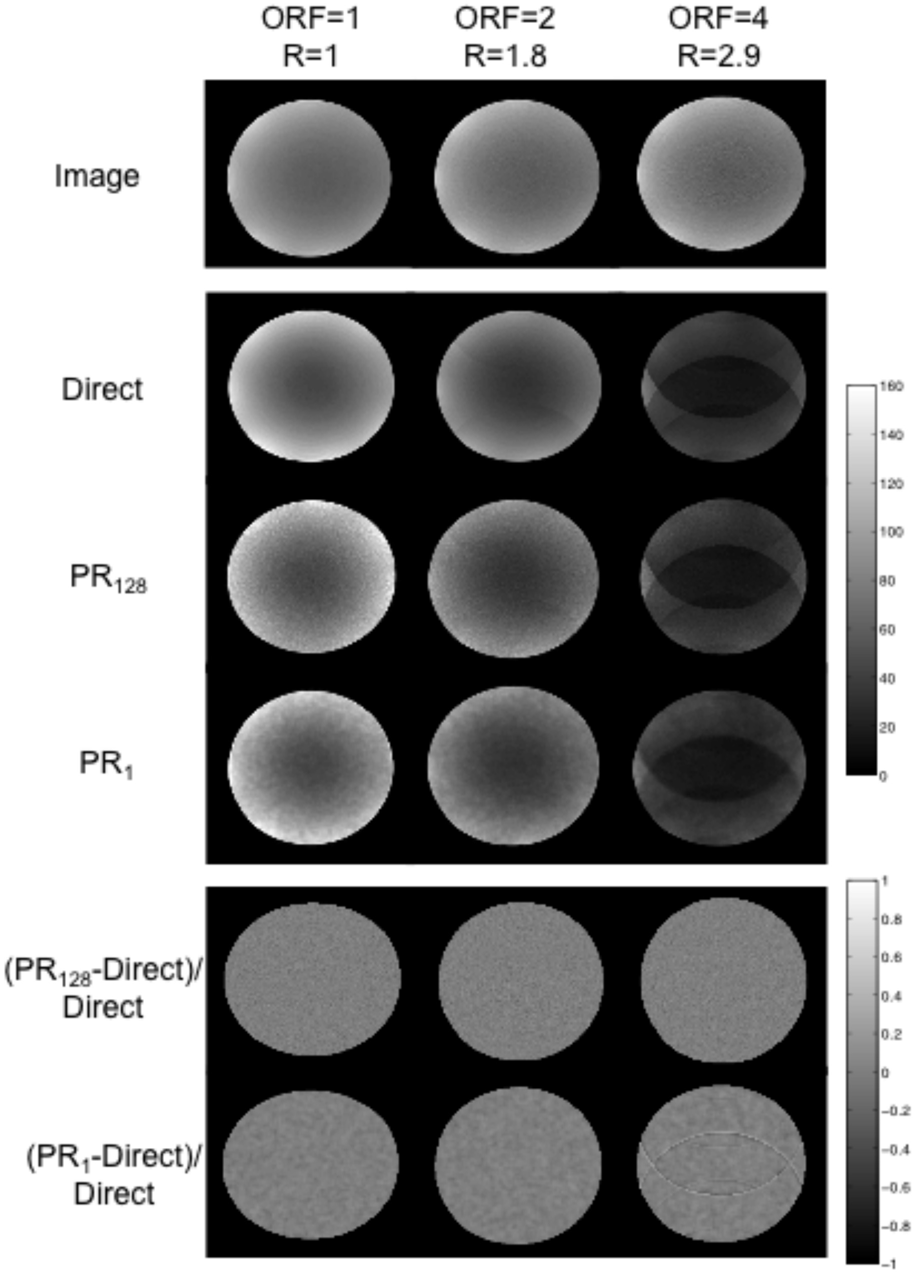

Figure 2.1 SNR maps using direct SNR calculation, pseudo multiple replica with 128 replicas (PR_{128}), and generalized pseudo replica with a single replica (PR_1) for generalized SENSE reconstructions with one dimensional net accelerations of 1, 1.8, and 2.9. Normalized differences between pseudo multiple replica and Direct SNR as well as generalized pseudo replica and Direct SNR are shown for each acceleration factor.

	PR$_{128}$		PR$_{1}$	
R	Mean	99% Confidence Interval	Mean	99% Confidence Interval
1	0.0060	[-0.128, 0.170]	-0.0044	[-0.098,0.078]
1.8	0.0062	[-0.128, 0.170]	-0.0054	[-0.098,0.082]
2.9	0.0061	[-0.127,0.167]	-0.0005	[-0.177, 0.207]

Table 2.1 Mean and 99% confidence interval of the normalized difference between multiple pseudo replica with 128 replicas (PR$_{128}$) and direct SNR methods and between generalized pseudo replica with a single replica (PR$_{1}$) and direct SNR methods for accelerations of 1, 1.8, and 2.9. These data correspond to the difference maps shown at the bottom of Figure 2.1.

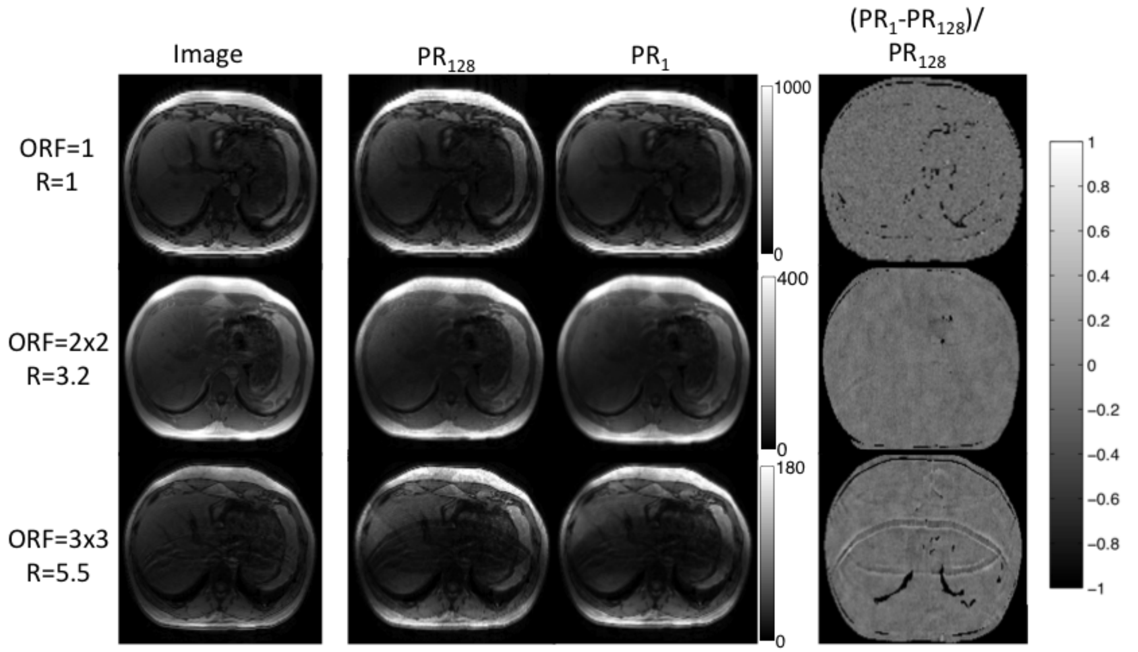

Figure 2.2 SNR maps of abdominal images at the level of the liver using the pseudo multiple replica with 128 replicas (PR$_{128}$) and generalized pseudo replica with a single replica (PR$_{1}$) for generalized SENSE reconstructions with acceleration factors of 1, 3.2, and 5.5. Resolution (and therefore SNR) of the un-accelerated and accelerated images are different as acquisition time in each case is limited to a single breath-hold.

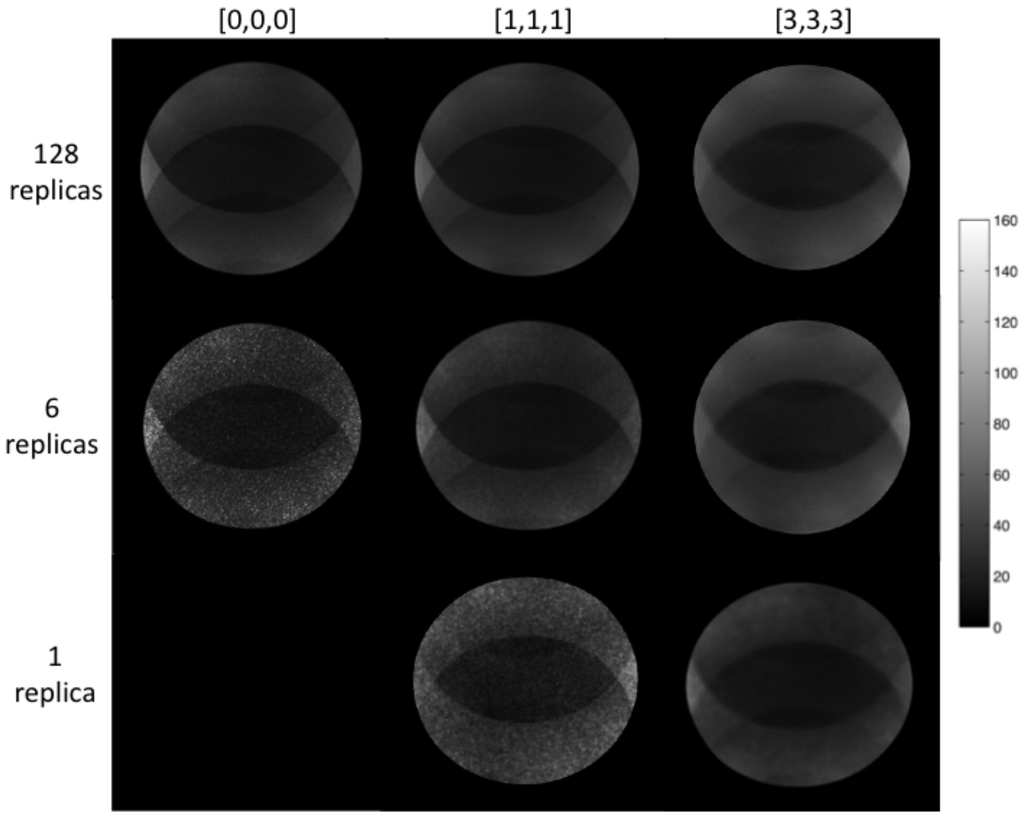

Figure 2.3 SNR maps with net acceleration factor of 2.9 showing the trade-off between spatial resolution and noise as the number of replicas and the volume used to calculate the noise [n_i,n_j,n_k] are changed. The single replica with box size of [0,0,0] is left blank because a SNR map cannot be calculated under those conditions.

Figure 2.2 shows SNR maps of an axial slice in the abdomen of a human volunteer (at the level of the liver) reconstructed with conjugate gradient generalized SENSE. SNR maps were calculated using the pseudo multiple replica and generalized pseudo replica methods with 128 and 1 replicas respectively. SNR maps are shown for a fully sampled dataset and for variable density undersampling patterns with net acceleration factors of 3.2 and 5.5. Normalized difference maps comparing the two techniques shown at the right of Figure 2.2 demonstrate that the generalized pseudo replica method and pseudo multiple replica SNR techniques give nearly equivalent SNR maps for both the fully sampled and undersampled datasets. Note that at the higher acceleration factor we again see the blurring effects of the generalized method with larger box size in locations where the g-factor varies significantly.

Figure 2.3 demonstrates how the generalized method can be adjusted to trade-off between spatial resolution and noise accuracy by varying the number of replicas and the moving VOI box size used to calculate the noise. The first column shows pseudo multiple replica SNR maps for 128, 6, and 1 replica. The second and third columns show results from the generalized method where both replicas and nearby pixels are used to calculate the noise statistics in varying amounts.

2.5 Discussion

As shown in Table 2.1,the 99% percent confidence intervals are actually lower for the generalized method with a single replica than the pseudo multiple replica method for phantom data with acceleration factors of 1 and 1.8. At low accelerations, the g-factor is relatively uniform over the volume of voxels used to measure the noise for a specific position, making the assumption that the noise is the same in each voxel a good approximation.

The generalized pseudo replica method allows for SNR calculations that are computationally rapid by reducing the number of required replicas, alleviating the major constraint to the use of the standard pseudo multiple replica technique. The vast majority of computation time for SNR calculation using pseudo-replica and the generalized pseudo replica methods is spent on image reconstructions. As such, the total computation time is roughly proportional to the number of replica images required to calculate the SNR. Since 128 pseudo-images were used for all but one of the SNR maps produced using the pseudo-replica method, the generalized pseudo replica method with a single replica can be up to approximately 128 times faster at calculating the SNR.

The tradeoff for the increased efficiency of the generalized pseudo replica method with fewer replicas is a loss of spatial resolution in the noise map and a slight bias at positions where g-factor varies drastically within the local averaging volume (i.e. for high accelerations). For many applications this loss of resolution is acceptable. Typically, the

SNR map is averaged over the region of interest to determine the mean SNR. In such a case the reduced spatial resolution in the noise map will not significantly effect the mean SNR, provided that the region of interest is larger than the box size used to calculate the SNR. Additionally, when necessary, the flexibility of the generalized pseudo replica method allows for buying back spatial resolution of SNR maps at the expense of a modest increase in replicas (and computation time). For example, the central image in Figure 2.3 shows very little blurring and only requires six replicas.

Other computationally rapid methods for generating SNR maps have been introduced recently. Steckner et al (12) proposed a new method in which the image acquisition is modified such that the matrix size and readout field of view are doubled. The even and odd readout data points are then used to make two normal images. The method works well for low duty cycle sequences. For high duty cycle sequences, the increase in data sampling time requires an increase in TE and/or TR thereby changing the SNR. In addition, this technique requires modification of the pulse sequence program, which is not a limitation of most other SNR measurement methods.

Li et al (13) proposed a method to calculate SNR for ARC parallel imaging. Noise only data are reconstructed using the weights from the actual image and the standard deviation of the resulting noise-only image in the region of interest is used to measure the noise. While this method and generalized pseudo-replica method both require noise-only data, the acquisition and use of the data is different. In the method proposed by Li et al, a complete image is acquired without any radiofrequency excitation in order to generate the noise-only data used to calculate the noise. In the generalized pseudo-replica method, the noise-only data is used to calculate the noise covariance matrix that is then used to create properly correlated and scaled pseudo noise. The noise-only data required to calculate the noise covariance matrix can be acquired in less than a second, whereas the method proposed by Li et al requires a complete image acquisition; therefore, Li’s technique requires almost double the acquisition time required for generalized pseudo-replica. In addition, Li’s method is not applicable to iterative processes such as conjugate gradient generalized SENSE, as noise-only data would not converge to the correct noise-only image.

In this article, the generalized pseudo replica method was applied to generalized SENSE reconstructions. However, the generalized pseudo replica method is applicable to any linear reconstruction technique. Linear reconstructions include but are not limited to most parallel imaging reconstructions, T1/T2 mapping (e.g. DESPOT (14)), fat/water separation (e.g. IDEAL (15)), and reconstructions of non-Cartesian trajectory data (e.g. GRAPPA operator (16)).

2.6 Conclusions

In this chapter a new approach to SNR for phased array reconstructions entitled the generalized pseudo replica approach was proposed and validated. This approach overcomes limitations of existing techniques: it is applicable to all linear parallel imaging reconstructions, does not require significant computation time, and does not rely on repeated image acquisitions. SNR comparisons can be used to assess coil performance and optimize parallel imaging sampling patterns for *in vivo* imaging.

2.7 References

1. Sodickson DK, Manning WJ. Simultaneous acquisition of spatial harmonics (SMASH): fast imaging with radiofrequency coil arrays. Magn Reson Med 1997;38(4):591-603.

2. Pruessmann KP, Weiger M, Scheidegger MB, Boesiger P. SENSE: sensitivity encoding for fast MRI. Magn Reson Med 1999;42(5):952-962.

3. Griswold MA, Jakob PM, Heidemann RM, Nittka M, Jellus V, Wang J, Kiefer B, Haase A. Generalized autocalibrating partially parallel acquisitions (GRAPPA). Magn Reson Med 2002;47(6):1202-1210.

4. Kellman P, McVeigh ER. Image reconstruction in SNR units: a general method for SNR measurement. Magn Reson Med 2005;54(6):1439-1447.

5. Robson PM, Grant AK, Madhuranthakam AJ, Lattanzi R, Sodickson DK, McKenzie CA. Comprehensive quantification of signal-to-noise ratio and g-factor for image-based and k-space-based parallel imaging reconstructions. Magn Reson Med 2008;60(4):895-907.

6. NEMA. Determination of Signal-to-Noise Ratio (SNR) in Diagnostic Magnetic Resonance Imaging. NEMA Standards Publication MS 1-2001 2001.

7. Pruessmann KP, Weiger M, Bornert P, Boesiger P. Advances in sensitivity encoding with arbitrary k-space trajectories. Magn Reson Med 2001;46(4):638-651.

8. Dietrich O, Raya JG, Reeder SB, Reiser MF, Schoenberg SO. Measurement of signal-to-noise ratios in MR images: influence of multichannel coils, parallel imaging, and reconstruction filters. J Magn Reson Imaging 2007;26(2):375-385.

9. Reeder SB, Wintersperger BJ, Dietrich O, Lanz T, Greiser A, Reiser MF, Glazer GM, Schoenberg SO. Practical approaches to the evaluation of signal-to-noise

ratio performance with parallel imaging: application with cardiac imaging and a 32-channel cardiac coil. Magn Reson Med 2005;54(3):748-754.

10. Roemer PB, Edelstein WA, Hayes CE, Souza SP, Mueller OM. The NMR phased array. Magn Reson Med 1990;16(2):192-225.

11. Kellman. Image Reconstruction in SNR Units: A General Method for SNR Measurement. Magnetic Resonance in Mecidine 2005;54:1439-1447.

12. Steckner MC, Liu B, Ying L. A new single acquisition, two-image difference method for determining MR image SNR. Med Phys 2009;36(2):662-671.

13. Li CQ, Chen W, Beatty PJ, Brau AC, Hargreaves BA, Busse RF, Gold GE. SNR Quantification with Phased-Array Coils and Parallel Imaging for 3D-FSE. In: Proceedings of 18th Annual Meeting of ISMRM, Stockholm, Sweden, 2010:552.

14. Deoni SC, Rutt BK, Peters TM. Rapid combined T1 and T2 mapping using gradient recalled acquisition in the steady state. Magn Reson Med 2003;49(3):515-526.

15. Reeder SB, Wen X, Yu H, Pineda AR, Gold GE, Markl M, Pelc NJ. Multicoil Dixon chemical species separation with an iterative least-squares estimation method. Magn Reson Med 2004;51(1):35-45.

16. Seiberlich N, Breuer FA, Blaimer M, Barkauskas K, Jakob PM, Griswold MA. Non-Cartesian data reconstruction using GRAPPA operator gridding (GROG). Magn Reson Med 2007;58(6):1257-1265.

Chapter 3

3 R_2^*-corrected Water-Fat Imaging using Compressed Sensing and Parallel Imaging[2]

3.1 Introduction

Use of water-fat imaging is wide spread, spanning a broad range of both anatomy and applications. Organs imaged include but are not limited to the liver, heart, calf, pancreas, and spine for applications such as quantitative grading and staging of non-alcoholic fatty liver disease (1), quantification of fat in bone marrow (2,3), measurement of total visceral adipose tissue (4), detection of brown fat (5), and detection of myocardial fat infiltration (6).

Chemical shift imaging has been demonstrated as a sensitive technique for measuring fat. In chemical shift imaging, multiple images are acquired at different echo times. Quantitative water-fat imaging can be achieved with chemical shift imaging if confounding factors such as T_1 bias (7,8), noise bias (7), accurate spectral modeling (8-10), and R_2^* correction (8,11,12) are accounted for. Unlike T_1 bias and accurate spectral modeling, R_2^* correction cannot be accounted for by choosing appropriate imaging parameters (low flip angle) and prior knowledge (position and relative amplitudes of fat peaks in fat spectrum). R_2^* correction is made by modifying the signal model to account for the signal decay due to R_2^*. This addition to the model increases the number of free parameters and thus the required amount of data for accurate and reliable model fitting. Typically six-echo acquisitions have been used to provide a good balance between acquisition time and accurate R_2^* estimation.

---

[2] A version of Chapter 3 has been accepted for publication: Wiens CN, McCurdy CM, Willig-Onwuachi JD, McKenzie CA. R2*-corrected Water-Fat Imaging using Compressed Sensing and Parallel Imaging. Magnetic Resonance In Medicine 2013. doi: 10.1002/mrm.24699

The acquisition of multiple 3D images is time consuming. This places considerable limitations on the resolution and anatomical coverage achievable, particularly in abdominal applications where breath-hold restrictions limit scan times to a single breath-hold (approximately 20s) in order to minimize motion artefacts. In order to achieve desired spatial resolution and coverage in abdominal imaging, image acceleration techniques must be utilized.

The role of image acceleration has been filled by parallel imaging techniques (13-15); however, reduced signal-to-noise ratio (SNR) presents a challenge—particularly for SNR limited applications like the low flip angle sequences used to prevent T_1 bias in water-fat imaging. SNR is lost in parallel MRI via two mechanisms: reduced signal averaging (SNR is decreased by the square root of the reduction factor in imaging time) and spatially dependent noise amplification during the reconstruction process (described by the g-factor). This SNR limitation constrains the degree to which parallel imaging can be used to accelerate water-fat imaging.

Compressed sensing has been shown to be an alternative and complimentary approach to parallel imaging for image acceleration (16,17). Previous work (18,19) has examined the use of compressed sensing techniques that exploit sub-sampling in *k*-space and the chemical shift dimension for accelerating water-fat imaging using a 3-echo acquisition without R_2^* correction. Unlike most water-fat separation techniques, which separate water and fat on a voxel-by-voxel basis, these techniques require that each voxel in an image be estimated simultaneously to allow sparsity of the water and fat images to be enforced.

Large coil arrays have significant advantages: improved SNR and higher achievable parallel imaging acceleration factors. However, these large multi-coil datasets present challenges in terms of memory constraints and reconstruction times for parallel imaging and compressed sensing. Coil compression techniques (20-22) have been developed to combine these large multi-coil datasets into fewer virtual coils, thereby improving reconstruction times with minimal loss of image quality.

In this work an integrated compressed sensing, parallel imaging, and water-fat separation technique is described. This technique includes R_2^* estimation, making it applicable to quantitative water-fat imaging. Coil compression is used to reduce image reconstruction times. This technique is demonstrated using retrospective and prospective undersampling of 3D liver, abdominal cavity, and calf datasets.

3.2 Theory

3.2.1 Signal Model

Chemical shift imaging separates signal from water and signal from fat by using multiple source images, taken at N different echo times t_n. At any position p (ranging from 1:P), the image domain signal at echo time n (I_n^p) can be described as a combination of fat, ρ_f^p, and water, ρ_w^p (9)

$$I_n^p = \left(\rho_w^p + \rho_f^p \cdot \sum_j \alpha_j \cdot e^{i2\pi f_j t_n} \right) e^{i2\pi\psi^p t_n}, \qquad 3.1$$

where α_j and f_j are the relative amplitudes and chemical shifts, respectively, of the jth spectral peak of fat and where the complex field map ψ^p arises from the R_2^* value and deviation from the central magnetic field, ψ'^p at that position (9)

$$\psi^p = \psi'^p + i\frac{R_2^{*p}}{2\pi}. \qquad 3.2$$

Using fixed and known characteristics of the spectral peaks of fat (α_j and f_j) (9,10), the signal measured at any position can now be described by four unknowns: the fat signal (ρ_f), the water signal (ρ_w), the R_2^* value, and the field deviation value (ψ').

The image domain signal can be mapped to multi-coil k-space in the standard way using a modified Fourier transform accounting for coil sensitivities. The k-space signal for a given coil (indexed by l) can be written as an integral of the image-domain signal, I_n^p (Eqn. 3.1), against the coil sensitivity, C_l, and the sinusoidal gradient phase modulations. This relationship can be written in the form of a matrix equation:

$$\mathbf{S}_n = E\Lambda_n(\boldsymbol{\rho}_w + \boldsymbol{\rho}_f d_n) , \qquad 3.3$$

where $\mathbf{S}_n$ is a vector of the signal values in the nth echo, with elements $S_q \equiv S_{nl}(k)$, and where every combination of *k*-space index, k, and coil index, *l*, maps onto a unique row index, *q*. Here $\boldsymbol{\rho}_w$ and $\boldsymbol{\rho}_f$ are vectors of the water and fat image domain signals, respectively, with elements ρ_w and ρ_f. Also, $d_n \equiv \sum_j \alpha_j \exp(i2\pi f_j t_n)$ and Λ_n is a PxP diagonal matrix with $\exp(i2\pi\psi^p t_n)$ at the *p*th diagonal. The encoding matrix, E, contains coil sensitivity and gradient modulations (Fourier transform modulations) for each location r_p, with elements $E_{qp} \equiv C_l(r_p)\exp(-i2\pi k r_p)$, where *q* again indexes combinations of *l* and k.

3.2.2 Sampling

Use of coil sensitivities (not always explicitly calculated) to perform some fraction of spatial encoding of an image is the common characteristic of parallel imaging reconstructions. Typically, uniform undersampling patterns in *k*-space, which lead to coherent point spread functions, are used to accelerate imaging. These uniform patterns minimize the distance of adjacent sample points in *k*-space. Large gaps between sampled points lead to high g-factors and sub-optimal parallel imaging reconstructions.

An incoherent point spread function is a necessary requirement for any compressed sensing reconstruction. Random undersampling patterns can provide this high degree of incoherence, but often result in large gaps between sampled points. Poisson disk undersampling (23) has been proposed as an alternative for combined parallel imaging compressed sensing reconstructions (24), including in water-fat compressed sensing reconstructions (18,19,25). This sampling pattern has two important properties: an incoherent point spread function and no large gaps between adjacent sampled points. Additional temporal incoherence can be added to water-fat image reconstruction by sampling each echo image with a different Poisson disk sampling pattern (18,26). It is expected that increasing the number of echoes will increase the importance of temporal incoherence.

3.2.3 Water-Fat Images

The objective of the reconstruction is to find estimates of water, fat, R_2^*, and field maps which when applied to the signal model are consistent with the acquired *k*-space. Using the constraints imposed by compressed sensing and parallel imaging, these estimates can be made from an undersampled dataset.

To ensure that the noise in the set of coils was uncorrelated, the acquired *k*-space data were transformed to a basis with uncorrelated noise using Cholesky decomposition of the noise correlation matrix (15). For most coil arrays, the noise is approximately uncorrelated and this step can be ignored with minimal loss of performance. From this point on, any mention of acquired *k*-space refers to *k*-space with decorrelated noise.

In the case where the field map and R_2^* are known (Λ_n matrix is known), the compressed sensing – parallel imaging problem can be posed as a convex optimization problem(25)

$$\underset{\boldsymbol{\rho}_w,\boldsymbol{\rho}_f}{\operatorname{argmin}} \sum_{n=1}^{N} \| U_n \mathbf{S}_n - \boldsymbol{\kappa}(t_n) \|_2^2 + \lambda_w \| \Phi_w \boldsymbol{\rho}_w \|_1 + \lambda_f \| \Phi_f \boldsymbol{\rho}_f \|_1 , \qquad 3.4$$

where U_n is the sampling transform, which picks off the value of the signal S_n for acquired *k*-space locations. Here, the first term enforces consistency between the water and fat images and our acquired undersampled, *k*-space data at echo time t_n (denoted $\boldsymbol{\kappa}(t_n)$). The second and third terms promote sparsity of both the water and fat images in their sparsity transform domain (with transform operators Φ_f and Φ_w, respectively). The weighting factors (λ_f, λ_w) scale the importance of sparsity constraints relative to data consistency. Eqn. 3.4 can be solved iteratively, in our case using a non-linear conjugate-gradient algorithm (16).

3.2.4 Updating Field Map and R_2^* Terms

If the field map and R_2^* terms are not explicitly known, they too can be found through an optimization process, though the problem becomes non-convex. Our reconstruction uses an approach similar to the Gauss-Newton method (18) to linearize the problem and solve its linearized version for the update terms. In this form, ΔR_2^* and $\Delta\psi'$ are now unknowns and must be iteratively determined:

$$\begin{aligned}&\underset{\Delta\rho_w,\Delta\rho_f,\Delta\psi,\Delta R_2^*}{\arg\min}\sum_{n=1}^{N}\|\boldsymbol{\delta}_{\mathbf{n}}+\mathrm{U}_n\mathrm{E}\Lambda_n\mathrm{B}\Delta\boldsymbol{\rho}\|_2^2+\lambda_w\|\Phi_w(\boldsymbol{\rho}_w+\Delta\boldsymbol{\rho}_w)\|_1+\lambda_f\|\Phi_f(\boldsymbol{\rho}_f+\Delta\boldsymbol{\rho}_f)\|_1+\\&+\lambda_{R2*}\|\Phi_{R2*}(\mathbf{R}_2^*+\Delta\mathbf{R}_2^*)\|_1+\lambda_\psi\|\Phi_\psi(\boldsymbol{\psi}'+\Delta\boldsymbol{\psi}')\|_2^2\end{aligned} \qquad 3.5$$

where $\boldsymbol{\delta}_n$ is the residual of current estimates mapped to *k*-space

$$\boldsymbol{\delta}_{\mathrm{n}}=\mathrm{U}_n\mathbf{S}_n-\boldsymbol{\kappa}(t_n) \qquad 3.6$$

$\Delta\rho$ is the concatenation of the water, fat, and complex field map update terms,

$\Delta\rho=[\Delta\rho_w^1,\ldots,\Delta\rho_w^P,\Delta\rho_f^1,\ldots,\Delta\rho_f^P,\Delta\psi^1,\ldots,\Delta\psi^P]^{\mathrm{T}}$ and B is a *P*x3*P* matrix consisting of three concatenated *P*x*P* diagonal matrices: the identity matrix, the identity matrix scaled by d_n, and $2\pi i t_n \mathrm{diag}(\rho_w^p+\mathrm{d}_n\rho_f^p)$. The first term of Eqn. 3.5 enforces consistency between the signal model and the acquired data, terms two through four promote sparsity of the estimates in specific transform domains (with transform operators Φ_w, Φ_f, Φ_{R2*}), and the fifth term enforces smoothness on the field map.

3.2.5 Initialization

Good initialization is critical to a successful reconstruction. Convergence of non-linear, non-convex optimization problems is not guaranteed for gradient based methods. Good initialization helps the reconstruction converge and reduces the number of iterations required to converge. Initialization was obtained by running a combined parallel imaging-compressed sensing reconstruction on each of the echo images, followed by an R_2^* corrected water-fat separation technique.

3.2.6 Summary of Technique

The proposed procedure is summarized as follows:

1. Initialize the field map and R_2^* estimates by performing a compressed sensing-parallel imaging reconstruction followed a R_2^* corrected water-fat separation technique.

2. Solve the linearized problem (Eqn. 3.5) for the water, fat, field map, and R_2^* update images. Continue updating until the maximum field map and R_2^* update terms are small.

3. Find the final water and fat images by solving the convex problem posed by Eqn. 3.4.

3.3 Methods

All images were acquired at 3T (MR 750, GE Healthcare, Waukesha, WI, USA) using a customized IDEAL-SPGR sequence. Figure 3.1 shows our modified six-echo IDEAL-SPGR pulse sequence capable of sampling each echo differently. Small y and z gradients were applied during the readout rewinder to alter each echo's sampling pattern.

The following method was used to minimize size of the y and z gradients applied during the fly-back. For each echo within an echo train length (ETL), sampling patterns broken up smaller patterns (i.e. k-space is broken up into 8 or 10 pieces). These smaller sampling patterns where then zigzagged through to obtain sets of k-space points to sample within an ETL. The size of these smaller patterns were adjusted to ensure that one echo within an ETL didn't deviate significantly from the others. Once k-space sampling pattern sets were obtained for each smaller sampling pattern, the maximum gradient size was calculated. This process was repeated with new sampling patterns until the maximum gradient size fell within an acceptable level of tolerance. This tolerance level is dependent on the resolution of image.

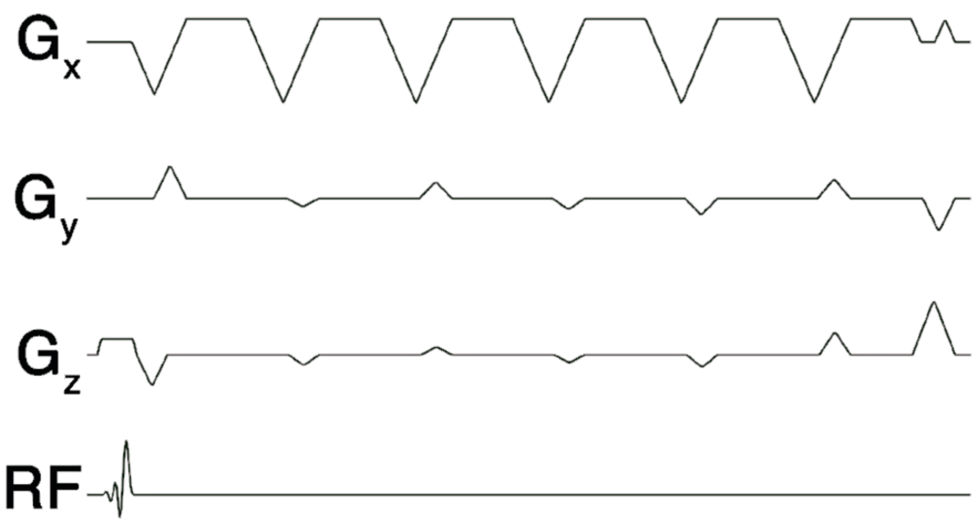

Figure 3.1 Sample TR of the fat-water pulse sequence. Small y and z gradients are applied during the frequency rewinder, allowing each echo to have a different *k*-space sampling pattern, thereby improving temporal incoherence. These small gradients are not shown to scale.

Ethics approval from the University of Western Ontario's Research Ethics Board and informed consent from healthy volunteers were obtained. For each scan, a noise-only scan was acquired to allow measurement of the noise covariance. Imaging parameters for each dataset are displayed in Table 3.1.

3.3.1 Undersampling Experiments

Fully gradient encoded datasets of the liver were acquired using an 8 coil (8Ch HDMR2 Torso Array coil (RX), GEHC Coils, Aurora, Ohio) and a 32 coil array (3.0T 32Ch Cardiac coil, Invivo, Gainesville, Florida, USA). Experiments were performed to compare the proposed method to a fully sampled reference (Figure 3.2) as well as to acceleration with parallel imaging alone (Figure 3.3). The datasets were retrospectively undersampled to the desired sampling pattern: Our proposed method uses Poisson disk sampling (23) with different patterns for each echo. Uniform undersampling patterns with the same pattern for each echo for parallel imaging alone were used. In both cases

	Figure 2	Figure 3	Figure 4	Figure 5	Figure 6	Figure 7
Number of Coils	8	32	8	8	32	32
Location	Liver	Liver	Calf	Knee	Abdomen	Abdomen
TR (ms)	7.1	7.1	7.2	10.1	6.3	7.1
TE_1 (ms)	1.0	1.0	1.4	2.1	0.9	1.0
ΔTE (ms)	0.8	0.8	0.7	1.0	0.6	0.8
In-Plane Matrix Size	160x112	160x112	128x128	224x224	148x104	192x144
Slices	48	48	64	88	120	32
ETL	3	3	2	2	3	3
Slice Thickness (mm)	4.5	4.5	3.0	1.2	3.6	6.0
FOV (cm)	40x28x22	40x28x22	16x16x19	20x20x11	42x29x43	40x30x19
Flip Angle (˚)	3	3	5	3	3	3
BW (kHz)	±143	±143	±83	±62	±125	±143
AF	3.2	1-5.0	4.0	3.8	7.0	3.1
Under-sampled	Retro	Retro	Retro	Both	Pro	Pro

Table 3.1 List of imaging parameters and acceleration for imaging experiments displayed in the Figures 3.2-3.7. Interleaved echo trains were used to reduce echo spacing (ΔTE). In addition to the parameters listed in this table, all data except for the knee datasets were acquired with axial scan planes and the frequency encode direction was from L→R. The knee datasets were acquired with sagittal scan planes and the frequency encode direction was from S→I.

the undersampling was performed outside a central fully sampled circular region (radius=12 lines). Water-fat separations for both the fully sampled and parallel imaging accelerated images were reconstructed using an R_2^* corrected IDEAL reconstruction (11). Parallel imaging reconstructions were performed using un-regularized CG-SENSE (15).

A fully gradient encoded dataset of a calf was acquired with an 8 coil array (HD T/R Knee Array, Invivo, Gainesville, Florida, USA). This dataset was retrospectively undersampled to produce two sets of undersampled data: one using the same Poisson disk sampling pattern for each echo and a second data set using a different Poisson disk sampling pattern for each echo (Figure 3.4). Both undersampled datasets were reconstructed using the proposed method. Fully sampled reference images were reconstructed using an R_2^* IDEAL reconstruction.

In order to examine the effect of the additional y and z gradients between each echo in an echo train, fully gradient encoded (no additional y and z gradients) and prospectively undersampled datasets (with additional y and z gradients) of the knee were acquired with the same 8 coil array used for calf imaging. The fully encoded dataset was retrospectively undersampled using the same sampling pattern (Poisson Disk, AF=3.8) as the prospectively undersampled dataset (Figure 3.5).

A prospectively undersampled dataset of the entire abdominal cavity (Figure 3.6) was acquired using a 32 coil array (Torso array, Neocoil, Pewaukee, WI, USA). These data were acquired with acceleration factor (AF) of 7.0 yielding an acquisition time of 19s. In addition, a prospectively undersampled dataset of the liver (Figure 3.7) was acquired using a 32 coil array (3.0T 32Ch Cardiac coil, Invivo, Gainesville, Florida, USA). An acceleration factor of 3.1 yielded an acquisition time of 21s.

3.3.2 Coil Sensitivity Estimation

For each scan the fully sampled center region of the first echo was used for coil sensitivity calculations using self-calibration (27).

3.3.3 Noise Covariance Measurement

For each scan, noise-only data were acquired as described by Kellman et al (28) in order to calculate the noise covariance for use in reconstruction of the undersampled data. For each noise scan, 50176 data points were acquired using the same bandwidths and amplifier gains as their corresponding data sets.

3.3.4 Reconstruction Implementation

The proposed method was implemented using MATLAB (R2011-64bit, The MathWorks, Natick, MA, USA) on Mac Pro workstations (Apple Computer, Cupertino, CA, USA). A six peak spectral model of fat (9,10) was used with the following frequencies and amplitudes: [485, 434, 332, 248, 50, -76] Hz and [0.087, 0.693, 0.128, 0.004, 0.039, 0.048]. A non-linear conjugate gradient reconstruction (16) was used to minimize the cost functions described in Eqn. 3.4 and Eqn. 3.5 and Wavelab was used for the wavelet transformation (29). The following sparsity transformations were used: both wavelet and finite differences for the water and fat images, 2nd order finite differences for the field map, and wavelet for the R_2^* map.

The choice of sparsity weighting factors is sensitive to scaling of both signal intensities and units of time and frequency. In this work the maximum signal intensities were normalized and units of 10^{-1}s (and 10^{1}Hz) were used for units of time (and frequency). These units allowed each of the estimates to have similar scaling. The sparsity weighting factors were set empirically such that a balance was achieved between enforcing both data consistency and sparsity: $[\lambda_w, \lambda_f, \lambda_{R2*}, \lambda_\psi]=[0.01, 0.01, 1e\text{-}4, 2e\text{-}4]$.

3.4 Results

Figure 3.2 shows water, fat, and R_2^* images for a fully sampled reference, as well as the proposed method with and without R_2^* estimation at an acceleration factor of 3.2. Arrows point to the bone marrow, a region where the R_2^* corrected images vary significantly from the case where R_2^* is neglected. The high R_2^* values in the bone marrow has caused poor estimates of water and fat in the reconstruction that neglects R_2^*. Regions of interest drawn over the liver of both the proposed and reference R_2^* images yielded mean ± standard deviation of (47±14)ms^{-1} and (48±14)ms^{-1}, respectively. Similarly, ROIs drawn over the spine yielded R_2^* values of (204±32) ms^{-1} and (196±23) ms^{-1}.

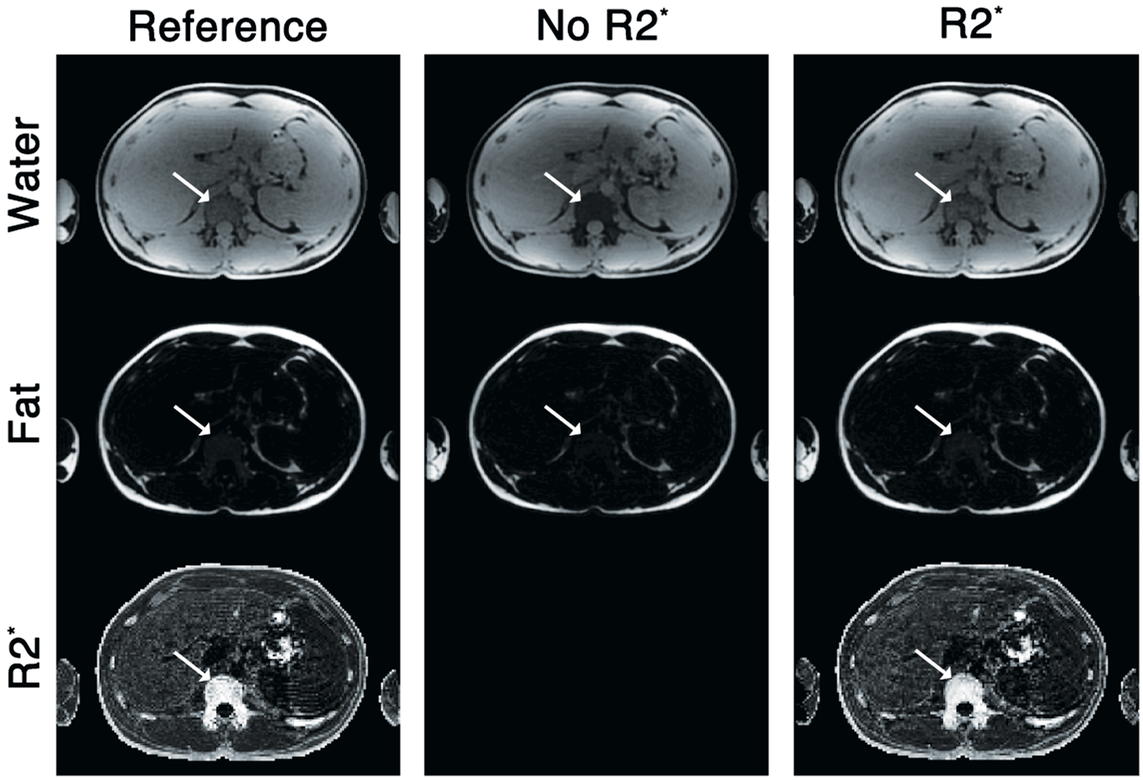

Figure 3.2 Water, Fat and R_2^* images of 3D abdominal data using the proposed method with and without R_2^* correction on data retrospectively undersampled at an acceleration factor (AF) of 3.2. Reference images (AF=1) were obtained using a fully sampled R_2^* corrected IDEAL reconstruction. Arrows point to the spine, a region with high R_2^* values, which result in inaccurate fat-water measurements when left uncorrected.

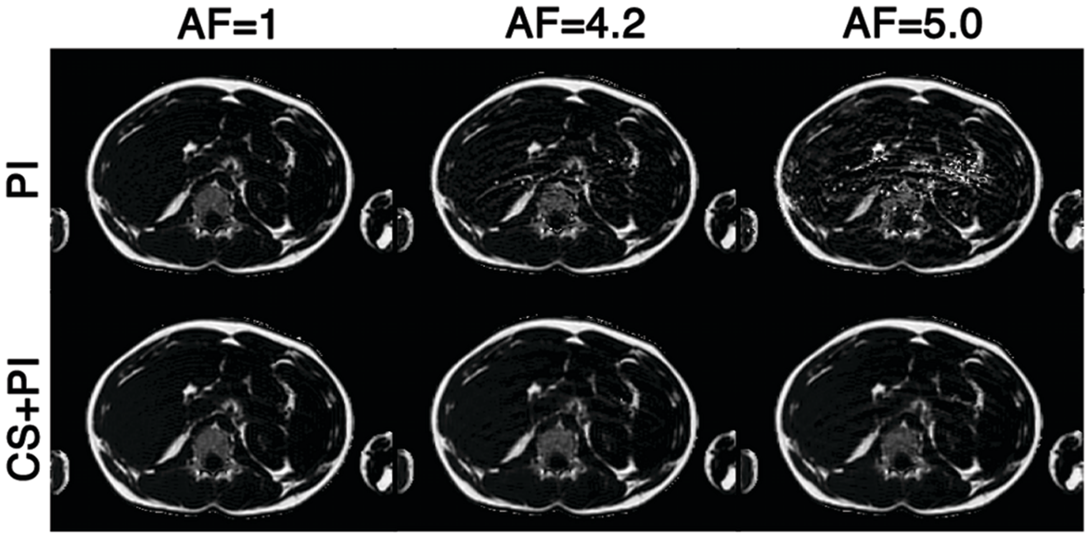

Figure 3.3 Fat fraction images of 3D abdominal data using the proposed method (bottom row) and sequential parallel imaging and water-fat separation (top row) at acceleration factors (AF) of 1, 4.2, and 5.0. Poisson disk (different pattern for each echo) and uniform (same pattern for each echo) undersampling patterns were used for the proposed method and parallel imaging respectively.

Figure 3.3 compares image reconstructions with the proposed method to reconstructions with sequential parallel imaging and R_2^*-corrected water-fat imaging at a variety of accelerations. As acceleration factors increase, image quality in the parallel imaging only case degrades due to increased residual aliasing and increased noise level caused by high g-factors. At acceleration factors of 5.0, the resulting fat fraction images exhibit drastically reduced SNR. This effect is a not as pronounced in the proposed method. Table 3.2 shows fat fractions determined from ROIs drawn in subcutaneous fat, spine, and liver of the datasets reconstructed in Figure 3.3. High g-factors caused bias in the spine and liver measurements for the parallel imaging only case.

	Reference	PI		PI+CS	
	AF=1	AF=4.2	AF=5.0	AF=4.2	AF=5.0
Subcutaneous Fat	88.9±3.1	88.6±2.9	88.6±2.9	88.6±3.0	88.6±2.9
Spine	26.3±3.6	25.8±7.1	27.3±11.4	26.8±3.6	26.4±4.1
Liver	2.7±1.5	5.1±3.9	10.8±11.5	3.0±1.0	3.2±1.4

Table 3.2 Fat fractions measured (mean±standard deviation) in the visceral fat, spine, and liver as a function of acceleration factor for both sequential parallel imaging and water-fat separation and the proposed method. Measurement were made on the dataset displayed in Figure 3.3.

Figure 3.4 shows the importance of temporal incoherence in an 8 channel calf dataset. In Figure 3.4b, data were undersampled using the same sampling pattern for each echo. In Figure 3.4c, a different sampling pattern was used for each echo. Net acceleration factors of 4.0 were used for both acquisitions. Figure 3.4c shows reduced residual aliasing and improved visibility of low contrast objects. One example of improved visibility of low contrast objects is circled in Figure 3.4.

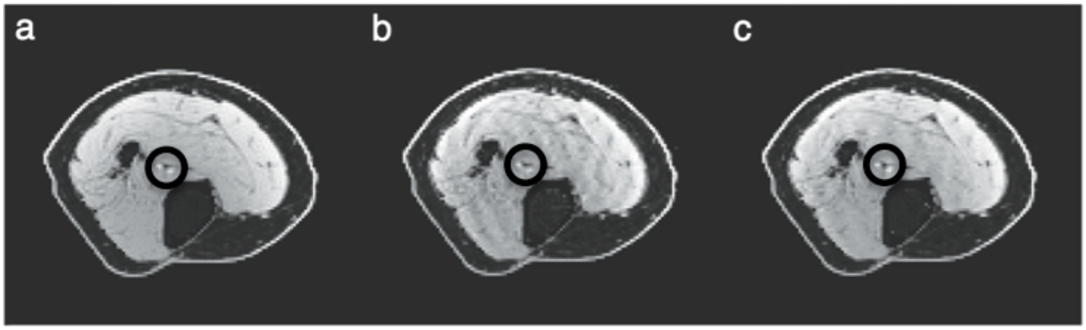

Figure 3.4 Water images of an 8 channel, 3D calf dataset. A reference image is shown for an axial slice (a) as well as accelerated images (b, c). In (b), the same sampling pattern is used for each echo. In (c), different sampling patterns are used for echo. The net acceleration factor was fixed for both acquisitions at 4.0. A low contrast object with improved visibility is circled.

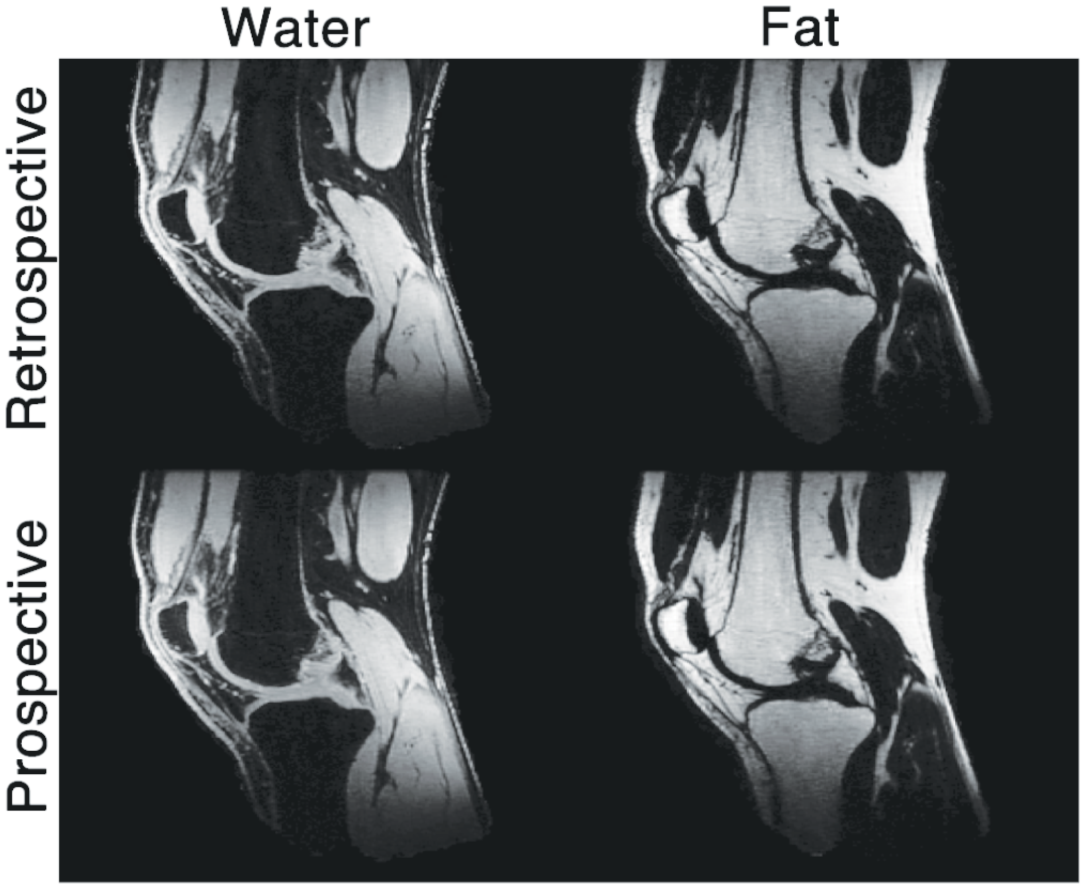

Figure 3.5 A comparison of retrospectively and prospectively decimated water and fat images. The fully sampled dataset was retrospectively decimated using the same sampling pattern (Poisson Disk, net acceleration factor = 3.8) as the prospectively decimated datasets. The equivalence of the two datasets shows that the additional y and z gradients are not affecting the quality of the water-fat separation.

Figure 3.5 compares retrospectively and prospectively undersampled datasets. Here, two acquisitions were acquired (fully sampled and prospectively undersampled). The fully sampled dataset was undersampled using the same sampling pattern as the prospectively undersampled. Comparable image quality is seen between the prospectively and retrospectively undersampled datasets, indicating that the additional y and z gradients between each echo in an echo train are not influencing reconstruction accuracy.

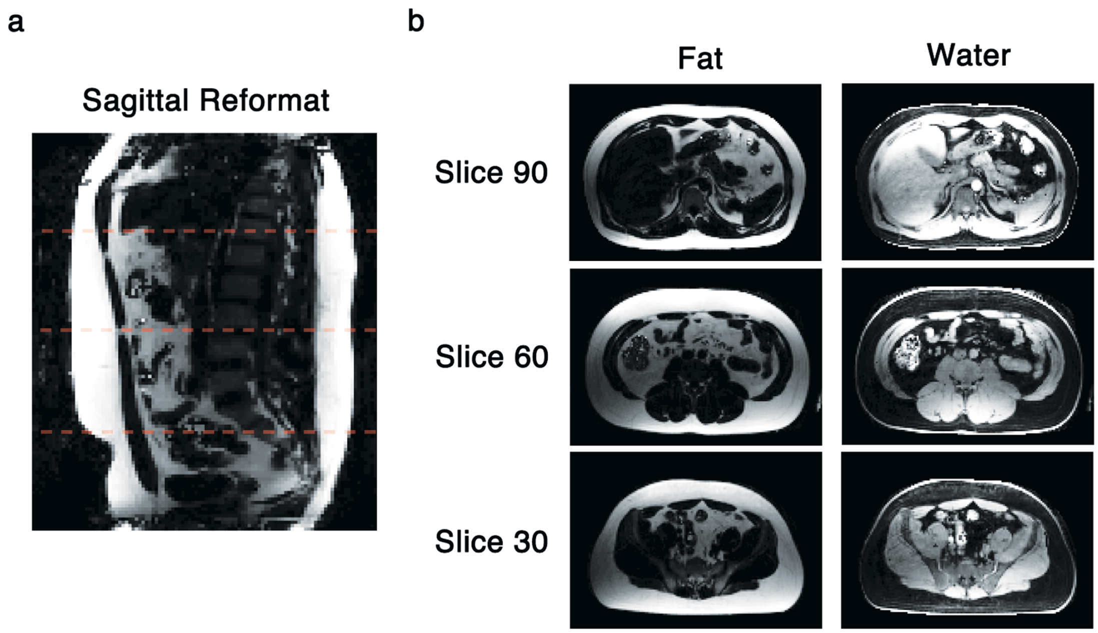

Figure 3.6 A prospectively undersampled dataset of entire abdominal cavity reconstructed with the proposed method. A sagittal reformat of the fat images is shown (a). Fat and water images are shown for slices 30, 60, and 90 (b). These three slices correspond to the three horizontal lines in (a). Net acceleration factor for this acquisition was 7.0.

Figure 3.6 shows images resulting from an acquisition with prospective undersampling. Here, the entire abdominal cavity was imaged in a 19s breath-hold using a net acceleration factor of 7.0. Figure 3.6a is a sagittal reformat of axially acquired images. Three horizontal lines are drawn on Figure 3.6a corresponding to the positions of slices 30, 60, and 90. Axial water and fat images are shown for each of the slices in Figure 3.5b.

Figure 3.7 displays the use of coil compression to help alleviate problems with memory constraints and lengthy reconstruction times. Here, a 32 channel dataset was compressed into 8 channels using the method proposed by Zhang et al (20). The resulting compressed images are very similar to the original, as shown by the difference images

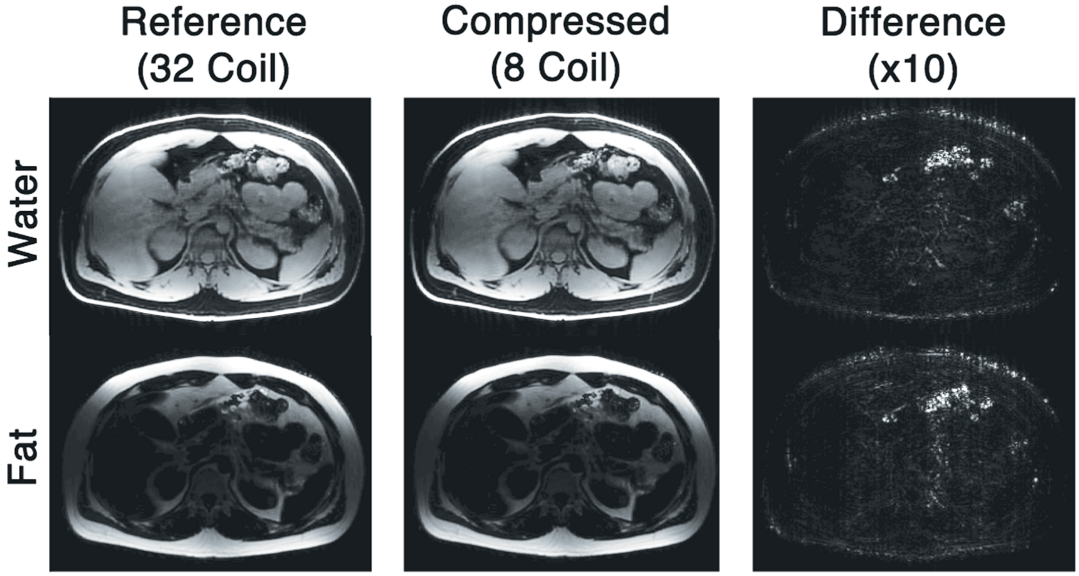

Figure 3.7 Water and fat images of 32 coil, 3D abdominal data with (8 virtual coils) and without (32 coils) coil compression. Water and fat difference images (amplified by a factor of 10) show the accuracy of the coil compression. Images were acquired at a net acceleration factor of 3.1.

amplified by a factor of 10. Reconstruction time was reduced from 2.3 hours to 37 minutes, a factor of 3.7 improvement.

3.5 Discussion

R_2^* correction is a necessary pre-requisite for quantitative water-fat imaging (30). The importance of correcting for R_2^* is particularly evident in regions of high R_2^*, such as the bone marrow (Figure 3.2). Bone marrow is not the only location in which high R_2^* values are expected. Other cases include but are not limited to iron overload in the liver (31) and heart (32).

For a prospective undersampling study (Figure 3.6), a complete abdominal cavity scan was chosen. This scan is particularly difficult to obtain in a single breath-hold due the large volume being imaged. Attempts to accelerate image acquisition using parallel imaging resulted in a minimum acquisition time of 25s before artefacts due to noise-amplification became significant (33). Breath-holds of 25s are too long for many patients, especially for obese patients for whom there is much interest in measuring the total visceral and subcutaneous adipose tissue (4,34,35).

One limitation of integrated compressed sensing, parallel imaging, and water-fat separation reconstructions is lengthy reconstruction time. Since reconstruction time scales non-linearly with the number of coils in the data set, coil compression (20) was examined as a potential method to reduce computation time by reducing dataset size. As seen in Figure 3.6, 32 coil datasets were compressed into 8 virtual-coil datasets without any noticeable degradation of image quality. This resulted in an approximately fourfold reduction in reconstruction time. It is important to note that when coil compression is applied to multi-echo phase sensitive reconstructions, the same compression matrix should be applied to each echo. Using different compression matrices for each compressed echo results in each echo having a different effective coil sensitivity, which is problematic when the absolute phase of the coil sensitivity is not known (36). Calibration of the coil sensitivities with a single echo preserves the relative phases between echo images which is critical for phase-sensitive reconstructions.

The calf was chosen for our examination of the effect of temporal incoherence for two reasons: there are no significant limitations in acquiring an artefact free fully sampled reference and the blood vessels in the calf provide some relatively low contrast objects. Loss of low contrast objects is a common artifact seen in compressed sensing reconstructions. It was postulated that when the acceleration factors were increased, compressed sensing artefacts would appear in reconstructions using the same sampling on each echo before they appear for different sampling patterns for each echo. In addition to the loss of low contrast objects, coherent artefacts were also seen in the images. The same effect is expected in the liver but it is difficult to see since fully sampled references are difficult to obtain due to restrictions on the total acquisition time imposed by the need to use a breath hold to eliminate motion artefact.

The signal model presented in Eqn. 3.1 represents a model for water-fat separation that allows for independent phases of water and fat. However, for most standard types of radiofrequency excitation, the Bloch equations indicate that the phases should be equal at

TE=0 (37). Constraining the initial phase reduces the number of free parameters by converting four linear parameters (magnitude and phase of water and fat) into two linear parameters (magnitude of water and fat) and one non-linear parameter (common phase of water and fat). The reduction in the number of free parameters increases SNR (38). In the future work, it would be interesting to investigate the phase constrained model.

The proposed pulse sequence uses small y and z gradients or blips during the fly-back to allow sampling of different locations in *k*-space for each echo. Allowing each echo to be sampled with different undersampling patterns adds additional incoherence to improve the reconstruction, as shown in Figure 3.4, particularly at high acceleration factors. This sampling strategy has been previously proposed in the context of water-fat imaging (18,19,25); however, to our knowledge, this is the first time this sampling strategy has been implemented for prospectively undersampled water-fat imaging (Figure 3.5, Figure 3.6). Previous studies have used either used retrospective undersampling (18,19) or prospective undersampling with the same sampling pattern for each echo (25).

The amplitude of these blips should be kept small to minimize induced eddy currents and resultant phase errors (39). Phase errors due to eddy currents have been shown to lead to inaccurate water and fat estimates (40,41). The temporal incoherence of the additional gradients in this application could lead to particularly complicated phase error patterns.

3.6 Conclusion

This work describes an integrated compressed sensing, parallel imaging, and water-fat separation technique capable of reconstructing R_2^* corrected water and fat images from highly undersampled datasets. Acceleration factors as high as seven were demonstrated with excellent image quality. At these high acceleration factors this new technique offers significant improvement in image quality over water-fat acquisitions accelerated using parallel imaging alone. These higher acceleration factors allow water and fat images with higher resolution or larger imaging volumes for breath-hold restricted applications.

3.7 References

1. Hussain HK, Chenevert TL, Londy FJ, Gulani V, Swanson SD, McKenna BJ, Appelman HD, Adusumilli S, Greenson JK, Conjeevaram HS. Hepatic fat fraction: MR imaging for quantitative measurement and display--early experience. Radiology 2005;237(3):1048-1055.

2. Schick F, Weiss B, Einsele H. Magnetic resonance imaging reveals a markedly inhomogeneous distribution of marrow cellularity in a patient with myelodysplasia. Ann Hematol 1995;71(3):143-146.

3. Schick F, Einsele H, Lutz O, Claussen CD. Lipid selective MR imaging and localized 1H spectroscopy of bone marrow during therapy of leukemia. Anticancer Res 1996;16(3B):1545-1551.

4. Kuk JL, Katzmarzyk PT, Nichaman MZ, Church TS, Blair SN, Ross R. Visceral fat is an independent predictor of all-cause mortality in men. Obesity (Silver Spring) 2006;14(2):336-341.

5. Hu HH, Smith DL, Jr., Nayak KS, Goran MI, Nagy TR. Identification of brown adipose tissue in mice with fat-water IDEAL-MRI. J Magn Reson Imaging 2010;31(5):1195-1202.

6. Kellman P, Hernando D, Arai AE. Myocardial Fat Imaging. Curr Cardiovasc Imaging Rep 2010;3(2):83-91.

7. Liu CY, McKenzie CA, Yu H, Brittain JH, Reeder SB. Fat quantification with IDEAL gradient echo imaging: correction of bias from T(1) and noise. Magn Reson Med 2007;58(2):354-364.

8. Bydder M, Yokoo T, Hamilton G, Middleton MS, Chavez AD, Schwimmer JB, Lavine JE, Sirlin CB. Relaxation effects in the quantification of fat using gradient echo imaging. Magn Reson Imaging 2008;26(3):347-359.

9. Yu H, Shimakawa A, McKenzie CA, Brodsky E, Brittain JH, Reeder SB. Multiecho water-fat separation and simultaneous R2* estimation with multifrequency fat spectrum modeling. Magn Reson Med 2008;60(5):1122-1134.

10. Hamilton G, Yokoo T, Bydder M, Cruite I, Schroeder ME, Sirlin CB, Middleton MS. In vivo characterization of the liver fat (1)H MR spectrum. NMR Biomed 2011;24(7):784-790.

11. Yu H, McKenzie CA, Shimakawa A, Vu AT, Brau AC, Beatty PJ, Pineda AR, Brittain JH, Reeder SB. Multiecho reconstruction for simultaneous water-fat decomposition and T2* estimation. J Magn Reson Imaging 2007;26(4):1153-1161.

12. Chebrolu VV, Hines CD, Yu H, Pineda AR, Shimakawa A, McKenzie CA, Samsonov A, Brittain JH, Reeder SB. Independent estimation of T*2 for water and fat for improved accuracy of fat quantification. Magn Reson Med 2010;63(4):849-857.

13. Griswold MA, Jakob PM, Heidemann RM, Nittka M, Jellus V, Wang J, Kiefer B, Haase A. Generalized autocalibrating partially parallel acquisitions (GRAPPA). Magn Reson Med 2002;47(6):1202-1210.

14. Pruessmann KP, Weiger M, Scheidegger MB, Boesiger P. SENSE: sensitivity encoding for fast MRI. Magn Reson Med 1999;42(5):952-962.

15. Pruessmann KP, Weiger M, Bornert P, Boesiger P. Advances in sensitivity encoding with arbitrary k-space trajectories. Magn Reson Med 2001;46(4):638-651.

16. Lustig M, Donoho D, Pauly JM. Sparse MRI: The application of compressed sensing for rapid MR imaging. Magn Reson Med 2007;58(6):1182-1195.

17. Lustig M, Pauly JM. SPIRiT: Iterative self-consistent parallel imaging reconstruction from arbitrary k-space. Magn Reson Med 2010;64(2):457-471.

18. Doneva M, Bornert P, Eggers H, Mertins A, Pauly J, Lustig M. Compressed sensing for chemical shift-based water-fat separation. Magn Reson Med 2010;64(6):1749-1759.

19. Sharma SD, Hu HH, Nayak KS. Accelerated water-fat imaging using restricted subspace field map estimation and compressed sensing. Magn Reson Med 2012;67(3):650-659.

20. Zhang T, Pauly JM, Vasanawala SS, Lustig M. Coil compression for accelerated imaging with Cartesian sampling. Magn Reson Med 2012. doi: 10.1002/mrm.24267.

21. Buehrer M, Pruessmann KP, Boesiger P, Kozerke S. Array compression for MRI with large coil arrays. Magn Reson Med 2007;57(6):1131-1139.

22. Doneva M, Bornert P. Automatic coil selection for channel reduction in SENSE-based parallel imaging. MAGMA 2008;21(3):187-196.

23. Dunbar D, Humphreys G. A spatial data structure for fast Poisson-disk sample generation. In Proceedings of SIGGRAPH, Boston, Massachusetts 2006:503-508.

24. Lustig M, Alley M, Vasanawala S, Donoho D, Pauly JM. L1 SPIR-iT: Autocalibrating Parallel Imaging Compressed Sensing. In: Proceedings of 17th Annual Meeting of ISMRM, Honolulu, Hawaii 2009:334.

25. Sharma SD, Hu HH, Nayak KS. Chemical shift encoded water-fat separation using parallel imaging and compressed sensing. Magn Reson Med 2012. doi: 10.1002/mrm.24270.

26. Hu S, Lustig M, Balakrishnan A, Larson PE, Bok R, Kurhanewicz J, Nelson SJ, Goga A, Pauly JM, Vigneron DB. 3D compressed sensing for highly accelerated hyperpolarized (13)C MRSI with in vivo applications to transgenic mouse models of cancer. Magn Reson Med 2010;63(2):312-321.

27. McKenzie CA, Yeh EN, Ohliger MA, Price MD, Sodickson DK. Self-calibrating parallel imaging with automatic coil sensitivity extraction. Magn Reson Med 2002;47(3):529-538.

28. Kellman P, McVeigh ER. Image reconstruction in SNR units: a general method for SNR measurement. Magn Reson Med 2005;54(6):1439-1447.

29. Buckheit J, Chen S, Donoho D, Johnstone I, Scargle K. About Wavelab. Wavelab software package version 0700. Technical Report Standord, CA: Department of Statistics, Stanford University 1995.

30. Reeder SB, Hu HH, Sirlin CB. Proton density fat-fraction: A standardized mr-based biomarker of tissue fat concentration. J Magn Reson Imaging 2012. doi: 10.1002/jmri.23741.

31. Hankins JS, McCarville MB, Loeffler RB, Smeltzer MP, Onciu M, Hoffer FA, Li CS, Wang WC, Ware RE, Hillenbrand CM. R2* magnetic resonance imaging of the liver in patients with iron overload. Blood 2009;113(20):4853-4855.

32. Anderson LJ, Holden S, Davis B, Prescott E, Charrier CC, Bunce NH, Firmin DN, Wonke B, Porter J, Walker JM, Pennell DJ. Cardiovascular T2-star (T2*) magnetic resonance for the early diagnosis of myocardial iron overload. Eur Heart J 2001;22(23):2171-2179.

33. Addeman BT, Soliman AS, Wiens CN, McKenzie CA. Volumetric Fat Quantification of Intra-Abdominal Adipose Tissue from a Single Breath Hold Acquisition. In Proceedings of 20th Annual Meeting of ISMRM, Melbourne, Australia 2012:4172.

34. Al-Attar SA, Pollex RL, Robinson JF, Miskie BA, Walcarius R, Little CH, Rutt BK, Hegele RA. Quantitative and qualitative differences in subcutaneous adipose tissue stores across lipodystrophy types shown by magnetic resonance imaging. BMC Med Imaging 2007;7:3.

35. Positano, Gastaldelli, Sironi, Santarelli, Lombardi, Landini. An Accurate and Robust Method for Unsupervised Assessment of Abdominal Fat by MRI. Journal of Magnetic Resonance Imaging 2004;20:684-689.

36. Brau AC, Beatty PJ, McKenzie CA, Yu H, Shimakawa A, Reeder SB, Brittain JH. The Impact of Parallel Imaging Reconstruction on Image Phase: Implications for Phase-sensitive Imaging. In Proceedings of 16th Annual Meeting of ISMRM, Toronto, Ontario 2008:1279.

37. Carl M, Chiang JT. Investigations of the origin of phase differences seen with ultrashort TE imaging of short T2 meniscal tissue. Magn Reson Med 2012;67(4):991-1003.

38. Bydder M, Yokoo T, Yu H, Carl M, Reeder SB, Sirlin CB. Constraining the initial phase in water-fat separation. Magn Reson Imaging 2011;29(2):216-221.

39. Haacke EM, Brown RW, Thompson MR, Venkatesan R. Magnetic Resonance Imaging: Physical Principles and Sequence Design. New York: Wiley-Liss; 1999.

40. Hernando D, Hines CD, Yu H, Reeder SB. Addressing phase errors in fat-water imaging using a mixed magnitude/complex fitting method. Magn Reson Med 2012;67(3):638-644.

41. Yu H, Shimakawa A, Hines CD, McKenzie CA, Hamilton G, Sirlin CB, Brittain JH, Reeder SB. Combination of complex-based and magnitude-based multiecho water-fat separation for accurate quantification of fat-fraction. Magn Reson Med 2011;66(1):199-206.

Chapter 4

4 Accelerated ^{13}C Chemical Shift Imaging of Hyperpolarized Pyruvate

4.1 Introduction

Low natural abundances and smaller gyromagnetic ratios (resulting in poor thermal polarization) have limited the use of spectroscopy and imaging of non-hydrogen nuclei such as carbon-13 (^{13}C). Hyperpolarization of ^{13}C enriched substrates through dynamic nuclear polarization (DNP) offers signal enhancements of approximately 10,000 fold relative to thermal ^{13}C imaging (1) thereby enabling many novel applications. These applications include imaging of *in vivo* metabolism through spectroscopy or spectroscopic imaging techniques. Among the many substrates that have been proposed (2-6), [1-^{13}C] pyruvate is the most commonly used due to its favourable characteristics including high levels of polarization, relatively long T_1, and its intersection into several metabolic pathways.

The small concentration and short lifetime of a hyperpolarized substrate limit the time window available for acquisition. Immediately after removal from the polarizer, hyperpolarized substrates begin to decay back their thermal equilibrium at rate determined by the substrate's T_1. Furthermore, unlike the thermal polarization case, the signal in a hyperpolarized experiment is non-renewable. Any radiofrequency excitations will irreversibly consume a portion of the hyperpolarized signal. As such, efficient spectroscopic techniques are necessary.

Model based approaches have been proposed as an efficient spectroscopic technique for metabolic imaging of ^{13}C metabolites (7-9) based on work done in water-fat imaging (10). These techniques use prior knowledge of the chemical shifts between each metabolite to separate the signal due to each metabolite from only few images at optimally chosen echo times (7,11). By using prior knowledge of the spectral locations of each metabolite, these model based approaches offer significant reductions in the spectral sampling required to resolve each metabolite.

Image acceleration using compressed sensing has been achieved for both proton (12) and hyperpolarized ^{13}C imaging (13-15). Previous work in the field of water-fat imaging (16-18) and hyperpolarized ^{13}C spectroscopic imaging (13-15) has examined the use of compressed sensing techniques that exploit sub-sampling in both the spatial and spectral dimensions. A necessary requirement for a successful compressed sensing reconstruction is an incoherent point spread function. Exploiting sub-sampling in a higher dimensional space results in improved incoherence (18), a particular important result for low resolution imaging like hyperpolarized ^{13}C spectroscopic imaging where generating an incoherent artefact is difficult.

The ^{13}C gyromagnetic ratio is approximately four times smaller than the ^{1}H gyromagnetic ratio. This results in a requirement for a four-fold increase in gradient strength (and slew rates) when compared to proton imaging in order to achieve the same image resolution. This results in slower flyback durations, thereby limiting the echo-train lengths (ETL) that can be achieved while still maintaining SNR optimal echo times. Thus, high performance gradients can be used to accelerate ^{13}C image acquisitions (19).

In this chapter, we propose a model based approach to separate pyruvate and its metabolites. We show that the proposed method can use compressed sensing to accelerate image acquisition. This approach was validated using digital phantoms and thermal phantoms and demonstrated in a variety of 3D *in vivo* experiments. We also show that high performance gradients can be used to accelerate the proposed method, by increasing echo trains lengths and thereby reducing the number of radiofrequency excitations required. This approach was demonstrated in a dynamic 3D *in vivo* experiment.

4.2 Theory

4.2.1 Signal Model

In model based chemical shift imaging, the chemical shift between pyruvate and each metabolite is assumed known. Then by acquiring multiple images acquired at N different echo times the signal due to each metabolite can be separated. At any position p, the signal from the nth echo image I_n^p can be described as the sum of the signal due to each of the M metabolites

$$I_n^p = \sum_{m=1}^{M} \rho_m^p \cdot e^{i2\pi\Delta f_m t_n} \cdot e^{i2\pi\psi^p t_n} \qquad 4.1$$

where ρ_m^p is the signal due to the mth metabolite, Δf_m is the chemical shift difference between the mth metabolite and pyruvate, and ψ^p is the field map. Alternatively, Eqn. 4.1 can be written in matrix notation as

$$\boldsymbol{I^p} = \Psi^p \Gamma \boldsymbol{\rho^p} \ , \qquad 4.2$$

where

$$\Psi^p = \begin{bmatrix} e^{i2\pi\psi^p t_1} & 0 & 0 \\ 0 & \ddots & 0 \\ 0 & 0 & e^{i2\pi\psi^p t_N} \end{bmatrix}, \qquad 4.3$$

$$\Gamma = \begin{bmatrix} e^{i2\pi\Delta f_m t_1} & \dots & e^{i2\pi\Delta f_M t_1} \\ \vdots & \ddots & \vdots \\ e^{i2\pi\Delta f_m t_N} & \dots & e^{i2\pi\Delta f_M t_N} \end{bmatrix}, \qquad 4.4$$

$$\boldsymbol{I^p} = \left[I_1^p \dots I_N^p\right]^T, \qquad 4.5$$

$$\boldsymbol{\rho^p} = \left[\rho_1^p \dots \rho_M^p\right]^T. \qquad 4.6$$

By extending this single pixel signal model to the entire image, the acquired k-space of the nth echo time ($\boldsymbol{k_n}$) can be described by

$$\boldsymbol{k_n} = F_n \Lambda_n A_n \boldsymbol{\rho} \ , \qquad 4.7$$

where ρ is the concatenation of each metabolite images $\boldsymbol{\rho} = [\rho_1^1, \dots, \rho_1^P, \dots, \rho_M^1, \dots, \rho_M^P]^T$, A_n is a PxM·P matrix consisting of M concatenated PxP matrices with the mth matrix consisting of the identity matrix scaled by $e^{i2\pi\Delta f_m t_n}$, Λ_n is a PxP diagonal matrix with element $e^{i2\pi\psi^p t_n}$ at the pth diagonal, and F_n is the undersampled Fourier transform operator.

4.2.2 Proposed Method

Estimates of the unknowns, the metabolite images and field map, can be estimated using an iterative, two step approach like those proposed in water-fat imaging (10,18). In the first step, the field map is fixed and estimates of the metabolite images are made. In the second step, the metabolite images are fixed and the field map is updated. This process of sequentially updating the metabolite images and field map is repeated until the change in the field map is small. By adding constraints to the metabolite images and field map, these estimates can be made from undersampled datasets.

4.2.3 Metabolite Estimation

In the case in which the field map is known, the metabolite images can be estimated by solving the following optimization problem

$$\underset{\boldsymbol{\rho}}{argmin} \sum_{n=1}^{N} \|F_n \Lambda_n A_n \boldsymbol{\rho} - \boldsymbol{k_n}\|_2^2 + \sum_{m=1}^{M} \lambda_m \|\Phi_m \boldsymbol{\rho}_m\|_1. \qquad 4.8$$

The first term in Eqn. 4.8 enforces consistency between the acquired data, signal model, and metabolite estimates while the second term promotes sparsity of the metabolite images in transform domain $\boldsymbol{\Phi}_m$. The relative weighting between image fidelity and sparsity of each metabolite image is controlled by the weighting parameter λ_m.

4.2.4 Updating Field Map

The field map can be considered to contain two components, a spatially dependent component that describes the uniformity of the B_0 field (ψ'^p) and an offset that describes how far off-resonance the carrier frequency is from the actual resonance (ψ_{offset})

$$\psi^p = \psi'^p + \psi_{offset} \qquad 4.9$$

In this text two methods are referred to: the constant field map and spatially varying methods. In the constant field map method, the field map over the field of view is assumed uniform ($\psi'^{p} = 0$ in Eqn. 4.9). In the spatially varying method, the first term is mapped by multiplying the ratio of the gyromagnetic ratios of carbon and protons by a B_0 map measured using proton imaging. Therefore, only the constant offset requires measuring.

In the case where the field map is not known, the optimization problem posed in Eqn. 4.8 becomes non-convex. Based on previous methods proposed for water-fat separation (10,16,18), the proposed method is to linearize the problem and solve the linearized version for the update terms:

$$\underset{\boldsymbol{\Delta\rho}}{argmin} \sum_{n=1}^{N} \|\boldsymbol{\delta_n} + F_n \Lambda_n B_n \boldsymbol{\Delta\rho}\|_2^2 + \sum_{m=1}^{M} \lambda_m \|\Phi_m(\boldsymbol{\rho}_m + \boldsymbol{\Delta\rho_m})\|_1. \qquad 4.10$$

where δ_n describes the residual of the current metabolite estimates mapped to k-space and the acquired k-space:

$$\boldsymbol{\delta_n} = F_n \Lambda_n A_n \boldsymbol{\rho} - \boldsymbol{k_n}. \qquad 4.11$$

Here, $\Delta\rho$ describes the concatenation of the metabolite image and field map update terms $\boldsymbol{\Delta\rho} = [\Delta\rho_1^1, \ldots, \Delta\rho_1^P, \ldots, \Delta\rho_M^1, \ldots, \Delta\rho_M^P, \Delta\psi, \ldots, \Delta\psi]^T$ and B_n is a Px(M+1)·P matrix consisting again of M+1 concatenated matrices where matrices 1:M are PxP matrices with the mth matrix consisting of the identity matrix scaled by $e^{i2\pi\Delta f_m t_n}$ and the M+1 matrix consisting of a PxP diagonal matrix with pth element $2\pi i t_n \sum_{m=1}^{M} \rho_m^p e^{i2\pi\Delta f_m t_n}$. It is important to note that the field map update term $\Delta\psi$ is restricted in Eqn. 4.10 such that it is spatially invariant. Any spatial variations in the field map are incorporated through the Λ_n matrix.

4.2.5 Sampling

An incoherent point spread function is a necessary component of any compressed sensing reconstruction. Unfortunately, SNR limitations restrict hyperpolarized experiments to low resolution acquisitions making it difficult to acquire enough k-space samples to generate an incoherent artefact. To improve the incoherence of the acquisition, different variable density random undersampling patterns were used for each echo. This has been shown in both water-fat and hyperpolarized ^{13}C experiments to improve incoherence (13,14,18).

4.2.6 Extension to Dynamic Imaging

Equation 4.10 describes the process of updating the field map for a single time-point acquisition. In the case of dynamic imaging where images are acquired at multiple time points, the field map should not change over the time course of a hyperpolarized experiment. The optimization problem posed in Eqn. 4.10 can be modified such the data from all of the time points is used to estimate the field map. In a dynamic acquisition consisting of T time points, the optimization problem described in Eqn. 4.10 is changed to

$$\underset{\boldsymbol{\Delta\rho}}{argmin} \sum_{n=1}^{N}\sum_{\tau=1}^{\mathrm{T}} \| \boldsymbol{\delta_n^\tau} + F_n \Lambda_n B_n^\tau \boldsymbol{\Delta\rho^\tau} \|_2^2 + \sum_{\tau=1}^{\mathrm{T}}\sum_{m=1}^{M} \lambda_m \| \Phi_m(\boldsymbol{\rho_m^\tau} + \boldsymbol{\Delta\rho_m^\tau}) \|_1. \qquad 4.12$$

where $\boldsymbol{\rho}^\tau$ and $\boldsymbol{\Delta\rho^\tau}$are now the concatenation of metabolite images and update terms acquired at time point τ. The field map uptake term contained in $\boldsymbol{\Delta\rho^\tau}$ is restricted such that it is constant in both space and time.

4.3 Methods

4.3.1 Simulated Experiments

Chemical shift encoded acquisitions were simulated using MATLAB (R2013, The MathWorks, Natick, MA, USA). This digital phantom consisted of four circles containing five metabolites (pyruvate and pyruvate hydrate mixture, alanine, lactate, and bicarbonate) with known chemical shift at 3T (0, 269Hz, 179Hz, 388Hz, -339Hz). The initial echo time and echo spacing was set to 2.1ms and 1.1ms respectively. Field maps were generated using a third order polynomial to investigate the proposed reconstruction under the conditions of low and high B_0 inhomogeneity. In the case of low B_0 inhomogeneity a field map varying by approximately 25Hz across the field of view was generated, a realistic value estimated from multiple field maps. In the case of high B_0 inhomogeneity a field map varying by approximately 80Hz across the field of view was generated, a realistic value estimated from field maps obtained while using the insert gradients. Pyruvate to pyruvate hydrate, alanine, lactate, and bicarbonate ratios were set to values consistent with measurements made in the heart of 8:1, 6.6:1, 4:1, and 4:1. Noise was added to the datasets such that the SNR of the pyruvate images was 50:1.

4.3.2 Phantom Validation

The proposed reconstruction and pulse sequence were validated using four ^{13}C enriched phantoms each containing of the following substrates: formic acid (two spectral components with chemical shifts of 1 Hz and -220 Hz relative to pyruvate), alanine, lactate, and bicarbonate. Imaging parameters were as follows: 5mm in-plane resolution, slice thickness=1.0cm, initial TE=1.6ms, ΔTE=1.2ms, Number of Echoes=9, echo train length=9, bandwidth=±6.4kHz, and NEX=40.

4.3.3 *in vivo* Experiments

To test the feasibility of the proposed reconstruction, fully sampled and prospectively undersampled hyperpolarized experiments were performed on Sprague-Dawley rats and a 129X1/SvJ mouse using either clinical (peak strength=50mT/m, peak slew rate=200T/m/s) or high-performance insert gradients (peak strength=500mT/m, peak slew rate=3300T/m/s).

All experiments were performed at 3T (MR 750, GE Healthcare, Waukesha, WI, USA) using a broadbanded variant of the IDEAL-SPGR pulse sequence capable of arbitrary sampling patterns (Figure 3.1). Small y and z gradients were applied during the readout rewinder allowing each echo to have different sampling patterns. Radiofrequency excitation was performed using a non-selective hard pulse. For each study, the flip angle was calibrated using a prescan of a ^{13}C enriched acetate phantom. In addition ^{1}H T_1-weighted spoiled gradient echo images were acquired for image overlay.

Custom built single channel coils were used for all experiments. For mouse experiments, data were acquired using a switch-tuned $^{1}H/^{13}C$ birdcage coil (20). For rat experiments, carbon data were acquired using a ^{13}C-only birdcage coil while proton images were acquired using a 32 coil array (3.0T 32Ch Cardiac coil, Invivo, Gainesville, Florida, USA). For insert gradient rat experiments, data were acquired using a ^{13}C-only and ^{1}H-only birdcage coils.

[1-^{13}C]-enriched pyruvic acid (CIL, Cambridge MA) was mixed with an aqueous solution of OX063 (61 mM) and ProHance (2.9 mM). The sample was hyperpolarized in a dissolution DNP polarizer (Hypersense, Oxford Instruments, Abingdon, UK) at 1.4 K, 94.1 GHz, and 50 mW.

All experiments were performed with ethical approval obtained from the institutional animal use subcommittee. Prepolarized [1-^{13}C] pyruvate was injected via a tail-vein catheter. Breathing rate and temperature were monitored and held constant throughout each acquisition. For the mouse study, a volume of 0.250 ml of hyperpolarized medium was injected. For the rat studies, a volume of 2.5 ml of hyperpolarized medium was injected.

Using clinical gradients, a fully encoded 3D dataset spanning the entire rat body was acquired 25s after start of injection of hyperpolarized [1-^{13}C] pyruvate. Imaging parameters were as follows: 5mm isotropic resolution, FOV=12.0x9.6x6.0cm, TE_1=1.9ms, ΔTE=1.1ms, Number of Echoes=9, Flip Angle=5°, echo train length = 3, readout bandwidth= 5.0kHz, and acquisition time = 9s.

Using clinical gradients, a prospectively undersampled 3D dataset spanning the entire mouse body was acquired 25s after start of injection. Imaging parameters were as follows: 4.2mm in-plane resolution, 5mm slice thickness, FOV=10.0x8.0x6.0cm, TE_1=1.7ms, ΔTE=1.1ms, Number of Echoes=9, Flip Angle=5°, echo train length = 3, readout bandwidth= 6.4kHz, acceleration factor=2, and acquisition time = 4s.

Using high performance insert gradients, fully sampled dynamic 3D datasets of a rat were acquired at 15s, 25s, and 35s after the start of injection. Imaging parameters were as follows: 5mm isotropic resolution, FOV=12.0x9.6x6.0cm, TE_1=0.9ms, ΔTE=1.1ms, Number of Echoes=9, echo train length=9, bandwidth=±13.9kHz, variable flip angle

(21,22) and acquisition time per time point=2s. An estimate of the proton field inhomogeneity was measured using a ^{1}H IDEAL-SPGR sequence over an identical field of view. Proton field maps were reconstructed using the Max-IDEAL reconstruction (23).

4.3.4 Reconstruction Implementation

The proposed method was implemented using MATLAB (R2013, The MathWorks, Natick, MA, USA) on a MacBook Pro laptop (Apple Computer, Cupertino, CA, USA). A model consisting of five species (pyruvate, pyruvate hydrate, lactate, alanine, bicarbonate) was used. A non-linear conjugate gradient reconstruction (12) was used to minimize the cost functions describe in Eqn. 4.8, Eqn 4.10, and Eqn. 4.12. Both finite difference and wavelet transformations were used as sparsifying transformations for the metabolite images. The open-source package Wavelab was used to compute the wavelet transformation (24). In this work, the max signal intensities were set to 1000 and each sparsity weighting factor was set to 50.

4.4 Results

4.4.1 Digital Simulations

Digital phantoms were used to investigate if the spatially varying component of the field map was necessary. Metabolite maps were reconstructed using simulated field maps with similar B_0 inhomogeneity to that found *in vivo* when clinical gradients (low B_0 inhomogeneity) and high performance insert gradients are used (high B_0 inhomogeneity). Figure 4.1 shows metabolite maps on pyruvate, lactate, alanine, and bicarbonate estimated for cases of low B_0 inhomogeneity and high B_0 inhomogeneity. For each case, metabolite maps were reconstructed using constant field map and spatially varying field map estimates. For B_0 inhomogeneity comparable to that seen in the insert gradients, the assumption of a uniform B_0 results in an inaccurate separation of metabolite signal and a spatially varying component should be included. Based on these simulations, a uniform field map assumption was used when clinical gradients were used. When insert gradients were used, proton field maps were used to measure the B_0 field for carbon data acquisition.

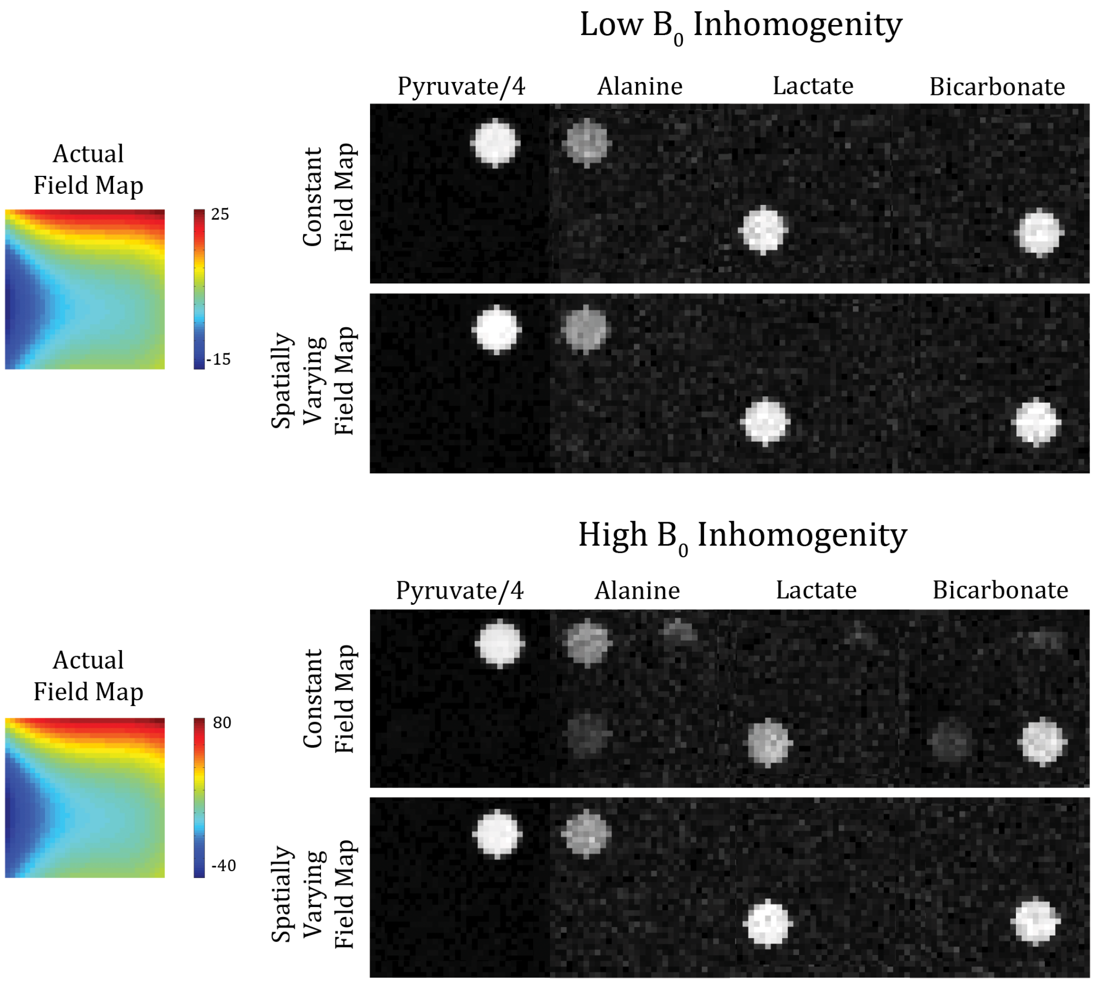

Figure 4.1 Digital phantom simulation of metabolite separation. Metabolite images with chemical shifts corresponding to pyruvate, pyruvate hydrate, lactate, alanine, and bicarbonate were reconstructed using the proposed reconstruction for cases of low and high B_0 inhomogeneity. For each case, metabolite images were reconstructed assuming a constant field map and a spatially varying field map.

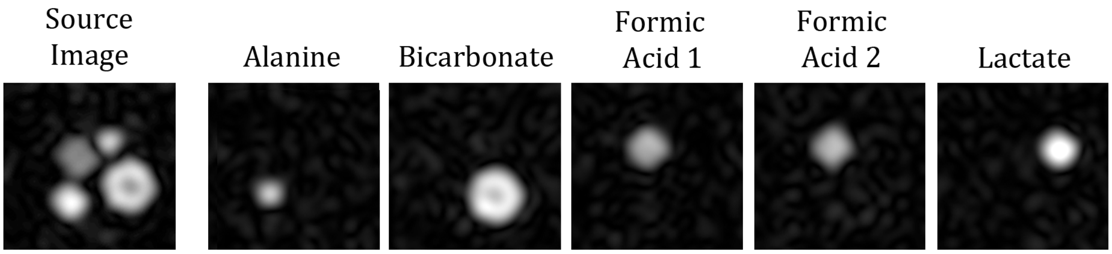

Figure 4.2 Four ^{13}C enriched phantoms containing alanine, lactate, formic acid, and lactate separated using the proposed reconstruction. Results show uniform separation of each component. Formic acid consists of two equal spectral components (doublet). As expected the proposed reconstruction broke the two components of formic acid into two equal components.

4.4.2 Phantom Validation

The proposed reconstruction and pulse sequences were validated using ^{13}C enriched phantoms. Figure 4.2 shows axial images of alanine, lactate, formic acid, and bicarbonate separated using the proposed reconstruction. The proposed reconstruction provides excellent separation of the different spectral components. Formic acid is a doublet and the signal from the formic acid phantom components two equal components.

4.4.3 3D *in vivo* Metabolic Separation

The feasibility of accelerating metabolic imaging using compressed sensing was investigated using retrospective decimation. Figure 4.3 shows the coronal pyruvate (scaled down by a factor of 4), alanine, lactate, and bicarbonate metabolite images of a rat at acceleration factors of 1, 2 and 3. In regions of high SNR, such as the entire pyruvate image, excellent image fidelity is observed. However, at an acceleration factor of 3, significant deviations from the reference image are appearing in regions with low SNR. Arrows point to the heart in the bicarbonate image, a region where such changes are seen.

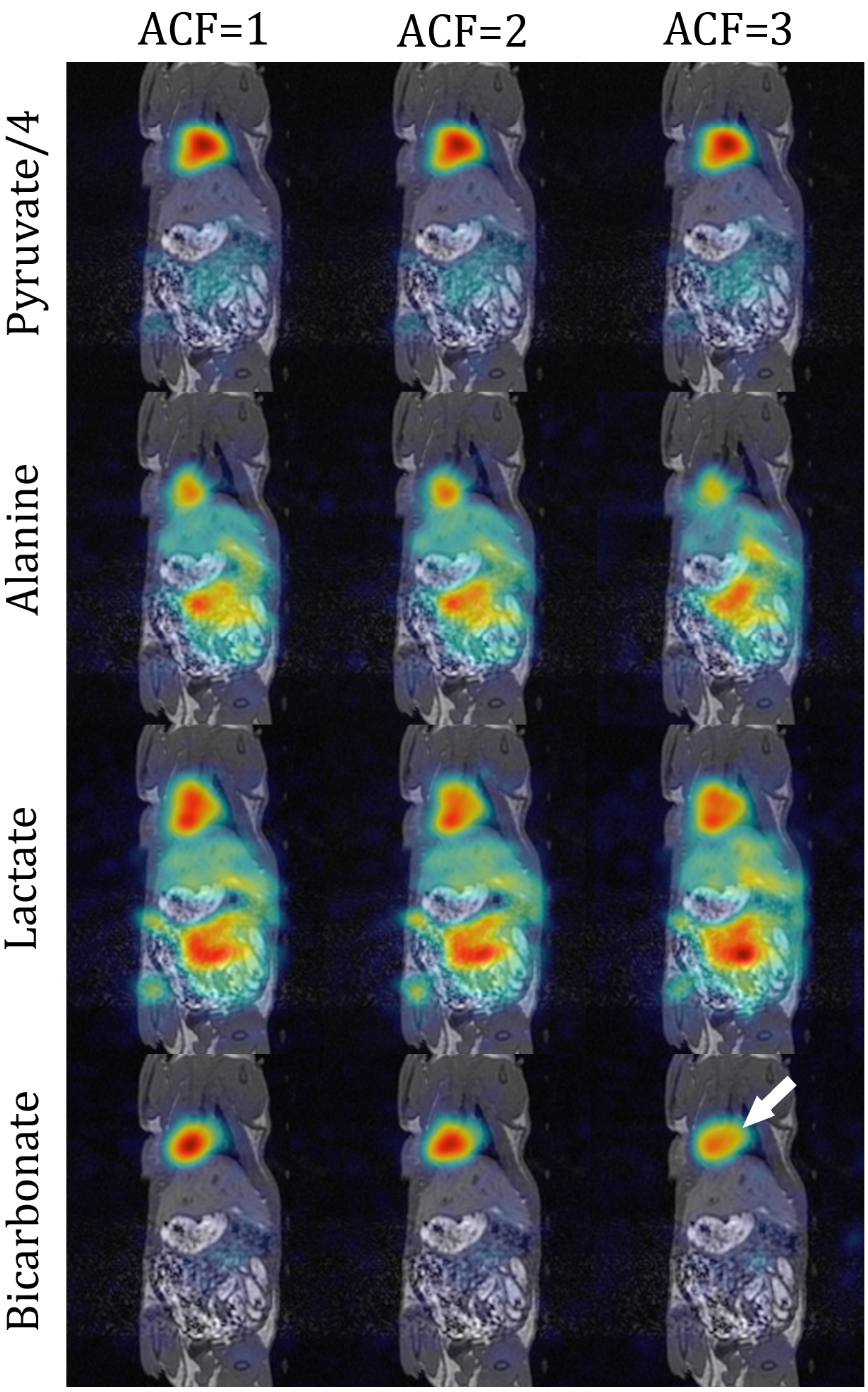

Figure 4.3 Pyruvate, lactate, alanine, and bicarbonate images of 3D rat data using the proposed method retrospectively undersampled at acceleration factors of 1, 2, and 3. A variable density random undersampling pattern (different pattern for each echo) was used. The arrow points to artefacts in the bicarbonate image caused by over accelerating the image.

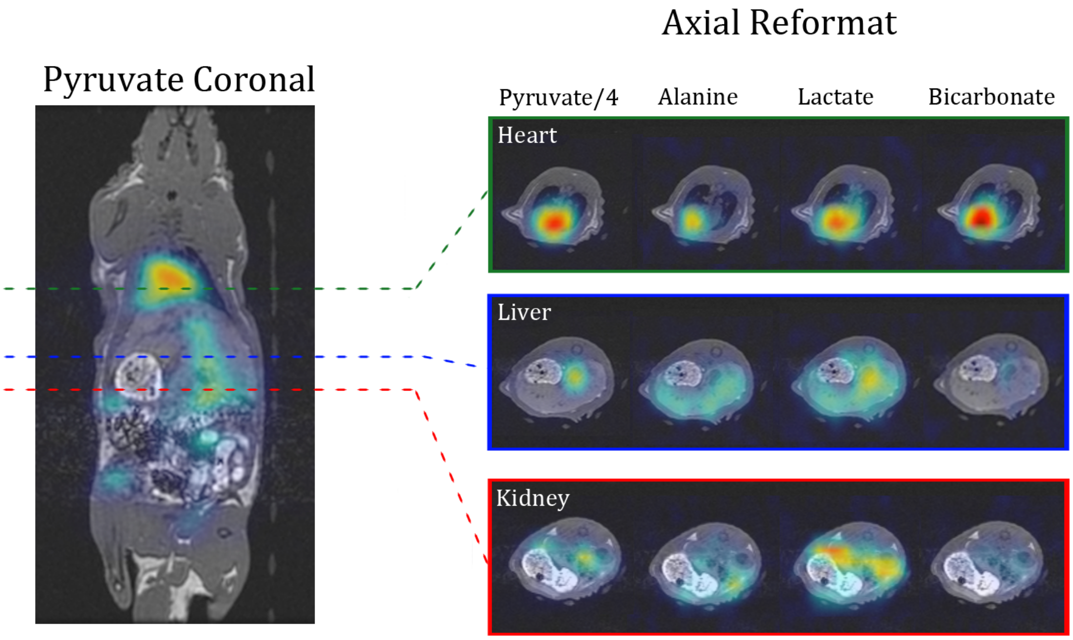

Figure 4.4 Metabolite maps of a dataset of an entire rat body reconstructed using the proposed method. Three horizontal lines are shown on the coronal pyruvate image corresponding to the three locations: heart (green), liver (blue), and kidney (blue). Axial reformats of pyruvate, alanine, and lactate images are shown for each location.

Figure 4.4 shows axial reformats of coronal metabolite images of a rat acquired 25s after start of injection overlaid on T_1 weighted spoiled gradient echo images. On the left is a coronal pyruvate image. Axial reformats of pyruvate (scaled down a factor of 4), alanine, lactate, and bicarbonate images are shown on the right at the heart (green), liver (blue), and kidneys (red). These reformatted images align well with the underlying anatomy.

Figure 4.5 shows a prospectively undersampled 3D dataset of a mouse acquired 25s after start of injection. Pyruvate (scaled down by a factor of 4), alanine, and lactate images are shown through various coronal slices throughout the imaging volume. Images were acquired at a net acceleration factor of 2.

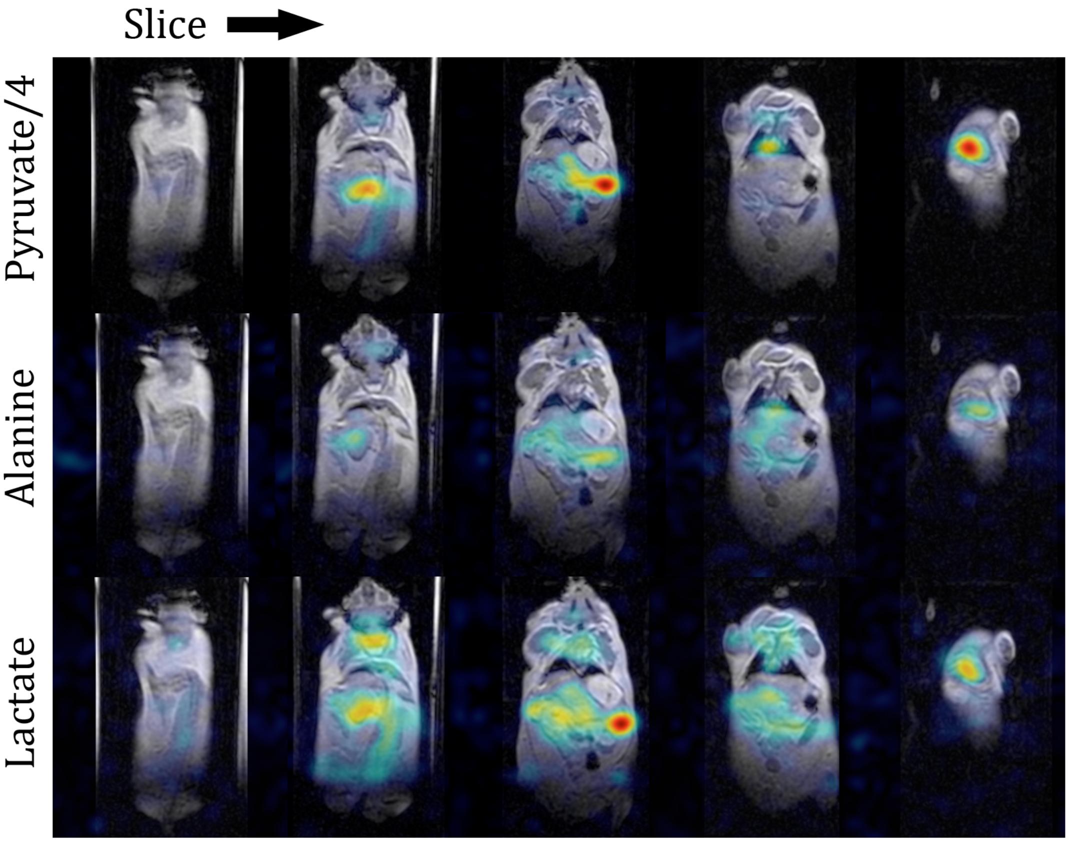

Figure 4.5 A prospectively undersampled 3D dataset of an entire mouse body acquired 25s after start of injection of hyperpolarized [1-^{13}C] pyruvate. Pyruvate, alanine, and lactate images of a 3D mouse dataset prospectively undersampled at an acceleration factor of 2.

Figure 4.6 demonstrates the use of high performance gradients in a dynamic, 3D imaging study of a rat. Pyruvate, alanine, lactate, and bicarbonate images are shown at 15s, 25s, and 35s after start of injection for two locations: heart and kidneys. These high performance gradients allowed for longer echo train length thereby reducing the number of radiofrequency excitations required.

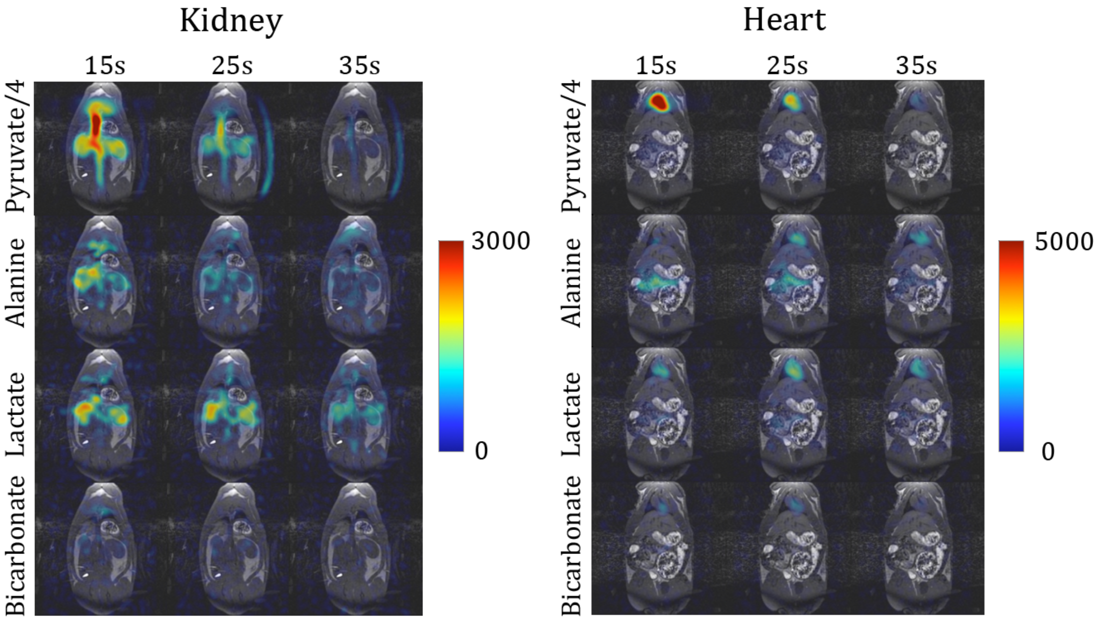

Figure 4.6 Dynamic metabolite maps acquired using high performance insert gradients at 15s, 25s, and 35s after start of injection. Pyruvate was normalized by a factor 4, alanine, lactate, and bicarbonate images are shown over two coronal slices, one through the heart and the other through the kidneys. The two slices were scaled differently for improved dynamic range in the display of the metabolic signals. In addition, the first pyruvate image acquired at 15s after injection was scaled down by an additional factor of 2 (total 8) for improved dynamic range.

The effect of B_0 inhomogeneity on reconstruction accuracy was examined *in vivo* for the case of increased B_0 inhomogeneity introduced when using high performance insert gradients. Figure 4.7 demonstrates this effect using the 25s time-point over the heart from Figure 4.6. Metabolite maps were reconstructed using the constant field map and spatially varying field map methods. In the presence of high B_0 inhomogeneity the constant field map technique begins to significant deviate for the spatially varying technique. This effect is most pronounced in the alanine and lactate images where the inclusion of the spatially varying component of the field map results in a significant reduction in the estimates of lactate and alanine.

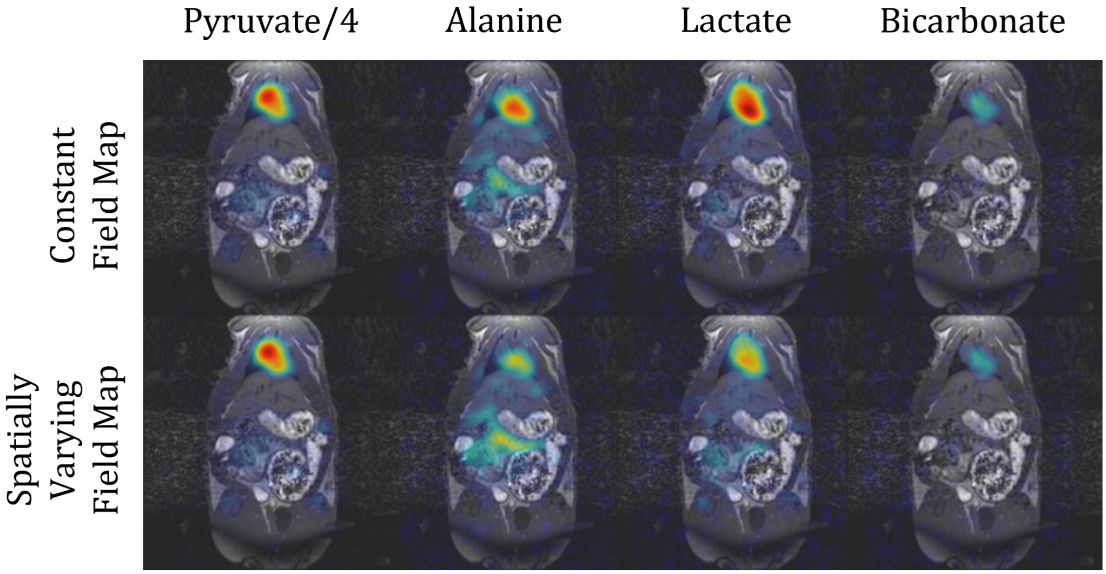

Figure 4.7 Metabolite map of the heart at the 25s time point from the dynamic dataset acquired using high performance insert gradients shown in Figure 4.6. The reconstructed metabolite maps using a constant and spatially varying field map show significantly differences that are particularly evident in the lactate and alanine images.

4.5 Discussion

In this work, a reconstruction framework is demonstrated for reconstruction metabolite images of pyruvate and its metabolites (pyruvate hydrate, alanine, lactate, and bicarbonate) using chemical shift encoding. This method uses compressed sensing to accelerate image acquisitions. Consistency of the data with the signal model is used to estimate B_o inhomogeneity.

Equation 4.9 describes the field map in terms of two components: a spatially varying component and a constant offset term. This offset term describes the difference between the carrier frequency and the resonance frequency of pyruvate. A previously developed chemical shift encoded metabolic imaging method developed by Wiesinger et al (7) solved for the field map by acquiring a spectrum to estimate the offset term and ignoring the spatially varying component. This method uses dataset consistency to estimate the carbon field map, eliminating the need to acquire a spectrum for each dataset. The drawback to not acquiring a spectrum with each scan is that the *a priori* knowledge of the chemical shift differences between each metabolite can longer be verified.

The use of high performance gradients was investigated for further acceleration of image acquisitions. These gradients allowed acquisitions with a longer echo trains length while still maintaining SNR optimal echo spacing (7). However, our control of the gradient amplifiers was too coarse to allow accurate shimming. This resulted in increased B_0 inhomogeneity and necessitated the inclusion of a spatially varying component to accurately describe the field map (Figure 4.1 and Figure 4.7). This spatially varying component was estimated using proton imaging.

In the case of clinical gradients, the assumption that the field map does not vary spatially across the field of view is reasonable for small animal imaging (Figure 4.1). In this case an accurate shim can be obtained and when combined the lower gyromagnetic ratio of ^{13}C, the resulting B_0 inhomogeneity is insignificant. However, it is unclear if this assumption is still valid for the larger field of views (and larger B_0 inhomogeneity) required for translation of these techniques to human applications.

Typically spiral (7,9,25,26) or echo-planar sampling (15,27) schemes imaging have been used for spectroscopic imaging due their fast acquisition time and limited use of radiofrquency excitations. While the reconstruction demonstrated here was validated on a Cartesian acquisition, it could be implemented using 3D stack of spirals, similar to multi-slice spiral acquisition proposed by multislice IDEAL spiral CSI method proposed by Wiesinger et al (7). In the future, the combination of a spiral acquisition scheme and the proposed reconstruction will be examined. The benefits of the proposed reconstruction would include reduced off-resonance blurring due to the inclusion of field inhomogeneity, possibility of acceleration using compressed sensing, and the removal of the need to acquire a calibration spectrum.

Further acceleration of chemical shift imaging is possible through the use of multi-channel coils (28,29) and parallel imaging. A combined parallel imaging, compressed sensing, chemical shift imaging formulism of the proposed reconstruction is straightforward. To include parallel imaging, simply replace the undersampled Fourier transform operator in Eqn. 4.8 and Eqn. 4.10 with an undersampled encoding matrix consisting of coil sensitivity and gradient modulations (Fourier transform modulations). In the case of water-fat imaging, adding parallel imaging has been shown to improve performance (18,30).

Decimation studies were used to the feasibility of accelerating image acquisitions using compressed sensing (Figure 4.3). While these studies do show feasibility, they do not accurately describe the image quality that can be obtained in a prospectively undersampled dataset. Lee et al (31) showed that accelerating image acquisitions with optimized flip-angle selection can lead to improved quality through the use of higher flip angles. Because a large portion of the hyperpolarized signal is being discarded in retrospective studies, it is expected a prospectively undersampled dataset (Figure 4.4) will perform considerably better than a retrospectively decimated datasets. Demonstration of this is difficult as a comparison of datasets from two separate injections would be required.

The use of spectrally selective excitations (9,15,32) whereby the pyruvate resonance is excited with a much lower flip angle than alanine, lactate, and bicarbonate allows preservation of hyperpolarized signal for metabolites of interest. In this implementation, a simple hard pulse was used. Using spectrally selective excitations would improve image quality of pyruvate's metabolites. However, spectral selective excitations require accurate frequency calibration and are susceptible to B_0 inhomogeneity.

The proposed technique was validated using hyperpolarized [1-^{13}C] pyruvate. However, this technique is applicable to metabolic imaging of different hyperpolarized substrates. Some examples include assessment of cell necrosis in tumours using hyperpolarize$^{13}C_2$] fumarate (6) and assessment of Krebs cycle metabolism using hyperpolarized [2-^{13}C] pyruvate (33,34). This technique can be trivially modified for these techniques by changing the spectral model (Δf_m in Eqn 4.1). For SNR efficiency and reconstruction stability, the echo spacing should also be optimized (7,11,26).

4.6 Conclusions

This work describes two methods of accelerating ^{13}C metabolic imaging of [1-^{13}C] pyruvate: an integrated compressed sensing and metabolite separation technique which allows separation of signal due to pyruvate, pyruvate hydrate, alanine, lactate, and bicarbonate from undersampled 3D datasets and through the use of high performance gradient. By exploiting sparsity in both the spatial and spectral dimension, acceleration factors of up to 3 were demonstrated through retrospective and prospective *in vivo* studies. Acceleration of data acquisition was also shown through the use of high performance gradients in a dynamic 3D study. Accelerating metabolic imaging through the use of compressed sensing or high performance gradient can be used to improve resolution, spatial coverage, or temporal resolution. Alternatively, the accelerated metabolic imaging can be used to improve SNR through the use of higher flip angles.

4.7 References

1. Ardenkjaer-Larsen JH, Macholl S, Johannesson H. Dynamic nuclear polarization with trityls at 1.2 K. Applied Magnetic Resonance 2008;34(3-4):509-522.

2. Gallagher FA, Kettunen MI, Day SE, Hu DE, Ardenkjaer-Larsen JH, Zandt R, Jensen PR, Karlsson M, Golman K, Lerche MH, Brindle KM. Magnetic resonance imaging of pH in vivo using hyperpolarized 13C-labelled bicarbonate. Nature 2008;453(7197):940-943.

3. Witney TH, Kettunen MI, Hu DE, Gallagher FA, Bohndiek SE, Napolitano R, Brindle KM. Detecting treatment response in a model of human breast adenocarcinoma using hyperpolarised [1-13C]pyruvate and [1,4-13C2]fumarate. Br J Cancer 2010;103(9):1400-1406.

4. Chen AP, Kurhanewicz J, Bok R, Xu D, Joun D, Zhang V, Nelson SJ, Hurd RE, Vigneron DB. Feasibility of using hyperpolarized [1-13C]lactate as a substrate for in vivo metabolic 13C MRSI studies. Magn Reson Imaging 2008;26(6):721-726.

5. Allouche-Arnon H, Wade T, Waldner LF, Miller VN, Gomori JM, Katz-Brull R, McKenzie CA. In vivo magnetic resonance imaging of glucose - initial experience. Contrast Media Mol Imaging 2013;8(1):72-82.

6. Gallagher FA, Kettunen MI, Hu DE, Jensen PR, Zandt RI, Karlsson M, Gisselsson A, Nelson SK, Witney TH, Bohndiek SE, Hansson G, Peitersen T, Lerche MH, Brindle KM. Production of hyperpolarized [1,4-13C2]malate from [1,4-13C2]fumarate is a marker of cell necrosis and treatment response in tumors. Proc Natl Acad Sci U S A 2009;106(47):19801-19806.

7. Wiesinger F, Weidl E, Menzel MI, Janich MA, Khegai O, Glaser SJ, Haase A, Schwaiger M, Schulte RF. IDEAL spiral CSI for dynamic metabolic MR imaging of hyperpolarized [1-13C]pyruvate. Magn Reson Med 2012;68(1):8-16.

8. Reeder SB, Brittain JH, Grist TM, Yen YF. Least-squares chemical shift separation for (13)C metabolic imaging. J Magn Reson Imaging 2007;26(4):1145-1152.

9. Gordon JW, Niles DJ, Fain SB, Johnson KM. Joint spatial-spectral reconstruction and k-t spirals for accelerated 2D spatial/1D spectral imaging of C dynamics. Magn Reson Med 2013.

10. Reeder SB, Wen Z, Yu H, Pineda AR, Gold GE, Markl M, Pelc NJ. Multicoil Dixon chemical species separation with an iterative least-squares estimation method. Magn Reson Med 2004;51(1):35-45.

11. Pineda AR, Reeder SB, Wen Z, Pelc NJ. Cramer-Rao bounds for three-point decomposition of water and fat. Magn Reson Med 2005;54(3):625-635.

12. Lustig M, Donoho D, Pauly JM. Sparse MRI: The application of compressed sensing for rapid MR imaging. Magn Reson Med 2007;58(6):1182-1195.

13. Hu S, Lustig M, Chen AP, Crane J, Kerr A, Kelley DA, Hurd R, Kurhanewicz J, Nelson SJ, Pauly JM, Vigneron DB. Compressed sensing for resolution enhancement of hyperpolarized 13C flyback 3D-MRSI. J Magn Reson 2008;192(2):258-264.

14. Hu S, Lustig M, Balakrishnan A, Larson PE, Bok R, Kurhanewicz J, Nelson SJ, Goga A, Pauly JM, Vigneron DB. 3D compressed sensing for highly accelerated hyperpolarized (13)C MRSI with in vivo applications to transgenic mouse models of cancer. Magn Reson Med 2010;63(2):312-321.

15. Larson PE, Hu S, Lustig M, Kerr AB, Nelson SJ, Kurhanewicz J, Pauly JM, Vigneron DB. Fast dynamic 3D MR spectroscopic imaging with compressed sensing and multiband excitation pulses for hyperpolarized 13C studies. Magn Reson Med 2011;65(3):610-619.

16. Doneva M, Bornert P, Eggers H, Mertins A, Pauly J, Lustig M. Compressed sensing for chemical shift-based water-fat separation. Magn Reson Med 2010;64(6):1749-1759.

17. Sharma SD, Hu HH, Nayak KS. Accelerated water-fat imaging using restricted subspace field map estimation and compressed sensing. Magn Reson Med 2012;67(3):650-659.

18. Wiens CN, McCurdy CM, Willig-Onwuachi JD, McKenzie CA. R2*-corrected water-fat imaging using compressed sensing and parallel imaging. Magn Reson Med 2013.

19. Mayer D, Yen YF, Takahashi A, Josan S, Tropp J, Rutt BK, Hurd RE, Spielman DM, Pfefferbaum A. Dynamic and high-resolution metabolic imaging of hyperpolarized [1-13C]-pyruvate in the rat brain using a high-performance gradient insert. Magn Reson Med 2011;65(5):1228-1233.

20. Lim H, Thind K, Martinez-Santiesteban F, TJ. S. Transmit-only receive-only operation of a switch-tuned 13C-1H radiofrequency coil for improved in vivo 13C spectroscopy. In :Proceedings of 21st Annual Meeting of ISMRM, Salt Lake City, Utah 2013:4369.

21. Zhao L, Mulkern R, Tseng CH, Williamson D, Patz S, Kraft R, Walsworth RL, Jolesz FA, Albert MS. Gradient-Echo Imaging Considerations for Hyperpolarized 129Xe MR. J Magn Reson B 1996;113(2):179-183.

22. Santyr GE, Lam WW, Ouriadov A. Rapid and efficient mapping of regional ventilation in the rat lung using hyperpolarized 3He with Flip Angle Variation for Offset of RF and Relaxation (FAVOR). Magn Reson Med 2008;59(6):1304-1310.

23. Soliman AS, Yuan J, White JA, Peters TM, McKenzie CA. A convex relaxation approach to fat/water separation with minimum label description. Med Image Comput Comput Assist Interv 2012;15(Pt 2):519-526.

24. Buckheit J, Chen S, Donoho D, Johnstone I, Scargle J. About Wavelab. Wavelab software package version 0700, Technical Report. Stanford, CA: Department of Statistics,Standford University; 1995.

25. Mayer D, Yen YF, Tropp J, Pfefferbaum A, Hurd RE, Spielman DM. Application of subsecond spiral chemical shift imaging to real-time multislice metabolic imaging of the rat in vivo after injection of hyperpolarized 13C1-pyruvate. Magn Reson Med 2009;62(3):557-564.

26. Levin YS, Mayer D, Yen YF, Hurd RE, Spielman DM. Optimization of fast spiral chemical shift imaging using least squares reconstruction: application for hyperpolarized (13)C metabolic imaging. Magn Reson Med 2007;58(2):245-252.

27. Cunningham CH, Vigneron DB, Chen AP, Xu D, Nelson SJ, Hurd RE, Kelley DA, Pauly JM. Design of flyback echo-planar readout gradients for magnetic resonance spectroscopic imaging. Magn Reson Med 2005;54(5):1286-1289.

28. Dominguez-Viqueira W, Lau AZ, Chen AP, Cunningham CH. Multichannel receiver coils for improved coverage in cardiac metabolic imaging using prepolarized (13) C substrates. Magn Reson Med 2013;70(1):295-300.

29. Tropp J, Lupo JM, Chen A, Calderon P, McCune D, Grafendorfer T, Ozturk-Isik E, Larson PE, Hu S, Yen YF, Robb F, Bok R, Schulte R, Xu D, Hurd R, Vigneron D, Nelson S. Multi-channel metabolic imaging, with SENSE reconstruction, of hyperpolarized [1-(13)C] pyruvate in a live rat at 3.0 tesla on a clinical MR scanner. J Magn Reson 2011;208(1):171-177.

30. Sharma SD, Hu HH, Nayak KS. Chemical shift encoded water-fat separation using parallel imaging and compressed sensing. Magn Reson Med 2013;69(2):456-466.

31. Lee RF, Johnson G, Grossman RI, Stoeckel B, Trampel R, McGuinness G. Advantages of parallel imaging in conjunction with hyperpolarized helium--a new approach to MRI of the lung. Magn Reson Med 2006;55(5):1132-1141.

32. Cunningham CH, Chen AP, Lustig M, Hargreaves BA, Lupo J, Xu D, Kurhanewicz J, Hurd RE, Pauly JM, Nelson SJ, Vigneron DB. Pulse sequence for dynamic volumetric imaging of hyperpolarized metabolic products. J Magn Reson 2008;193(1):139-146.

33. Chen AP, Hurd RE, Schroeder MA, Lau AZ, Gu YP, Lam WW, Barry J, Tropp J, Cunningham CH. Simultaneous investigation of cardiac pyruvate dehydrogenase flux, Krebs cycle metabolism and pH, using hyperpolarized [1,2-(13)C2]pyruvate in vivo. NMR Biomed 2012;25(2):305-311.

34. Schroeder MA, Atherton HJ, Ball DR, Cole MA, Heather LC, Griffin JL, Clarke K, Radda GK, Tyler DJ. Real-time assessment of Krebs cycle metabolism using hyperpolarized 13C magnetic resonance spectroscopy. Faseb J 2009;23(8):2529-2538.

Chapter 5

5 Conclusions and Future Work

5.1 Thesis Summary

Chemical shift imaging is a powerful technique that allows separation of signals due to different chemical species. Encoding MR images in the chemical shift dimension results in long acquisition times. These long acquisition times often limit the resolution and spatial coverage. This thesis examines the role that image acceleration techniques can play in chemical shift imaging. A method to measure the signal-to-noise ratio of parallel imaging reconstructions was described. New algorithms for accelerated chemical shift imaging in the fields of water-fat imaging and metabolite separation of hyperpolarized [1-^{13}C] pyruvate were proposed.

Chapter 2 described the validation of a new method referred to as the generalized pseudo-replica method for measuring the signal-to-noise ratio of parallel imaging reconstructions. In the generalized pseudo-replica method, synthesized correlated Gaussian noise was repeatedly added to undersampled k-space data and parallel imaging reconstructions were performed. The resulting reconstructions produce a set of replica images in which the signal in each replica is the same while the noise is different. Subtraction of the original image where no synthetic noise was added results in a set of noise-only images. From the noise-only images pixel-wise estimates of the noise can be made with a 4D moving standard deviation calculation (3 spatial dimensions, 1 replica dimension).

The generalized pseudo-replica method was compared to existing SNR techniques using phantom and *in vivo* experiments. At low and moderate acceleration factors, accurate SNR measurements were estimated through the image volume. At high acceleration factors, locally biased estimates appeared at the edge of regions with high g-factors. An assumption made in the technique was that noise within the volume of interest is uncorrelated. At high acceleration factors, this assumption began to fail as the g-factor within a VOI could vary significantly, resulting in a locally biased estimate of SNR.

The generalized pseudo-replica method offers a trade-off between computational efficiency and spatial resolution of the noise map. In most applications, SNR measurements are made by taking the average SNR over particular region of interest. In such cases, a full resolution noise map is not necessary and this loss of resolution is acceptable.

Chapters 3 described an approach to water-fat imaging with R_2^* correction using compressed sensing and parallel imaging acceleration. In this approach, water-fat imaging, compressed sensing, and parallel imaging were integrated together, allowing the reconstruction of water-fat images from highly undersampled datasets from the liver, calf, knee, and abdominal cavity. Acceleration factors as high as 7.0 were shown with excellent image quality.

This water-fat imaging approach was demonstrated using a customized IDEAL-SPGR pulse sequence capable of arbitrary undersampling patterns. In this pulse sequence small y and z gradients were applied during the frequency rewinder, allowing sampling of each echo with different undersampling patterns. Sampling each echo differently improved incoherence, a necessary component to compressed sensing reconstructions. It was also shown that at high acceleration factors this improved incoherence results in improved reconstruction fidelity.

R_2^* decay is one of the confounding factors that must be corrected for quantitative measurement of the PDFF (1). This method estimated R_2^* making quantitative measurements possible. Measurements of R_2^* and PDFF using the proposed technique were compared to a fully sampled reference images to ensure agreement.

The proposed method was compared to the current gold standard acceleration technique (sequential parallel imaging and water-fat separation). At high accelerations, noise amplification due to high g-factors caused the sequential parallel imaging and water-fat separation technique to fail. The proposed technique performed well allowing accurate PDFF measurements in liver, spine, and subcutaneous fat.

Multi-echo, multi-channel 3D datasets are large and presented challenges in terms of memory constraints and reconstruction times. To help alleviate these problems, coil compression was introduced. It was shown that 32 coil datasets could be compressed into 8 virtual-coil datasets without any noticeable degradation of image quality. This resulted in a fourfold reduction in reconstruction times.

Chapter 4 described an approach to separation of hyperpolarized [1-^{13}C] pyruvate and its metabolites. In this approach signal from pyruvate, alanine, lactate, and bicarbonate was separated after injection of hyperpolarized [1-^{13}C] pyruvate. Compressed sensing and high performance insert gradients were used to accelerate image acquisitions. The approach was validated using digital phantoms and demonstrated in dynamic, 3D *in vivo* experiments.

The small gyromagnetic ratio of ^{13}C made field map estimation an easier problem in ^{13}C imaging. For a small field-of-view, the field can be assumed to be homogeneous provided that care is taken when shimming. However, shimming is difficult when high performance gradients are used, resulting in non-homogeneous field maps. In such a case, a homogenous field should not be assumed. In the approach I presented, the field map is broken into two components, a spatial varying component and offset term. The spatial varying component was measured using proton imaging while the offset term, which describes the difference between the carrier frequency and resonance of pyruvate, was estimated by enforcing consistency of the data with the signal model.

Image acquisitions were accelerated using two synergistic approaches. First, images were accelerated through the use of a compressed sensing reconstruction. In this approach, metabolite maps and the field map offset term were estimated directly from the undersampled k-space. Second, high performance gradients designed for small animal imaging was used to accelerate image acquisitions. The combination of both is a topic that will be examined in the future and should allow the acquisition of 3D images in approximately 1s, resulting in a nine-fold reduction in acquisition time. In addition to reducing the acquisition time, accelerated hyperpolarized imaging reduces the number of radiofrequency excitations required to resolve metabolic maps. In the context of a hyperpolarized experiment this mean that a larger portion of the hyperpolarized signal can be used by each excitation (i.e. a higher flip angle can be used).

5.2 Future Work

5.2.1 Image Quality Metrics for Compressed Sensing

The gold standard for image quality for any diagnostic imaging technique is visual inspection. Can the radiologist make the diagnosis of the disease based on the image? However, this method is not perfectly reproducible and may not be practical for large clinical studies. As an alternative, quantitative image quality metrics have been proposed as an objective method to characterize the diagnostic value of a reconstruction.

The quality of an image can be described by its noise properties and image artifact. For parallel imaging, noise properties and image artifact are well defined. Techniques such as the one proposed in Chapter 2 have been described to quantify the noise properties of a parallel imaging reconstruction (3-7). Point spread function based metrics have been proposed to describe artifact in parallel imaging reconstruction (8,9).

Unlike parallel imaging, the question of quantitative image metrics for compressed sensing reconstructions is still open. Classical image quality metrics such as SNR and artifact estimation rely on the image system being linear and shift-invariant (10-12). In compressed sensing these assumptions break down, making most existing image quality metrics inapplicable to compressed sensing.

Currently compressed sensing techniques typically assess image quality using difference images or root mean square error. These metrics do not necessarily correlate well with the diagnostic quality of an image (13,14). To illustrate this, consider the detectability of low contrast objects. Loss of low contrast objects is a common artifact in over-accelerated compressed sensing reconstructions. This is problematic because important structures, such as lesions, can disappear from an image (15). Because these artifacts are low contrast, the resulting difference images or root mean square error could be low indicating a diagnostic quality image when in fact a diagnostically important feature in missing.

The non-linearity of compressed sensing reconstructions makes the SNR techniques described in Chapter 2 not applicable to the reconstructions proposed in Chapter 3 and 4. Currently, case-by-case evaluation of images by a radiologist is being used to characterize image quality of compressed sensing reconstruction (16,17). Development of image quality metrics that accurately reflect their diagnostic quality would certainly be useful both in assessing all compressed sensing reconstructions including those proposed in Chapters 3 and 4.

5.2.2 Clinically Feasibility of Accelerated Water-Fat Imaging

The ultimate goal of any technique is use in clinical and pre-clinical settings. Lengthy reconstruction times are still a major limitation to clinical applicability of the technique proposed in Chapter 3. To help reduce computational requirements and improve reconstruction times, coil compression was implemented (18). 32 coil datasets were compressed into 8 virtual-coil datasets resulting in a reduction in reconstruction times of a factor of 4. While this is a good first step, further improvements in reconstruction times are required before clinical implementation of this technique is feasible. GPU implementations of compressed sensing algorithm have been to shown to improve reconstruction times (19,20). In addition, alternative faster compressed sensing algorithms should be examined to improve reconstructions times (21).

5.2.3 Applications of Chemical Shift Imaging to Hyperpolarized Imaging

In Chapter 4, the use of chemical shift imaging was examined for hyperpolarized [1-^{13}C] pyruvate metabolic imaging. The following section discusses two other opportunities for chemical shift imaging in the field of hyperpolarized imaging: mapping of gas transport in lungs using hyperpolarized ^{129}Xe (22) and mapping of cell necrosis and treatment response in tumors using hyperpolarized [1,4-$^{13}C_2$]fumarate (23).

Hyperpolarized noble gases such as ^{129}Xe have been used to evaluate the structure and function of the lungs (24). Upon inhalation ^{129}Xe diffuses out of the alveolar air space, through the lung parenchyma and into the blood. These components exhibit different chemical shifts: alveolar air space (0ppm), lung parenchyma (198ppm), and blood

(218ppm) (25). Chemical shift imaging techniques similar to the one proposed in Chapter 4 were recently proposed to measure gas uptake by blood and tissue (8,22,26). Using a spectrally selective excitation, the signal from just the lung parenchyma and blood signal could be excited and using reconstructions like the one proposed in Chapter 4, separation of the signal from lung parenchyma and blood could be achieved. Separating these signals could allow regional measurements of lung function parameters like gas exchange and perfusion, with applications to the early detection and staging of diseases like asthma or chronic obstructive pulmonary disease (COPD).

The use of hyperpolarized ^{13}C contrast agents as potential imaging biomarkers for the detection and treatment response of cancer has garnered much attention. Primarily, [1-^{13}C] pyruvate and its conversion to lactate have been used as a potential biomarker (27,28). The use of alternative substrates such as [1,4-$^{13}C_2$] fumarate is also being explored (23). Fumarate, a citric acid cycle component, is converted to malate in the mitochondria by the enzyme fumarase. Under normal cells conditions, transportation of fumarate into the mitochondria is slow, and the conversion of fumarate into malate cannot be seen within the lifetime of the hyperpolarized [1,4-$^{13}C_2$] fumarate (23,29). In necrotic cells, membranes of cells and organelles like the mitochondria are disrupted, and the conversion of fumarate (175.4ppm) into malate (180.6ppm and 181.8ppm) is much faster and can be seen (23). Separation of the signals from fumarate and malate using the proposed 3D chemical shift imaging technique could allow regional measurements of cell necrosis with applications in treatment response in tumors.

5.3 References

1. Reeder SB, Hu HH, Sirlin CB. Proton density fat-fraction: a standardized MR-based biomarker of tissue fat concentration. J Magn Reson Imaging 2012;36(5):1011-1014.

2. Lee RF, Johnson G, Grossman RI, Stoeckel B, Trampel R, McGuinness G. Advantages of parallel imaging in conjunction with hyperpolarized helium--a new approach to MRI of the lung. Magn Reson Med 2006;55(5):1132-1141.

3. Dietrich O, Raya JG, Reeder SB, Reiser MF, Schoenberg SO. Measurement of signal-to-noise ratios in MR images: influence of multichannel coils, parallel imaging, and reconstruction filters. J Magn Reson Imaging 2007;26(2):375-385.

4. Kellman P, McVeigh ER. Image reconstruction in SNR units: a general method for SNR measurement. Magn Reson Med 2005;54(6):1439-1447.

5. Reeder SB, Wintersperger BJ, Dietrich O, Lanz T, Greiser A, Reiser MF, Glazer GM, Schoenberg SO. Practical approaches to the evaluation of signal-to-noise ratio performance with parallel imaging: application with cardiac imaging and a 32-channel cardiac coil. Magn Reson Med 2005;54(3):748-754.

6. Robson PM, Grant AK, Madhuranthakam AJ, Lattanzi R, Sodickson DK, McKenzie CA. Comprehensive quantification of signal-to-noise ratio and g-factor for image-based and k-space-based parallel imaging reconstructions. Magn Reson Med 2008;60(4):895-907.

7. NEMA. Determination of signal-to-noise ratio (SNR) in diagnostic magnetic resonance imaging. Rosslyn, VA; 2001.

8. Yang L. Point Spread Function Based Quantification of Artefact in Parallel Imaging. London: University of Western Ontario; 2010.

9. Li Y, Huang F, Lin W, Reykowski A. A Mathetmatical Model Toward Quantitative Assessment of Parallel Imaging Reconstruction. Proceedings of the 18th Annual Meeting of ISMRM, Stockholm, Sweden 2010;2010.

10. Wech T, Stab D, Budich JC, Fischer A, Tran-Gia J, Hahn D, Kostler H. Resolution evaluation of MR images reconstructed by iterative thresholding algorithms for compressed sensing. Med Phys 2012;39(7):4328-4338.

11. Steckner MC, Drost DJ, Prato FS. Computing the modulation transfer function of a magnetic resonance imager. Med Phys 1994;21(3):483-489.

12. Dragonu I, Guobin L, Snyder J, Hennig J, Zaitsev M. Determination of the Point Spread Function for Compressed Sensing Reconstruction. Proceedings of the 18th Annual Meeting of ISMRM, Stockholm, Sweden 2010:2272.

13. Trzasko JD, Bao Z, Manduca A, McGee KP, Bernstein MA. Sparsity and low-contrast object detectability. Magn Reson Med 2012;67(4):1022-1032.

14. Wang Z, Bovik AC, Sheikh HR, Simoncelli EP. Image quality assessment: from error visibility to structural similarity. IEEE Trans Image Process 2004;13(4):600-612.

15. Lustig M, Donoho D, Pauly JM. Sparse MRI: The application of compressed sensing for rapid MR imaging. Magn Reson Med 2007;58(6):1182-1195.

16. Vasanawala SS, Alley MT, Hargreaves BA, Barth RA, Pauly JM, Lustig M. Improved pediatric MR imaging with compressed sensing. Radiology 2010;256(2):607-616.

17. Sharma SD, Fong CL, Tzung B, Law M, Nayak KS. Clinical Image Quality Assessment of CS-Reconstructed Brain Images. Proceedings of the 18th Annual Meeting of ISMRM, Stockholm, Sweden 2010:4874.

18. Zhang T, Pauly JM, Vasanawala SS, Lustig M. Coil compression for accelerated imaging with Cartesian sampling. Magn Reson Med 2013;69(2):571-582.

19. Murphy M, Alley M, Demmel J, Keutzer K, Vasanawala S, Lustig M. Fast l(1)-SPIRiT compressed sensing parallel imaging MRI: scalable parallel implementation and clinically feasible runtime. IEEE Trans Med Imaging 2012;31(6):1250-1262.

20. Smith DS, Gore JC, Yankeelov TE, Welch EB. Real-Time Compressive Sensing MRI Reconstruction Using GPU Computing and Split Bregman Methods. Int J Biomed Imaging 2012;2012:864827.

21. Goldstein T, Osher S. The Split Bregman Method for L1-Regularized Problems. Siam J Imaging Sci 2009;2(2):323-343.

22. Qing K, Ruppert K, Jiang Y, Mata JF, Miller GW, Shim YM, Wang C, Ruset IC, Hersman FW, Altes TA, Mugler JP, 3rd. Regional mapping of gas uptake by blood and tissue in the human lung using hyperpolarized xenon-129 MRI. J Magn Reson Imaging 2013.

23. Gallagher FA, Kettunen MI, Hu DE, Jensen PR, Zandt RI, Karlsson M, Gisselsson A, Nelson SK, Witney TH, Bohndiek SE, Hansson G, Peitersen T, Lerche MH, Brindle KM. Production of hyperpolarized [1,4-13C2]malate from [1,4-13C2]fumarate is a marker of cell necrosis and treatment response in tumors. Proc Natl Acad Sci U S A 2009;106(47):19801-19806.

24. Mugler JP, Altes TA. Hyperpolarized 129Xe MRI of the human lung. Journal of Magnetic Resonance Imaging 2013;37(2):313-331.

25. Wagshul ME, Button TM, Li HF, Liang Z, Springer CS, Zhong K, Wishnia A. In vivo MR imaging and spectroscopy using hyperpolarized 129Xe. Magn Reson Med 1996;36(2):183-191.

26. Ouriadov AV, Fox MS, Friesen-Waldner LJ, McKenzie CA. Hyperpolarized 129Xe Gas & Dissolved Phse Lung Imaging using IDEAL. Proceedings of the 19th Annual Meeting of ISMRM, Montreal, Canada 2011:886.

27. Albers MJ, Bok R, Chen AP, Cunningham CH, Zierhut ML, Zhang VY, Kohler SJ, Tropp J, Hurd RE, Yen YF, Nelson SJ, Vigneron DB, Kurhanewicz J. Hyperpolarized 13C lactate, pyruvate, and alanine: noninvasive biomarkers for prostate cancer detection and grading. Cancer Res 2008;68(20):8607-8615.

28. Golman K, Zandt RI, Lerche M, Pehrson R, Ardenkjaer-Larsen JH. Metabolic imaging by hyperpolarized 13C magnetic resonance imaging for in vivo tumor diagnosis. Cancer Res 2006;66(22):10855-10860.

29. Kurhanewicz J, Vigneron DB, Brindle K, Chekmenev EY, Comment A, Cunningham CH, Deberardinis RJ, Green GG, Leach MO, Rajan SS, Rizi RR, Ross BD, Warren WS, Malloy CR. Analysis of cancer metabolism by imaging hyperpolarized nuclei: prospects for translation to clinical research. Neoplasia 2011;13(2):81-97.

Ethics Approval

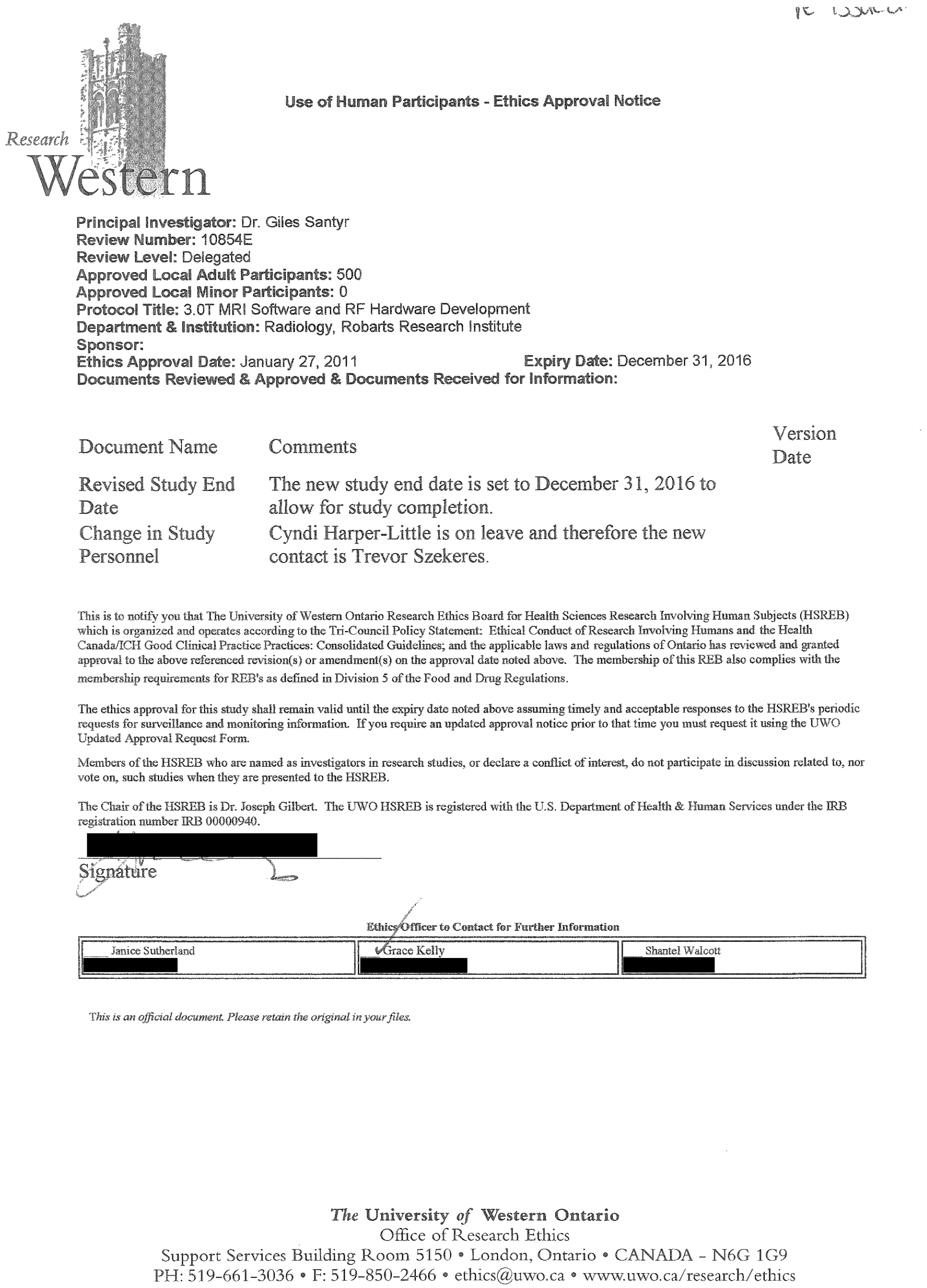

re issue

Research Western

Use of Human Participants - Ethics Approval Notice

Principal Investigator: Dr. Giles Santyr
Review Number: 10854E
Review Level: Delegated
Approved Local Adult Participants: 500
Approved Local Minor Participants: 0
Protocol Title: 3.0T MRI Software and RF Hardware Development
Department & Institution: Radiology, Robarts Research Institute
Sponsor:
Ethics Approval Date: January 27, 2011 **Expiry Date:** December 31, 2016
Documents Reviewed & Approved & Documents Received for Information:

Document Name	Comments	Version Date
Revised Study End Date	The new study end date is set to December 31, 2016 to allow for study completion.	
Change in Study Personnel	Cyndi Harper-Little is on leave and therefore the new contact is Trevor Szekeres.	

This is to notify you that The University of Western Ontario Research Ethics Board for Health Sciences Research Involving Human Subjects (HSREB) which is organized and operates according to the Tri-Council Policy Statement: Ethical Conduct of Research Involving Humans and the Health Canada/ICH Good Clinical Practice Practices: Consolidated Guidelines; and the applicable laws and regulations of Ontario has reviewed and granted approval to the above referenced revision(s) or amendment(s) on the approval date noted above. The membership of this REB also complies with the membership requirements for REB's as defined in Division 5 of the Food and Drug Regulations.

The ethics approval for this study shall remain valid until the expiry date noted above assuming timely and acceptable responses to the HSREB's periodic requests for surveillance and monitoring information. If you require an updated approval notice prior to that time you must request it using the UWO Updated Approval Request Form.

Members of the HSREB who are named as investigators in research studies, or declare a conflict of interest, do not participate in discussion related to, nor vote on, such studies when they are presented to the HSREB.

The Chair of the HSREB is Dr. Joseph Gilbert. The UWO HSREB is registered with the U.S. Department of Health & Human Services under the IRB registration number IRB 00000940.

[redacted]

Signature

Ethics Officer to Contact for Further Information

___ Janice Sutherland [redacted]	✓Grace Kelly [redacted]	___ Shantel Walcott [redacted]

This is an official document. Please retain the original in your files.

The **University** *of* **Western Ontario**
Office of Research Ethics
Support Services Building Room 5150 • London, Ontario • CANADA - N6G 1G9
PH: 519-661-3036 • F: 519-850-2466 • ethics@uwo.ca • www.uwo.ca/research/ethics

Western

AUP Number: 2009-005
PI Name: Mckenzie, Charles
AUP Title: Validation Of Accelerated Hyperpolarized C13 Ideal Mri

Approval Date: 05/14/2013

Official Notice of Animal Use Subcommittee (AUS) Approval: Your new Animal Use Protocol (AUP) entitled "Validation Of Accelerated Hyperpolarized C13 Ideal Mri

" has been APPROVED by the Animal Use Subcommittee of the University Council on Animal Care. This approval, although valid for four years, and is subject to annual Protocol Renewal.2009-005::5

1. This AUP number must be indicated when ordering animals for this project.
2. Animals for other projects may not be ordered under this AUP number.
3. Purchases of animals other than through this system must be cleared through the ACVS office. Health certificates will be required.

The holder of this Animal Use Protocol is responsible to ensure that all associated safety components (biosafety, radiation safety, general laboratory safety) comply with institutional safety standards and have received all necessary approvals. Please consult directly with your institutional safety officers.

Submitted by: Copeman, Laura
on behalf of the Animal Use Subcommittee
University Council on Animal Care

[redacted]

Letters of Permission

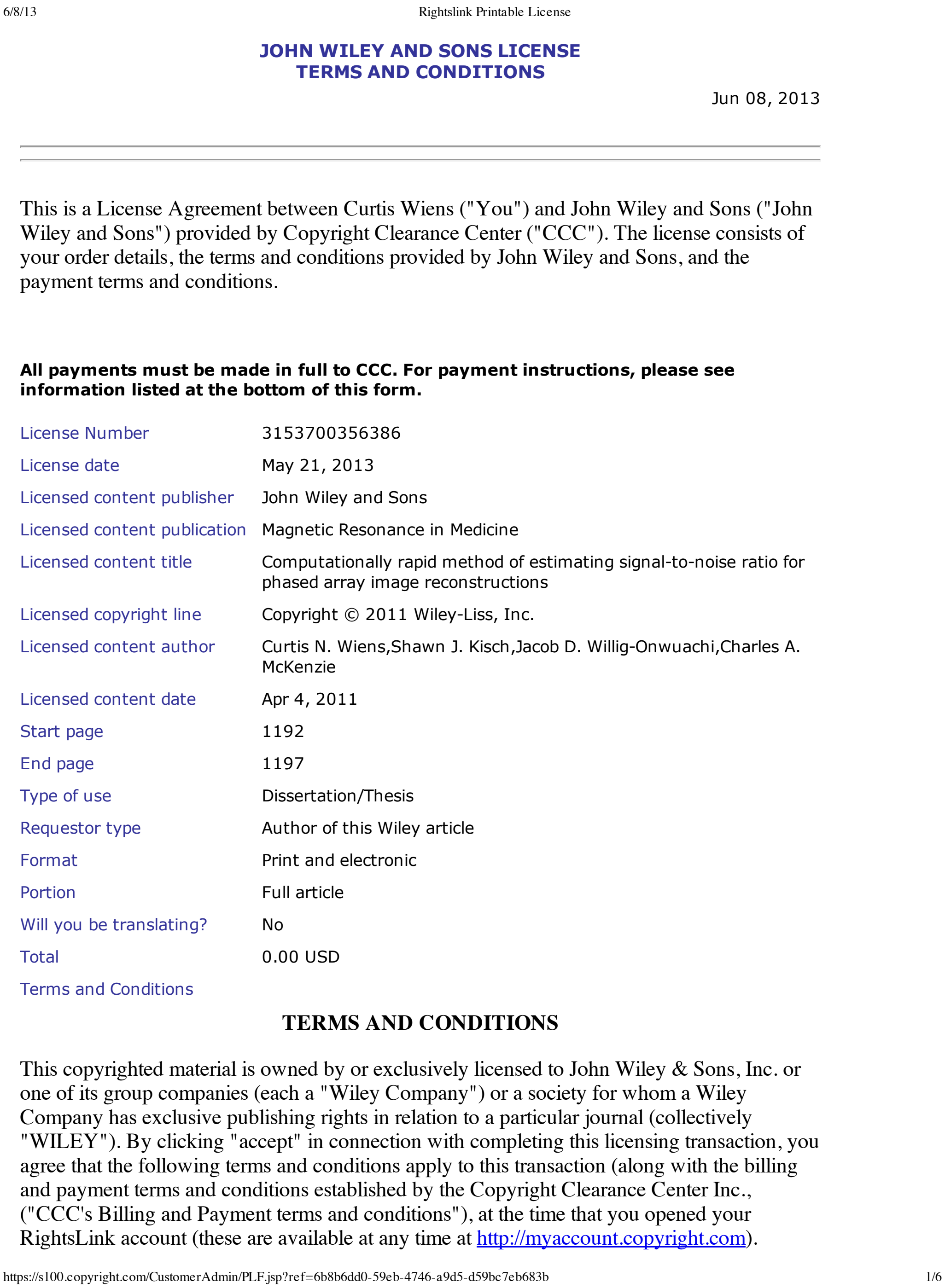

JOHN WILEY AND SONS LICENSE TERMS AND CONDITIONS

Jun 08, 2013

This is a License Agreement between Curtis Wiens ("You") and John Wiley and Sons ("John Wiley and Sons") provided by Copyright Clearance Center ("CCC"). The license consists of your order details, the terms and conditions provided by John Wiley and Sons, and the payment terms and conditions.

All payments must be made in full to CCC. For payment instructions, please see information listed at the bottom of this form.

License Number	3153700356386
License date	May 21, 2013
Licensed content publisher	John Wiley and Sons
Licensed content publication	Magnetic Resonance in Medicine
Licensed content title	Computationally rapid method of estimating signal-to-noise ratio for phased array image reconstructions
Licensed copyright line	Copyright © 2011 Wiley-Liss, Inc.
Licensed content author	Curtis N. Wiens,Shawn J. Kisch,Jacob D. Willig-Onwuachi,Charles A. McKenzie
Licensed content date	Apr 4, 2011
Start page	1192
End page	1197
Type of use	Dissertation/Thesis
Requestor type	Author of this Wiley article
Format	Print and electronic
Portion	Full article
Will you be translating?	No
Total	0.00 USD
Terms and Conditions	

TERMS AND CONDITIONS

This copyrighted material is owned by or exclusively licensed to John Wiley & Sons, Inc. or one of its group companies (each a "Wiley Company") or a society for whom a Wiley Company has exclusive publishing rights in relation to a particular journal (collectively "WILEY"). By clicking "accept" in connection with completing this licensing transaction, you agree that the following terms and conditions apply to this transaction (along with the billing and payment terms and conditions established by the Copyright Clearance Center Inc., ("CCC's Billing and Payment terms and conditions"), at the time that you opened your RightsLink account (these are available at any time at http://myaccount.copyright.com).

Terms and Conditions

1. The materials you have requested permission to reproduce (the "Materials") are protected by copyright.

2.You are hereby granted a personal, non-exclusive, non-sublicensable, non-transferable, worldwide, limited license to reproduce the Materials for the purpose specified in the licensing process. This license is for a one-time use only with a maximum distribution equal to the number that you identified in the licensing process. Any form of republication granted by this license must be completed within two years of the date of the grant of this license (although copies prepared before may be distributed thereafter). The Materials shall not be used in any other manner or for any other purpose. Permission is granted subject to an appropriate acknowledgement given to the author, title of the material/book/journal and the publisher. You shall also duplicate the copyright notice that appears in the Wiley publication in your use of the Material. Permission is also granted on the understanding that nowhere in the text is a previously published source acknowledged for all or part of this Material. Any third party material is expressly excluded from this permission.

3. With respect to the Materials, all rights are reserved. Except as expressly granted by the terms of the license, no part of the Materials may be copied, modified, adapted (except for minor reformatting required by the new Publication), translated, reproduced, transferred or distributed, in any form or by any means, and no derivative works may be made based on the Materials without the prior permission of the respective copyright owner. You may not alter, remove or suppress in any manner any copyright, trademark or other notices displayed by the Materials. You may not license, rent, sell, loan, lease, pledge, offer as security, transfer or assign the Materials, or any of the rights granted to you hereunder to any other person.

4. The Materials and all of the intellectual property rights therein shall at all times remain the exclusive property of John Wiley & Sons Inc or one of its related companies (WILEY) or their respective licensors, and your interest therein is only that of having possession of and the right to reproduce the Materials pursuant to Section 2 herein during the continuance of this Agreement. You agree that you own no right, title or interest in or to the Materials or any of the intellectual property rights therein. You shall have no rights hereunder other than the license as provided for above in Section 2. No right, license or interest to any trademark, trade name, service mark or other branding ("Marks") of WILEY or its licensors is granted hereunder, and you agree that you shall not assert any such right, license or interest with respect thereto.

5. NEITHER WILEY NOR ITS LICENSORS MAKES ANY WARRANTY OR REPRESENTATION OF ANY KIND TO YOU OR ANY THIRD PARTY, EXPRESS, IMPLIED OR STATUTORY, WITH RESPECT TO THE MATERIALS OR THE ACCURACY OF ANY INFORMATION CONTAINED IN THE MATERIALS, INCLUDING, WITHOUT LIMITATION, ANY IMPLIED WARRANTY OF MERCHANTABILITY, ACCURACY, SATISFACTORY QUALITY, FITNESS FOR A PARTICULAR PURPOSE, USABILITY, INTEGRATION OR NON-INFRINGEMENT AND ALL SUCH WARRANTIES ARE HEREBY EXCLUDED BY WILEY AND ITS LICENSORS AND WAIVED BY YOU.

6. WILEY shall have the right to terminate this Agreement immediately upon breach of this

Agreement by you.

7. You shall indemnify, defend and hold harmless WILEY, its Licensors and their respective directors, officers, agents and employees, from and against any actual or threatened claims, demands, causes of action or proceedings arising from any breach of this Agreement by you.

8. IN NO EVENT SHALL WILEY OR ITS LICENSORS BE LIABLE TO YOU OR ANY OTHER PARTY OR ANY OTHER PERSON OR ENTITY FOR ANY SPECIAL, CONSEQUENTIAL, INCIDENTAL, INDIRECT, EXEMPLARY OR PUNITIVE DAMAGES, HOWEVER CAUSED, ARISING OUT OF OR IN CONNECTION WITH THE DOWNLOADING, PROVISIONING, VIEWING OR USE OF THE MATERIALS REGARDLESS OF THE FORM OF ACTION, WHETHER FOR BREACH OF CONTRACT, BREACH OF WARRANTY, TORT, NEGLIGENCE, INFRINGEMENT OR OTHERWISE (INCLUDING, WITHOUT LIMITATION, DAMAGES BASED ON LOSS OF PROFITS, DATA, FILES, USE, BUSINESS OPPORTUNITY OR CLAIMS OF THIRD PARTIES), AND WHETHER OR NOT THE PARTY HAS BEEN ADVISED OF THE POSSIBILITY OF SUCH DAMAGES. THIS LIMITATION SHALL APPLY NOTWITHSTANDING ANY FAILURE OF ESSENTIAL PURPOSE OF ANY LIMITED REMEDY PROVIDED HEREIN.

9. Should any provision of this Agreement be held by a court of competent jurisdiction to be illegal, invalid, or unenforceable, that provision shall be deemed amended to achieve as nearly as possible the same economic effect as the original provision, and the legality, validity and enforceability of the remaining provisions of this Agreement shall not be affected or impaired thereby.

10. The failure of either party to enforce any term or condition of this Agreement shall not constitute a waiver of either party's right to enforce each and every term and condition of this Agreement. No breach under this agreement shall be deemed waived or excused by either party unless such waiver or consent is in writing signed by the party granting such waiver or consent. The waiver by or consent of a party to a breach of any provision of this Agreement shall not operate or be construed as a waiver of or consent to any other or subsequent breach by such other party.

11. This Agreement may not be assigned (including by operation of law or otherwise) by you without WILEY's prior written consent.

12. Any fee required for this permission shall be non-refundable after thirty (30) days from receipt

13. These terms and conditions together with CCC's Billing and Payment terms and conditions (which are incorporated herein) form the entire agreement between you and WILEY concerning this licensing transaction and (in the absence of fraud) supersedes all prior agreements and representations of the parties, oral or written. This Agreement may not be amended except in writing signed by both parties. This Agreement shall be binding upon and inure to the benefit of the parties' successors, legal representatives, and authorized assigns.

14. In the event of any conflict between your obligations established by these terms and conditions and those established by CCC's Billing and Payment terms and conditions, these terms and conditions shall prevail.

15. WILEY expressly reserves all rights not specifically granted in the combination of (i) the

license details provided by you and accepted in the course of this licensing transaction, (ii) these terms and conditions and (iii) CCC's Billing and Payment terms and conditions.

16. This Agreement will be void if the Type of Use, Format, Circulation, or Requestor Type was misrepresented during the licensing process.

17. This Agreement shall be governed by and construed in accordance with the laws of the State of New York, USA, without regards to such state's conflict of law rules. Any legal action, suit or proceeding arising out of or relating to these Terms and Conditions or the breach thereof shall be instituted in a court of competent jurisdiction in New York County in the State of New York in the United States of America and each party hereby consents and submits to the personal jurisdiction of such court, waives any objection to venue in such court and consents to service of process by registered or certified mail, return receipt requested, at the last known address of such party.

Wiley Open Access Terms and Conditions

Wiley publishes Open Access articles in both its Wiley Open Access Journals program [http://www.wileyopenaccess.com/view/index.html] and as Online Open articles in its subscription journals. The majority of Wiley Open Access Journals have adopted the Creative Commons Attribution License (CC BY) which permits the unrestricted use, distribution, reproduction, adaptation and commercial exploitation of the article in any medium. No permission is required to use the article in this way provided that the article is properly cited and other license terms are observed. A small number of Wiley Open Access journals have retained the Creative Commons Attribution Non Commercial License (CC BY-NC), which permits use, distribution and reproduction in any medium, provided the original work is properly cited and is not used for commercial purposes.

Online Open articles - Authors selecting Online Open are, unless particular exceptions apply, offered a choice of Creative Commons licenses. They may therefore select from the CC BY, the CC BY-NC and the Attribution-NoDerivatives (CC BY-NC-ND). The CC BY-NC-ND is more restrictive than the CC BY-NC as it does not permit adaptations or modifications without rights holder consent.

Wiley Open Access articles are protected by copyright and are posted to repositories and websites in accordance with the terms of the applicable Creative Commons license referenced on the article. At the time of deposit, Wiley Open Access articles include all changes made during peer review, copyediting, and publishing. Repositories and websites that host the article are responsible for incorporating any publisher-supplied amendments or retractions issued subsequently.
Wiley Open Access articles are also available without charge on Wiley's publishing platform, **Wiley Online Library** or any successor sites.

Conditions applicable to all Wiley Open Access articles:

- The authors' moral rights must not be compromised. These rights include the right of "paternity" (also known as "attribution" - the right for the author to be identified as such) and "integrity" (the right for the author not to have the work altered in such a way that the author's reputation or integrity may be damaged).
- Where content in the article is identified as belonging to a third party, it is the obligation

of the user to ensure that any reuse complies with the copyright policies of the owner of that content.

- If article content is copied, downloaded or otherwise reused for research and other purposes as permitted, a link to the appropriate bibliographic citation (authors, journal, article title, volume, issue, page numbers, DOI and the link to the definitive published version on Wiley Online Library) should be maintained. Copyright notices and disclaimers must not be deleted.
    - Creative Commons licenses are copyright licenses and do not confer any other rights, including but not limited to trademark or patent rights.

- Any translations, for which a prior translation agreement with Wiley has not been agreed, must prominently display the statement: "This is an unofficial translation of an article that appeared in a Wiley publication. The publisher has not endorsed this translation."

Conditions applicable to non-commercial licenses (CC BY-NC and CC BY-NC-ND)

For non-commercial and non-promotional purposes individual non-commercial users may access, download, copy, display and redistribute to colleagues Wiley Open Access articles. In addition, articles adopting the CC BY-NC may be adapted, translated, and text- and data-mined subject to the conditions above.

Use by commercial "for-profit" organizations

Use of non-commercial Wiley Open Access articles for commercial, promotional, or marketing purposes requires further explicit permission from Wiley and will be subject to a fee. Commercial purposes include:

- Copying or downloading of articles, or linking to such articles for further redistribution, sale or licensing;

- Copying, downloading or posting by a site or service that incorporates advertising with such content;

- The inclusion or incorporation of article content in other works or services (other than normal quotations with an appropriate citation) that is then available for sale or licensing, for a fee (for example, a compilation produced for marketing purposes, inclusion in a sales pack)

- Use of article content (other than normal quotations with appropriate citation) by for-profit organizations for promotional purposes

- Linking to article content in e-mails redistributed for promotional, marketing or educational purposes;

- Use for the purposes of monetary reward by means of sale, resale, license, loan, transfer or other form of commercial exploitation such as marketing products

- Print reprints of Wiley Open Access articles can be purchased from: corporatesales@wiley.com

The modification or adaptation for any purpose of an article referencing the CC BY-NC-ND License requires consent which can be requested from RightsLink@wiley.com .

Other Terms and Conditions:

BY CLICKING ON THE "I AGREE..." BOX, YOU ACKNOWLEDGE THAT YOU HAVE READ AND FULLY UNDERSTAND EACH OF THE SECTIONS OF AND PROVISIONS SET FORTH IN THIS AGREEMENT AND THAT YOU ARE IN AGREEMENT WITH AND ARE WILLING TO ACCEPT ALL OF YOUR OBLIGATIONS AS SET FORTH IN THIS AGREEMENT.

v1.8

If you would like to pay for this license now, please remit this license along with your payment made payable to "COPYRIGHT CLEARANCE CENTER" otherwise you will be invoiced within 48 hours of the license date. Payment should be in the form of a check or money order referencing your account number and this invoice number RLNK501025938.
Once you receive your invoice for this order, you may pay your invoice by credit card. Please follow instructions provided at that time.

Make Payment To:
Copyright Clearance Center
Dept 001
P.O. Box 843006
Boston, MA 02284-3006

For suggestions or comments regarding this order, contact RightsLink Customer Support: customercare@copyright.com or +1-877-622-5543 (toll free in the US) or +1-978-646-2777.

Gratis licenses (referencing $0 in the Total field) are free. Please retain this printable license for your reference. No payment is required.

JOHN WILEY AND SONS LICENSE TERMS AND CONDITIONS

Jun 08, 2013

This is a License Agreement between Curtis Wiens ("You") and John Wiley and Sons ("John Wiley and Sons") provided by Copyright Clearance Center ("CCC"). The license consists of your order details, the terms and conditions provided by John Wiley and Sons, and the payment terms and conditions.

All payments must be made in full to CCC. For payment instructions, please see information listed at the bottom of this form.

License Number	3153700294987
License date	May 21, 2013
Licensed content publisher	John Wiley and Sons
Licensed content publication	Magnetic Resonance in Medicine
Licensed content title	R2*-corrected water–fat imaging using compressed sensing and parallel imaging
Licensed copyright line	Copyright © 2013 Wiley Periodicals, Inc.
Licensed content author	Curtis N. Wiens,Colin M. McCurdy,Jacob D. Willig-Onwuachi,Charles A. McKenzie
Licensed content date	Mar 8, 2013
Start page	n/a
End page	n/a
Type of use	Dissertation/Thesis
Requestor type	Author of this Wiley article
Format	Print and electronic
Portion	Full article
Will you be translating?	No
Total	0.00 USD
Terms and Conditions	

TERMS AND CONDITIONS

This copyrighted material is owned by or exclusively licensed to John Wiley & Sons, Inc. or one of its group companies (each a "Wiley Company") or a society for whom a Wiley Company has exclusive publishing rights in relation to a particular journal (collectively "WILEY"). By clicking "accept" in connection with completing this licensing transaction, you agree that the following terms and conditions apply to this transaction (along with the billing and payment terms and conditions established by the Copyright Clearance Center Inc., ("CCC's Billing and Payment terms and conditions"), at the time that you opened your RightsLink account (these are available at any time at http://myaccount.copyright.com).

Terms and Conditions

1. The materials you have requested permission to reproduce (the "Materials") are protected by copyright.

2.You are hereby granted a personal, non-exclusive, non-sublicensable, non-transferable, worldwide, limited license to reproduce the Materials for the purpose specified in the licensing process. This license is for a one-time use only with a maximum distribution equal to the number that you identified in the licensing process. Any form of republication granted by this license must be completed within two years of the date of the grant of this license (although copies prepared before may be distributed thereafter). The Materials shall not be used in any other manner or for any other purpose. Permission is granted subject to an appropriate acknowledgement given to the author, title of the material/book/journal and the publisher. You shall also duplicate the copyright notice that appears in the Wiley publication in your use of the Material. Permission is also granted on the understanding that nowhere in the text is a previously published source acknowledged for all or part of this Material. Any third party material is expressly excluded from this permission.

3. With respect to the Materials, all rights are reserved. Except as expressly granted by the terms of the license, no part of the Materials may be copied, modified, adapted (except for minor reformatting required by the new Publication), translated, reproduced, transferred or distributed, in any form or by any means, and no derivative works may be made based on the Materials without the prior permission of the respective copyright owner. You may not alter, remove or suppress in any manner any copyright, trademark or other notices displayed by the Materials. You may not license, rent, sell, loan, lease, pledge, offer as security, transfer or assign the Materials, or any of the rights granted to you hereunder to any other person.

4. The Materials and all of the intellectual property rights therein shall at all times remain the exclusive property of John Wiley & Sons Inc or one of its related companies (WILEY) or their respective licensors, and your interest therein is only that of having possession of and the right to reproduce the Materials pursuant to Section 2 herein during the continuance of this Agreement. You agree that you own no right, title or interest in or to the Materials or any of the intellectual property rights therein. You shall have no rights hereunder other than the license as provided for above in Section 2. No right, license or interest to any trademark, trade name, service mark or other branding ("Marks") of WILEY or its licensors is granted hereunder, and you agree that you shall not assert any such right, license or interest with respect thereto.

5. NEITHER WILEY NOR ITS LICENSORS MAKES ANY WARRANTY OR REPRESENTATION OF ANY KIND TO YOU OR ANY THIRD PARTY, EXPRESS, IMPLIED OR STATUTORY, WITH RESPECT TO THE MATERIALS OR THE ACCURACY OF ANY INFORMATION CONTAINED IN THE MATERIALS, INCLUDING, WITHOUT LIMITATION, ANY IMPLIED WARRANTY OF MERCHANTABILITY, ACCURACY, SATISFACTORY QUALITY, FITNESS FOR A PARTICULAR PURPOSE, USABILITY, INTEGRATION OR NON-INFRINGEMENT AND ALL SUCH WARRANTIES ARE HEREBY EXCLUDED BY WILEY AND ITS LICENSORS AND WAIVED BY YOU.

6. WILEY shall have the right to terminate this Agreement immediately upon breach of this

Agreement by you.

7. You shall indemnify, defend and hold harmless WILEY, its Licensors and their respective directors, officers, agents and employees, from and against any actual or threatened claims, demands, causes of action or proceedings arising from any breach of this Agreement by you.

8. IN NO EVENT SHALL WILEY OR ITS LICENSORS BE LIABLE TO YOU OR ANY OTHER PARTY OR ANY OTHER PERSON OR ENTITY FOR ANY SPECIAL, CONSEQUENTIAL, INCIDENTAL, INDIRECT, EXEMPLARY OR PUNITIVE DAMAGES, HOWEVER CAUSED, ARISING OUT OF OR IN CONNECTION WITH THE DOWNLOADING, PROVISIONING, VIEWING OR USE OF THE MATERIALS REGARDLESS OF THE FORM OF ACTION, WHETHER FOR BREACH OF CONTRACT, BREACH OF WARRANTY, TORT, NEGLIGENCE, INFRINGEMENT OR OTHERWISE (INCLUDING, WITHOUT LIMITATION, DAMAGES BASED ON LOSS OF PROFITS, DATA, FILES, USE, BUSINESS OPPORTUNITY OR CLAIMS OF THIRD PARTIES), AND WHETHER OR NOT THE PARTY HAS BEEN ADVISED OF THE POSSIBILITY OF SUCH DAMAGES. THIS LIMITATION SHALL APPLY NOTWITHSTANDING ANY FAILURE OF ESSENTIAL PURPOSE OF ANY LIMITED REMEDY PROVIDED HEREIN.

9. Should any provision of this Agreement be held by a court of competent jurisdiction to be illegal, invalid, or unenforceable, that provision shall be deemed amended to achieve as nearly as possible the same economic effect as the original provision, and the legality, validity and enforceability of the remaining provisions of this Agreement shall not be affected or impaired thereby.

10. The failure of either party to enforce any term or condition of this Agreement shall not constitute a waiver of either party's right to enforce each and every term and condition of this Agreement. No breach under this agreement shall be deemed waived or excused by either party unless such waiver or consent is in writing signed by the party granting such waiver or consent. The waiver by or consent of a party to a breach of any provision of this Agreement shall not operate or be construed as a waiver of or consent to any other or subsequent breach by such other party.

11. This Agreement may not be assigned (including by operation of law or otherwise) by you without WILEY's prior written consent.

12. Any fee required for this permission shall be non-refundable after thirty (30) days from receipt

13. These terms and conditions together with CCC's Billing and Payment terms and conditions (which are incorporated herein) form the entire agreement between you and WILEY concerning this licensing transaction and (in the absence of fraud) supersedes all prior agreements and representations of the parties, oral or written. This Agreement may not be amended except in writing signed by both parties. This Agreement shall be binding upon and inure to the benefit of the parties' successors, legal representatives, and authorized assigns.

14. In the event of any conflict between your obligations established by these terms and conditions and those established by CCC's Billing and Payment terms and conditions, these terms and conditions shall prevail.

15. WILEY expressly reserves all rights not specifically granted in the combination of (i) the

license details provided by you and accepted in the course of this licensing transaction, (ii) these terms and conditions and (iii) CCC's Billing and Payment terms and conditions.

16. This Agreement will be void if the Type of Use, Format, Circulation, or Requestor Type was misrepresented during the licensing process.

17. This Agreement shall be governed by and construed in accordance with the laws of the State of New York, USA, without regards to such state's conflict of law rules. Any legal action, suit or proceeding arising out of or relating to these Terms and Conditions or the breach thereof shall be instituted in a court of competent jurisdiction in New York County in the State of New York in the United States of America and each party hereby consents and submits to the personal jurisdiction of such court, waives any objection to venue in such court and consents to service of process by registered or certified mail, return receipt requested, at the last known address of such party.

Wiley Open Access Terms and Conditions

Wiley publishes Open Access articles in both its Wiley Open Access Journals program [http://www.wileyopenaccess.com/view/index.html] and as Online Open articles in its subscription journals. The majority of Wiley Open Access Journals have adopted the Creative Commons Attribution License (CC BY) which permits the unrestricted use, distribution, reproduction, adaptation and commercial exploitation of the article in any medium. No permission is required to use the article in this way provided that the article is properly cited and other license terms are observed. A small number of Wiley Open Access journals have retained the Creative Commons Attribution Non Commercial License (CC BY-NC), which permits use, distribution and reproduction in any medium, provided the original work is properly cited and is not used for commercial purposes.

Online Open articles - Authors selecting Online Open are, unless particular exceptions apply, offered a choice of Creative Commons licenses. They may therefore select from the CC BY, the CC BY-NC and the Attribution-NoDerivatives (CC BY-NC-ND). The CC BY-NC-ND is more restrictive than the CC BY-NC as it does not permit adaptations or modifications without rights holder consent.

Wiley Open Access articles are protected by copyright and are posted to repositories and websites in accordance with the terms of the applicable Creative Commons license referenced on the article. At the time of deposit, Wiley Open Access articles include all changes made during peer review, copyediting, and publishing. Repositories and websites that host the article are responsible for incorporating any publisher-supplied amendments or retractions issued subsequently.
Wiley Open Access articles are also available without charge on Wiley's publishing platform, **Wiley Online Library** or any successor sites.

Conditions applicable to all Wiley Open Access articles:

- The authors' moral rights must not be compromised. These rights include the right of "paternity" (also known as "attribution" - the right for the author to be identified as such) and "integrity" (the right for the author not to have the work altered in such a way that the author's reputation or integrity may be damaged).
- Where content in the article is identified as belonging to a third party, it is the obligation

of the user to ensure that any reuse complies with the copyright policies of the owner of that content.

- If article content is copied, downloaded or otherwise reused for research and other purposes as permitted, a link to the appropriate bibliographic citation (authors, journal, article title, volume, issue, page numbers, DOI and the link to the definitive published version on Wiley Online Library) should be maintained. Copyright notices and disclaimers must not be deleted.
  - Creative Commons licenses are copyright licenses and do not confer any other rights, including but not limited to trademark or patent rights.

- Any translations, for which a prior translation agreement with Wiley has not been agreed, must prominently display the statement: "This is an unofficial translation of an article that appeared in a Wiley publication. The publisher has not endorsed this translation."

Conditions applicable to non-commercial licenses (CC BY-NC and CC BY-NC-ND)

For non-commercial and non-promotional purposes individual non-commercial users may access, download, copy, display and redistribute to colleagues Wiley Open Access articles. In addition, articles adopting the CC BY-NC may be adapted, translated, and text- and data-mined subject to the conditions above.

Use by commercial "for-profit" organizations

Use of non-commercial Wiley Open Access articles for commercial, promotional, or marketing purposes requires further explicit permission from Wiley and will be subject to a fee. Commercial purposes include:

  - Copying or downloading of articles, or linking to such articles for further redistribution, sale or licensing;
  - Copying, downloading or posting by a site or service that incorporates advertising with such content;
  - The inclusion or incorporation of article content in other works or services (other than normal quotations with an appropriate citation) that is then available for sale or licensing, for a fee (for example, a compilation produced for marketing purposes, inclusion in a sales pack)
  - Use of article content (other than normal quotations with appropriate citation) by for-profit organizations for promotional purposes
  - Linking to article content in e-mails redistributed for promotional, marketing or educational purposes;
  - Use for the purposes of monetary reward by means of sale, resale, license, loan, transfer or other form of commercial exploitation such as marketing products

- Print reprints of Wiley Open Access articles can be purchased from: corporatesales@wiley.com

The modification or adaptation for any purpose of an article referencing the CC BY-NC-ND License requires consent which can be requested from RightsLink@wiley.com .

Other Terms and Conditions:

BY CLICKING ON THE "I AGREE..." BOX, YOU ACKNOWLEDGE THAT YOU HAVE READ AND FULLY UNDERSTAND EACH OF THE SECTIONS OF AND PROVISIONS SET FORTH IN THIS AGREEMENT AND THAT YOU ARE IN AGREEMENT WITH AND ARE WILLING TO ACCEPT ALL OF YOUR OBLIGATIONS AS SET FORTH IN THIS AGREEMENT.

v1.8

If you would like to pay for this license now, please remit this license along with your payment made payable to "COPYRIGHT CLEARANCE CENTER" otherwise you will be invoiced within 48 hours of the license date. Payment should be in the form of a check or money order referencing your account number and this invoice number RLNK501025936.
Once you receive your invoice for this order, you may pay your invoice by credit card. Please follow instructions provided at that time.

Make Payment To:
Copyright Clearance Center
Dept 001
P.O. Box 843006
Boston, MA 02284-3006

For suggestions or comments regarding this order, contact RightsLink Customer Support: customercare@copyright.com or +1-877-622-5543 (toll free in the US) or +1-978-646-2777.

Gratis licenses (referencing $0 in the Total field) are free. Please retain this printable license for your reference. No payment is required.

Curriculum Vitae

Name:	Curtis Wiens
Post-secondary Education and Degrees:	The University of Western Ontario London, Ontario, Canada 2008-2013 Ph.D.
	University of Victoria Victoria, British Columbia, Canada 2004-2007 B.Sc.
	College of the Rockies Cranbrook, British Columbia, Canada 2003-2004
Honours and Awards:	Natural Sciences and Engineering Research Council of Canada (NSERC) CGS Doctoral Scholarship 2011-2013
	Western Graduate Research Scholarship (WGRS) Physics and Astronomy, University of Western Ontario 2008-2013
	Ontario Graduate Scholarship 2011 (Declined)
	UVIC Fellowship University of Victoria 2007 (Declined)
Related Work Experience	Teaching Assistant Department of Physics and Astronomy The University of Western Ontario 2008-2013
	Research Assistant Department of Physics and Astronomy University of Victoria 2007

Publications:

Yang IY, Cui Y, **Wiens CN**, Wade TP, Friesen-Waldner LJ, McKenzie CA. Fat Fraction Bias Correction using T1 estimates and Flip Angle Mapping, Journal of Magnetic Resonance Imaging, 2013 (early print).

Wiens CN, McCurdy CM, Willig-Onwuachi JD, McKenzie CA. A combined approach to Compressed Sensing and Parallel Imaging for Fat-Water Separation with R2* estimation, Magnetic Resonance in Medicine, 2013 (early print).

Wiens CN, Kisch SJ, Willig-Onwuachi JD, McKenzie CA. Computationally Rapid Method of Estimating SNR for phased array image reconstructions, Magnetic Resonance in Medicine, 2011:66:1192-1197.

Conference Presentations:

Gibson E, Friesen-Waldner LJ, Hamilton AM, Ribot EJ, Wade TP, **Wiens CN**, Thind K, Harris JK, Borradaile NM, McKenzie CA. Hyperpolarized [1-13C]-Pyruvate Metabolism in Brown Fat, Proceedings of the 21th Annual Meeting of ISMRM. Salt Lake City, USA, 2013.

Wade TP, **Wiens CN**, McKenzie CA. Eddy Current Compensated IDEAL (ECC-IDEAL), Proceedings of the 21th Annual Meeting of ISMRM. Salt Lake City, USA, 2013.

Friesen-Waldner LJ, Wade TP, **Wiens CN**, Thind K, Harris JK, Sinclair KP, Chen AP, Borradaile NM, McKenzie CA. Hyperpolarized [1-13C]-Pyruvate Metabolism in Brown Fat, Proceedings of the 21th Annual Meeting of ISMRM. Salt Lake City, USA, 2013.

Friesen-Waldner LJ, Wade TP, **Wiens CN**, Thind K, Harris JK, Sinclair KP, Chen AP, Borradaile NM, McKenzie CA. Hyperpolarized [1-13C]-Pyruvate Metabolism in Brown Fat, Imaging Network Ontario Symp, 2013.

Wiens CN, Wade TP, Friesen-Waldner LJ, Thind K, Sinclair KP, Chen AP, Borradaile NM, McKenzie CA. In-vivo Characterization of Hepatic Anabolic Metabolism using Hyperpolarized [1-13C] Pyruvate in a Fatty Liver Mouse Model at Clinical Field Strength}, Imaging Network Ontario Symp, 2013.

Thind K, Ouriadov A, Chen AP, Lim H, **Wiens CN**, Martinez P, McKenzie CA, Scholl TJ, Santyr GE. Use of the IDEAL technique with Hyperpolarized 13C-bicarbonate to map pH, Imaging Network Ontario Symp, 2013.

Wiens CN, Friesen-Waldner LJ, Wade TP, Sinclair KP, McKenzie CA. Accelerated 13C Chemical Shift imaging of Hyperpolarized [1-13C] Pyruvate, ISMRM Workshop on Data Sampling and Image Reconstruction, Sedona, USA, 2013.

Wiens CN, McCurdy CM, Willig-Onwuachi JD, McKenzie CA. A combined approach to Compressed Sensing and Parallel Imaging for Fat-Water Separation with R2* estimation, Proceedings of the 20th Annual Meeting of ISMRM, Melbourne, Australia, 2012.

Cui Y, Yang IY, Wade TP, **Wiens CN**, Soliman AS, McKenzie CA. Fast Absolute Quantification of in-vivo Water and Fat Content, Proceedings of the 20th Annual Meeting of ISMRM, Melbourne, Australia, 2012.

Addeman BT, Beaton M, Hegele RA, Soliman AS, **Wiens CN**, McKenzie CA. Validation of Volumetric and Single Slice MRI Adipose analysis using a novel Fully Automated Segmentation method, Proceedings of the 20th Annual Meeting of ISMRM, Melbourne, Australia, 2012.

Yang IY, Cui Y, **Wiens CN**, Wade TP, McKenzie CA. Fat Fraction Bias Correction using T1 estimates and Flip Angle Mapping, Proceedings of the 20th Annual Meeting of ISMRM, Melbourne, Australia, 2012.

Addeman BT, Soliman AS, **Wiens CN**, McKenzie CA. Volumetric Fat Quantification of Intra-Abdominal Adipose Tissue from a Single Breath Hold Acquisition, Proceedings of the 20th Annual Meeting of ISMRM, Melbourne, Australia, 2012.

Yang IY, Cui Y, **Wiens CN**, Wade TP, McKenzie CA. Fat Fraction Bias Correction using T1 estimates and Flip Angle Mapping, ISMRM Workshop on Fat-Water Separation, Longbeach, USA, 2012.

Cui Y, Yang IY, Wade TP, **Wiens CN**, Soliman AS, McKenzie CA. Absolute Quantification of in-vivo Water and Fat Content, ISMRM Workshop on Fat-Water Separation, Longbeach, USA, 2012.

Wiens CN, McCurdy CM, Willig-Onwuachi JD, McKenzie CA. A combined approach to Compressed Sensing and Parallel Imaging for Fat-Water Separation with R2* estimation, ISMRM Workshop on Fat-Water Separation, Longbeach, USA, 2012.

Addeman BT, Soliman AS, **Wiens CN**, McKenzie CA. Volumetric Fat Quantification of Intra-Abdominal Adipose Tissue from a Single Breath Hold Acquisition, ISMRM Workshop on Fat-Water Separation, Longbeach, USA, 2012.

Addeman BT, Beaton M, Hegele RA, Soliman AS, **Wiens CN**, McKenzie CA. Validation of Volumetric and Single Slice MRI Adipose analysis using a novel Fully Automated Segmentation method, ISMRM Workshop on Fat-Water Separation, Longbeach, USA, 2012.

Yang IY, **Wiens CN**, Friesen-Waldner LJ, McKenzie CA. Fat Fraction Bias Correction using T1 estimates and Flip Angle Mapping, ISMRM Workshop on Fat-Water Separation, Longbeach, USA, 2012.

Tanguay J, **Wiens CN**, McKenzie CA, Santyr GE. Accelerated Magnetic Resonance Imaging of the Breast Using Multi-Channel Radiofrequency Coil Arrays at 3 Tesla, Canadian Organization of Medical Physicists, Ottawa, 2010.

Wiens CN, Kisch SJ, Willig-Onwuachi JD, McKenzie CA. Computationally Rapid Method of Estimating SNR for phased array image reconstructions, London Imaging, 2010.

Wiens CN, Kisch SJ, Hines CD, Yu H, Pineda AR, Robson PM, Brittain JH, Reeder SB, McKenzie CA. Noise weighted T2*-IDEAL Reconstruction for non-uniformly undersampled k-space acquisitions, London Imaging, 2010.

Wiens CN, Kisch SJ, Willig-Onwuachi JD, McKenzie CA. Computationally Rapid Method of Estimating SNR for phased array image reconstructions, Proceedings of the 18th Annual Meeting of ISMRM, Stockholm, Sweden, 2010.

Wiens CN, Kisch SJ, Hines CD, Yu H, Pineda AR, Robson PM, Brittain JH, Reeder SB, McKenzie CA. Noise weighted T2*-IDEAL Reconstruction for non-uniformly undersampled k-space acquisitions, Proceedings of the 18th Annual Meeting of ISMRM, Stockholm, Sweden, 2010.

Wiens CN, Addeman BT, Kisch SJ, Hines CD, Yu H, Brittain JH, Reeder SB, McKenzie CA. Quantification of Noise Efficiency with T1 corrected IDEAL Spoiled Gradient Echo Imaging, London Imaging, 2009.

Wiens CN, Addeman BT, Kisch SJ, Hines CD, Yu H, Brittain JH, Reeder SB, McKenzie CA. Quantification of Noise Efficiency with T1 corrected IDEAL Spoiled Gradient Echo Imaging, Proceedings of the 17th Annual Meeting of ISMRM, Honolulu, USA, 2009.

Wiens CN, Kisch SJ, Hines CD, Yu H, Pineda AR, Robson PM, Brittain JH, Reeder SB, McKenzie CA. Noise weighted T2*-IDEAL Reconstruction for non-uniformly undersampled k-space acquisitions, ISMRM Workshop on Parallel Imaging, Santa Cruz, USA, 2009.